Winter 12-15-2015

Identifying the Origin of Galactic Cosmic Rays with the SuperTIGER Instrument

Ryan Patrick Murphy
Washington University in St. Louis

WASHINGTON UNIVERSITY IN ST. LOUIS

Department of Physics

Dissertation Examination Committee:
Martin H. Israel, Chair
W. Robert Binns, Co-Chair
James Buckley
Ramanath Cowsik
Henric Krawczynski
Katharina Lodders

Identifying the Origin of Galactic Cosmic Rays with the SuperTIGER Instrument

by

Ryan Patrick Murphy

A dissertation presented to the
Graduate School of Arts and Sciences
of Washington University in
partial fulfillment of the
requirements for the degree of

Doctor of Philosophy

December 2015
Saint Louis, Missouri

Contents

List of Tables

List of Figures

Acknowledgments

This dissertation would not have been possible without the help and support of a great number of people. I will thank as many as I can here, but I certainly will end up forgetting someone important, for which I apologize.

First, I need to thank Bob and Marty. For the 6 years I worked in our group, I couldn't have asked for more supportive, encouraging, and patient mentors and advisors. Their example has helped me become a better scientist, and I'm thankful for the opportunity to work in our group.

I also want to thank John E. Ward, for his support as a friend and colleague throughout the construction, flight, and data analysis, over 4 years and spanning 5 continents. He managed to put up with me for three months in a small office in Antarctica (and also demanded his own paragraph).

Thank you to Brian Rauch, whose advice and help has been extremely helpful over the past several years, particularly as I worked through the last stages of the data analysis, where his expertise was much appreciated. Thank you to my committee members–Bob, Marty, Jim Buckley, Ram Cowsik, Henric Krawczynski, and Katharina Lodders, for their helpful comments in preparing this final draft of the thesis.

Thank you to the entire Wash U SuperTIGER team–Dana "God of Thunder" Braun, Paul Dowkontt, Richard Bose, Marty Olevitch, Garry Simburger, and Phil Moore. This thesis would not have been possible without their hard work, and the help that they gave me throughout the past 6 years has taught me a great deal. Thank you to the Physics Department Shop–Todd Hardt, Tony Biondo, and Denny Huelsman–for their hard work machining most of the SuperTIGER experiment. I also want to thank the other graduate students who I overlapped with in our group, Kelly Lave, Dan Flanagan and Nathan Walsh, for their help throughout the years. I especially need to thank Dan for setting up everything for my first summer of lab work. Thank you as well to our talented undergraduate students who I had the pleasure to work with, Katie Thomas, Ashley Williams, and Ari Eisenstadt.

A big thank you to the entire SuperTIGER collaboration. I want to thank my NASA Goddard Space Flight Center colleagues–John Mitchell, Thomas Hams, Makoto Sasaki, Terri Brandt, Jason Link, Kenichi Sakai, Sean Fitzsimmons, Frank San Sebastian, Devin Hahne–as well as the many other people who helped out at Goddard, including Bill Daniels, Don, Mel, Becky, and others that I'm sure I'm forgetting, for making me feel welcome and their help during the time I spent working there. I also need to thank Makoto for all of his help in the data analysis, including making the DST files and providing the stlib code library. I want to single out Thomas for his impressive work on the SuperTIGER recovery, and for working with me throughout my involvement in that endeavor. I also want to thank Kenichi for putting up with me as a roommate during our time in Antarctica. Thank you to our collaborators at Caltech–Mark Wiedenbeck, Allan Labrador, Dick Mewaldt, John Klemic, and Ed Stone–for their help throughout the past several years. I especially want to thank

Mark for his work with the galactic propagations I use in this thesis. Thank you to Jake Waddington of the University of Minnesota for his helpful suggestions and comments.

I want to thank Vernon Jones, Debbie Fairbrother, the NASA Balloon Program Office and the everyone at the Columbia Scientific Balloon Facility for the excellent and highly professional efforts that resulted in the record long-duration balloon flight of SuperTIGER. In particular, I want to thank Drew Denney, our payload engineer, for working with us to get everything ready to fly as soon as possible. I also want to thank Fred Perrin and Joseph Jones for their help while I was testing our HV boards at CSBF. Thank you to Dave Sullivan and Dwayne Orr for overseeing the balloon campaign in McMurdo. Thank you to everyone else from CSBF for helping SuperTIGER throughout our preparations, flight, and recovery. I also want to thank Rachel Maynard and everyone at NASA Plum Brook Station for their help during our thermal vacuum test.

Thank you to the National Science Foundation and the United States Antarctic Program for providing the opportunity for the SuperTIGER flight and their support during the flight and recovery. I also want to thank the Antarctica Support Contract (ASC) and everyone at McMurdo station and the South Pole for their help and support. Thank you to Scott Battaion and Anne Dal Vera for all of their help at the LDB site (and in Scott's case, on the 2014 recovery attempt). Thank you to Lisa Rugar, Annie, and everyone else that helped in the galley at the LDB site for the best lunches on the continent. A big thank you to the groom team–James King, Lyra Pierotti, and Dave White–as well as Ryan Wallace, our science implementer, for their hard work on the SuperTIGER recovery effort (and for putting

up with us as we tried to get ourselves out into the field). Thank you to Kenn Borek Air and the pilots that helped us with the SuperTIGER recovery. First, thank you to the Twin Otter pilots–Rodney Fishbrook, who flew the 2014 recovery team for their over flight, Steve Kaizer, who flew the SuperGroom Team in to the SuperTIGER site, and Henry Perk, who brought out a new snowmobile and returned the first load of recovered parts. I also want to thank the crew of the Basler that took Sean and I out to the recovery site–Dereck Peterson, John Gilmour, Lucius Cirwell, and Tyson "Tyrone" Taylor–for helping us with the recovery and hanging out with us at the Pole while we waited for the weather to be right.

Thank you to Peggy Fossett and the Peggy and Steve Fossett Foundation, whose generous donation established the Peggy and Steve Fossett Antarctic Astrophysics Fellowship, which supported me for two years of my thesis research. I also want to thank NASA, which supported SuperTIGER through grants NNX09AC17G and NNX14AB25G, and the McDonnell Center for the Space Sciences, which supported SuperTIGER and gave me the funding to travel abroad to present my work in 2013 and 2014.

I want to thank the people I've had the privilege of sharing an office with over the past several years–Jerrad Martin, Ryan Dickherber, Trey Garson, Avery Archer, Nathan Todd, and Wenlei Chen–for supporting me and putting up with me when I distracted them from their work. I also want to thank everyone else on our astrophysics floor for everything over the years: Brett, Sarah, Vicky, Qingzhen, Fabian, Anna, Janie, Banafsheh, and Matthias.

Over my years in graduate school, I've made a lot of amazing friends, but I would like to thank them all here real quick (and again, sorry if I forgot anyone). Thank you to my first group of

friends, that made me feel welcome here in the department: Patrick Johnson (who owes me $1 for defending this thesis before becoming a knight), Brett McArthur, Sara Thibadeau, Jerrad Martin, John Flavin, Jeff Pobst, Evan Groopman, Amber Groopman, Michael "Brandeis" DeSantis, Lauren Tran, Dan Hunter, Tim Mitchell, Kasey Wagoner, Ben Burch, Dimitris Manolidis, Adam Vogt, Matt Blodgett, Saeed Mirshekari, Hossein Mahzoon, and Fletcher Werner. Thank you to all the friends that I met as they arrived here in grad school and who I had the opportunity to be teammates with on sports teams throughout the years: Tom Crockett, Anthony and Lorin Kovacs, Joben Lewis, Avery Archer, Christine Archer, Gabrielle Coutrout (Le Booooo), Matt Reisman, Rachel Crouch, Nick Weingartner, Kelsey Meinerz, Min Shinn, Nara Higano, Brendan Haas, Kim Sukhum, Xinxin Wang, Jon Kessler, Sam Emery, Chris Pueblo, Jason Schaffer, Vy Tran, Ivy Love, Nick Aguelakakis, Mark Johnson, Mack Atkinson, Robert Ashcraft, Augusto Medeiros, Anna Zaczyk, Cole Pruitt, Mike and Lacey Abercrombie, Adam Archibald, Kumar Mallavarapu, Amila Weerasighe, Vikas Soni, and Nero Zhou. Thank you to my group of friends from outside the Physics Department, most of whom I guess I met playing trivia: Tim Mitchell, Joey Ackerman, Drew Yaeger, Richard Bose, Diego Morales, Vic Wessels, Mena Morales, Elizabeth Danka, Matt Strulson, Matt Hynes, Erin Reinl, Megan Erhart, and Anna Boudoures, among many others. Thank you to everyone else that has helped me along the way, and everyone I left out (without meaning to!).

Last and certainly not least, I need to thank my family for all of the support they've given me over the years. I don't really have the words to express everything that I want to say, but thank you for everything.

Ryan Patrick Murphy

Washington University in Saint Louis

December 2015

ABSTRACT OF THE DISSERTATION

Identifying the Origin of Galactic Cosmic Rays with the SuperTIGER Instrument

by

Ryan Patrick Murphy

Doctor of Philosophy in Physics

Washington University in St. Louis

Professor Martin H. Israel, Chair

The SuperTIGER (Trans-Iron Galactic Element Recorder) experiment was launched on a long-duration balloon flight from Williams Field, Antarctica, on December 8, 2012. The instrument measured the relative elemental abundances of galactic cosmic rays (GCR) in the charge (Z) range Z >10 with excellent charge resolution, displaying well resolved individual element peaks for $10 \leq Z \leq 40$. During its record-breaking 55-day flight, SuperTIGER collected ∼4.15 $\times 10^6$ Iron nuclei, ∼7.5 times as many as detected by its predecessor, TIGER, with charge resolution at iron of < 0.18 cu. SuperTIGER measures charge (Z) and energy (E) using a combination of three scintillator and two Cherenkov detectors, and employs a scintillating fiber hodoscope for event trajectory determination. The SuperTIGER data have been analyzed to correct for instrument effects and remove events that underwent nuclear interactions within the instrument. The data include more than 600 events in the charge range $30 < Z \leq 40$. SuperTIGER is the first experiment to resolve elemental abundances in this charge range with single-element resolution and high statistics. The relative abundances of the galactic cosmic ray source have been derived using atmospheric and interstellar propagations of the measured relative elemental abundances. The SuperTIGER measured abundances are generally consistent with previous experimental

results from TIGER and ACE-CRIS, with improved statistical precision. The SuperTIGER results confirm the earlier results from TIGER, supporting a model of cosmic-ray origin in OB associations, with preferential acceleration of refractory elements over volatile elements ordered by atomic mass (A).

Chapter 1

Introduction

Cosmic Rays are charged particles of extraterrestrial origin that are observed to be isotropically incident on the Earth's atmosphere. Cosmic rays have been observed over a wide range of energies. The lowest energy Cosmic Rays, Solar Energetic Particles (generally $E <\sim 10^7$eV/nucleon), originate in the heliosphere. At somewhat higher energies, Galactic Cosmic Rays (GCR) originate and are accelerated elsewhere in the Milky Way. Extragalactic Cosmic Rays at extremely high energies (over 10^{18}-10^{19} GeV) have also been observed and are thought to originate in extragalactic sources like Active Galactic Nuclei (AGN) or gamma-ray bursters. Galactic cosmic rays are composed of ∼98% atomic nuclei and about ∼2% electrons, positrons, and anti-protons. Of the GCR nuclei, ∼89% are hydrogen (protons), while ∼10% are helium and ∼1% are heavier elements. This dissertation focuses on the SuperTIGER experiment, which is designed to measure the abundances of elements with atomic number Z in the range of $30 \leq Z \leq 40$. These ultra-heavy GCR are only a very small fraction of the GCR heavier than helium.

Cosmic Rays were first identified as being of extraterrestrial origin by Victor Hess (1912), who observed that the background radiation detected in his electroscope increased with increased altitude over a series of ballon flights from Austria in 1911 and 1912. In the century that has followed, balloon-based observations of Cosmic Rays have continued to play

a significant role in increasing our understanding of the universe. Scientific ballooning offers a platform above ∼99.5% of the Earth's atmosphere, which allows for direct measurements of GCR with a limited atmospheric overburden. For direct measurements of GCR in the ultra-heavy range, the ideal measurement location is in space beyond the Earth's magnetosphere, but long-duration balloon flights provide a viable low-cost alternative. These flights allow for a long exposure time—up to ∼55 days with conventional long-duration balloon technology, but with ultra-long-duration balloons offering 100+ day flights in the near future—for heavy instruments (up to ∼2000 kg) at a fraction of the cost of a space-based detector. Balloon payloads can also be refurbished and re-used on multiple flights, allowing for an even longer combined exposure time.

1.1 Galactic Cosmic Rays

Supernovae are thought to be the cause of GCR acceleration. To maintain the constant flux of GCR, 10^{41} erg/second of power is required, if one assumes a simple leaky box model of galactic propagation (Lingenfelter, 1992). Supernovae are one class of sources that have enough energy to maintain this power. The rate of supernovae within the galaxy is ∼3 per century (van den Bergh and Mclure, 1994), so the average amount of energy from each supernova required by the GCR is $\sim 10^{50}$ ergs. Since the average ejecta kinetic energy of a supernova is $\sim 10^{51}$ ergs, this means that the energy required to maintain the GCR is about 10% of the shock wave energy of supernovae within the galaxy (although different galactic propagation models, such as the nested leaky box model, may require a lower fraction of SN energy). The GCR are thought to reach their high energies (up to the knee of the all particle spectrum, $\sim 10^{15}$eV/nucleon) due to diffusive shock acceleration within the supernova shock waves.

The Galactic cosmic rays observed at Earth can be classified into two categories: primary cosmic rays and secondary cosmic rays. Primary cosmic rays were created at the GCR source and accelerated to high energies before traveling through the galaxy to Earth. Secondary cosmic rays are nuclei created as the result of nuclear interactions of cosmic ray nuclei with the interstellar medium. These nuclear interactions can result in the fragmentation (or spallation) of heavier GCR nuclei into lighter nuclei that are then observed as secondaries at Earth. For most elements, the GCR flux observed at Earth is a mixture of primary and secondary nuclei.

1.1.1 Ultra-Heavy GCR and TIGER

UH GCR have been observed by numerous previous experiments. Early observations were carried out by two instruments aboard the HEAO 3 spacecraft, HEAO-3-C2 (Byrnak et al., 1983) and HEAO-3-C3 (Binns et al., 1987). These experiments made exploratory measurements on the abundances of UH GCR. HEAO-3-C2 made measurements with single-element resolution up to $_{32}$Ge. HEAO-3-C3 made exploratory measurements at higher Z but lacked the single-element resolution found on later experiments. The Ariel 6 experiment (Fowler et al., 1986) made observations in the UH range at the same time as HEAO but also lacked single-element resolution. The Trek instrument aboard the *Mir* space station also made exploratory measurements in the charge range $72 \leq Z \leq 82$ using passive track detectors (Weaver and Westphal, 2005). Trek also detected 6 actinides ($89 \leq Z \leq 103$).

The Trans-Iron Galactic Element Recorder (TIGER) experiment was a balloon-borne cosmic ray detector that had three balloon campaigns in North America (a short flight due to balloon failure in 1995 and a failed launch in 1996 from Lynn Lake, MB, Canada, and a successful 22-hour flight in 1997 from Ft. Sumner, NM) and two successful long-duration balloon flights in Antarctica in 2001-2002 and 2003-2004. TIGER used scintillator detectors,

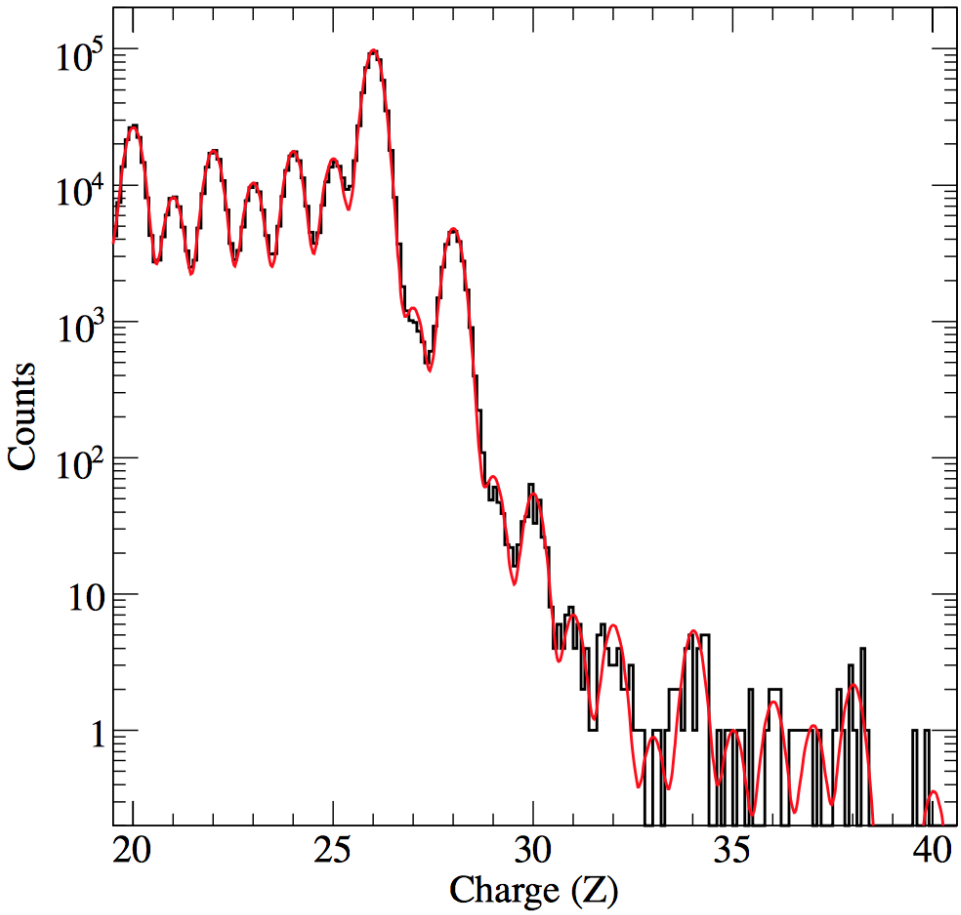

Figure 1.1: TIGER Charge Histogram from Rauch et al. (2009). ©AAS, reproduced with permission.

Cherenkov detectors, and a scintillating fiber hodoscope similar to the SuperTIGER detectors described in Chapter 2 to measure the charge Z and energy of Galactic Cosmic Ray nuclei. TIGER had individual-element resolution over the $30 \leq Z \leq 40$ charge range, but had extremely limited statistics at higher Z (for example, only 10 $_{38}$Sr were detected). Unfortunately, after the 2003 TIGER flight the instrument landed in a remote location in Antarctica and only a few components of the experiment were recovered. The bulk of the TIGER instrument was abandoned and slowly buried by the drifting snows of east Antarctica. Figure 1.1 shows the elemental abundances measured by TIGER from Rauch et al. (2009). The TIGER instrument and data analysis methods are the direct forerunners of the SuperTIGER

experiment and data analysis techniques described later in this dissertation. A more detailed description of the TIGER results and conclusions can be found elsewhere in this chapter.

1.1.2 Derivation of Galactic Cosmic Ray Source Abundances from Observed Abundances

Experiments like TIGER and SuperTIGER observe the Galactic Cosmic Ray (GCR) flux incident at balloon float altitude (∼38 km on average for SuperTIGER). This flux is a mixture of primary CR and secondary particles created en route from the GCR source to the detector. To derive GCR source abundances, we need to calculate the secondary contributions to the observed abundances. The first step is to calculate what abundances at the top of the instrument are required to give the observed abundances. This is a straightforward calculation using the total charge-changing cross sections for each Z, assuming that those nuclei that interacted within the instrument are eliminated. These top of instrument abundances are then used to calculate the abundances at the top of the atmosphere, which is a more complicated calculation described in Chapter 5. A separate calculation of the interactions of GCR nuclei with the interstellar medium along their journey to earth is then applied, which yields the calculated GCR source abundances. More details of the process used for SuperTIGER can be found in Chapter 5.

1.2 Acceleration Models of Galactic Cosmic Rays

The origin of Galactic Cosmic Ray nuclei has been an ongoing subject of study for decades, and is one of the enduring mysteries of astrophysics. Measurements of GCR composition, consisting of elemental and isotopic abundances, have been made in an attempt

to constrain and test theories of GCR origin. Initial results seemed to favor a model for acceleration where elements with low First Ionization Potentials (FIP) would be preferentially accelerated, but this model gradually fell out of favor when a model based on the volatility of each element was proposed. More recently, the emerging consensus has identified superbubbles, which are blown out by the stellar winds and supernova shocks of OB associations, as the most likely site of the origin and acceleration of GCR. The FIP, Volatility, and OB Association models will all be described briefly.

1.2.1 First Ionization Potential Model

Early theories of the GCR source, including those of Cassé and Goret (1978) and Meyer (1985), suggested that the GCR source was the coronae of stars. This coronal material would then be injected into the space around the star by stellar winds and flare events before being accelerated by a nearby supernova explosion. Both Cassé and Goret (1978) and Meyer (1985) point to the overabundance (relative to Solar System abundances) of elements with lower First Ionization Potential (FIP) in the GCR, similar to that seen in particles from the Sun, as evidence that the GCR source is a hot, gaseous environment such as a stellar atmosphere or wind. Early measurements from the HEAO-3-C3 experiment were consistent with a GCR source with similar elemental abundances to the solar system, with lower-FIP elements preferentially accelerated (Binns et al., 1987). However, these FIP models could not explain the relatively large spread in enhancement for high-FIP elements, including the relatively low abundances of N, Zn, and Ge (Meyer, Drury, and Ellison, 1997). Figure 1.2 shows the ratio of the GCR source derived from TIGER observations (using a process similar to that described in Section 1.1.2) to the Solar System abundances as a function of FIP (figure from Rauch et al. (2009), ©AAS, reproduced with permission). While a general trend is

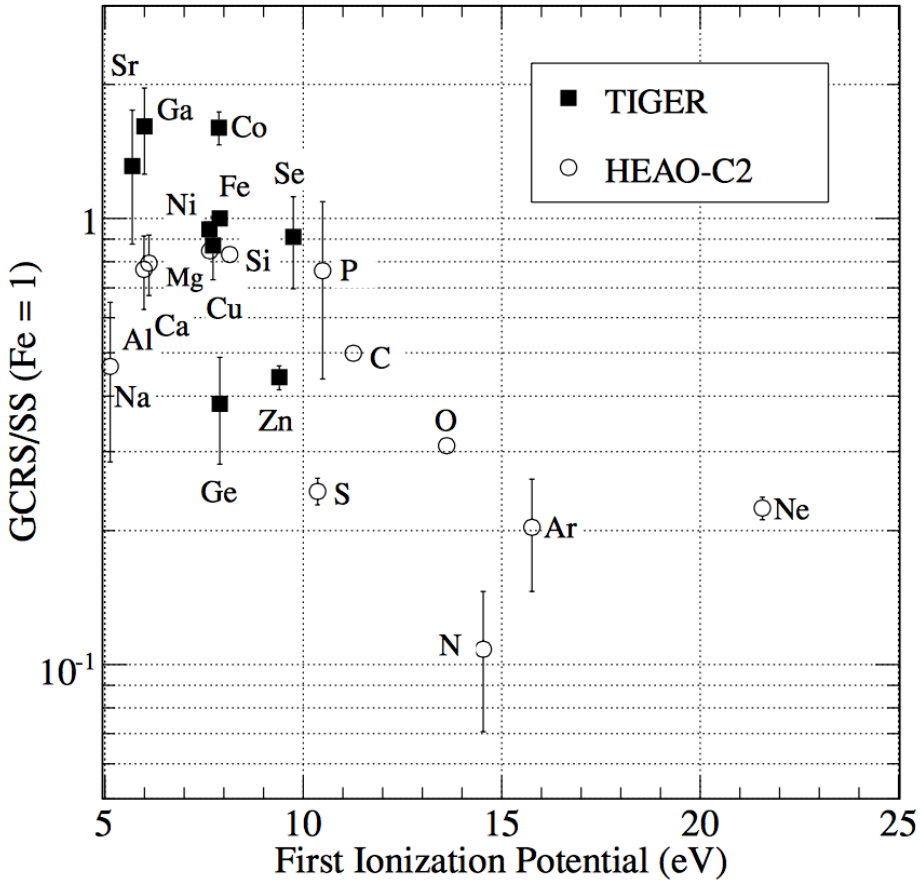

Figure 1.2: Ratio of GCR source abundances to Solar System (SS) abudnances vs First Ionization Potential. Figure re-printed from Rauch et al. (2009). ©AAS, reproduced with permission.

apparent, elements such as $_{32}$Ge and $_{30}$Zn are outliers, showing that the FIP model does not adequately explain discrepancies between the GCR source and Solar System abundances.

1.2.2 Volatility Model

Another model of GCR acceleration seeks to explain the enhancement of primary GCR nuclei in terms of their chemical volatility. Epstein (1980) showed that elements that are found in interstellar dust grains should be preferentially accelerated compared to those that exist primarily as interstellar gasses, due to the higher mass-to-charge ratio of dust grains.

These dust grains are charged by UV ionization. This model predicts similar enhancements to the FIP model, since many low-FIP elements are found in dust grains while most high-FIP elements are primarily found in a gaseous state. Meyer, Drury, and Ellison (1997) and Ellison, Drury, and Meyer (1997) developed this model further, positing that refractory elements (elements with high condensation temperatures $T_c > 1250$ K) found in interstellar dust grains are preferentially accelerated compared to those volatile elements with lower condensation temperatures T_c. Due to photo ionization by UV photons, these dust grains accumulate a small surface electrical charge, which gives them a very high rigidity, and allows for their efficient acceleration by supernova shocks. After collisions with atoms in the local interstellar medium, some atoms are sputtered off the grain and injected into the CR accelerator suprathermally. Volatile elements, found in interstellar gasses, do not have the benefit of this suprathermal injection. For these volatile atoms, Ellison, Drury, and Meyer (1997) suggest a rigidity-based acceleration model that is related to the element's mass (A) to ionized charge (Q) ratio, of the form ($(A/Q)^{\alpha}$). No such mass-dependent trend was predicted for the refractory elements.

Since both the FIP and Volatility models predict similar enhancements in the GCRS/SS ratio, it is difficult to test the differences between the two models. These two atomic properties are often correlated, with most volatile elements having high FIPs and most refractory elements having low FIPs (condensation temperatures can be found in Lodders (2003)). To discriminate between the two theories, accurate measurements of elements where this association is broken are necessary. Among the elements where this association is broken are $_{11}$Na, $_{15}$P, $_{16}$S, $_{29}$Cu, $_{30}$Zn, $_{31}$Ga, $_{32}$Ge, and $_{34}$Se. With the exception of $_{16}$S, the elements in this list with $Z < 26$ have significant secondary contributions to their abundances in the observed GCR flux, making the derivation of GCR source abundances difficult. Most elements with $Z > 26$ will not have a substantial secondary contribution, but single-element resolution and significant statistics are required to draw meaningful conclusions.

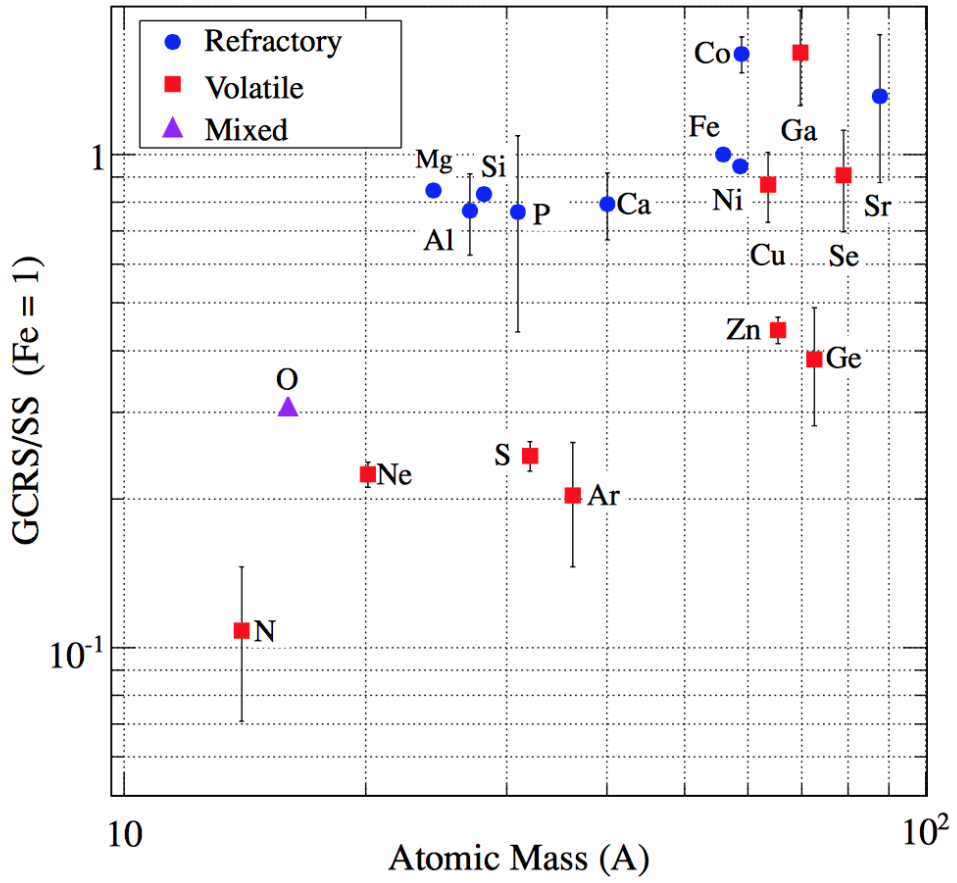

Figure 1.3: Figure from Rauch et al. (2009) showing the ratio of GCR source abundances to Solar System abundances vs atomic mass A. ©AAS, reproduced with permission.

TIGER results from Rauch, in his Ph.D. thesis (2008), suggest that the FIP model "does not explain the GCRS". The Volatility model, however, seems to work well for those elements with $Z < 26$, showing a clear separation between the refractory and volatile elements in the ratio of the GCRS and SS abundances. However, at higher Z, there is less separation, particularly at $_{29}$Cu, $_{31}$Ga, and $_{34}$Se (see Figure1.3). Rauch et al. (2009) explain this by using a further variation of the model for separation between the volatile and refractory elements, discussed in Section 1.3. The expanded statistics from the SuperTIGER experiment that will be presented in this thesis will provide a better test to the FIP and Volatility models.

1.3 OB Association Model of GCR Origins

The current widely accepted explanation of GCR origins is that a large fraction of GCR originate in OB associations. OB associations are loosely organized groups of young, massive, short-lived O and B type stars. Through a combination of supernova shocks and stellar winds, OB associations form large rarified gas cavities known as superbubbles. The potential OB association origins of GCR were first discussed by Montmerle (1979) and Cesarsky and Montmerle (1979). Higdon, Lingenfelter, and Ramaty (1998) suggested superbubbles as a GCR source with constant metallicity, which would match observations of GCR abundances (Higdon et al., 1998), as the composition of the material in and around the cores of superbubbles contains most of the metal-rich grain and gas ejecta from previous supernovae.

1.3.1 Cosmic Ray Evidence for OB Association Model

Results from the ACE/CRIS experiment (Binns et al., 2005) found an enhanced $^{22}Ne/^{20}Ne$ ratio in the GCR compared to the ratio in the solar wind, at 5.0 $\pm$0.2 times that of the solar system, which has been taken as further evidence of the OB association of GCR. Higdon and Lingenfelter (2003) calculated the predicted ^{22}Ne and ^{20}Ne yields in the stellar winds of Wolf-Rayet stars and in supernova ejecta. The most massive, short-lived stars evolve into Wolf-Rayet (WR) stars, which are post-main-sequence stars that have lost their hydrogen-rich stellar envelope, characterized by their high surface temperatures as well as the enhancement of heavy elements at their surfaces and their strong stellar winds. WR stars are commonly found within OB associations, where their strong stellar winds contribute significantly to the formation of superbubbles. Higdon and Lingenfelter (2003) used models of the WR stellar winds (which are the source of the ^{22}Ne) and the ejecta of core-collapse

supernovae (the source of ^{20}Ne) to find neon yields, and combined those yields to estimate the ^{22}Ne/^{20}Ne ratio within superbubbles. This model resulted in their conclusion that the ^{22}Ne/^{20}Ne ratio observed by Binns et al. (2000) could be understood as the result of cosmic rays accelerated out of superbubbles, with a source material that was a mixture of normal interstellar medium enriched with $\sim 18 \pm 5\%$ (by mass fraction) outflow from massive stars and supernova ejecta. Other observations from ACE/CRIS of the ^{12}C/^{16}O and ^{58}Fe/^{56}Fe ratios show smaller deviations from solar system ratios that can also be explained by a GCR source with $\sim$20% massive star outflow and supernova ejecta enrichment (Binns et al., 2005).

Higdon and Lingenfelter (2005) studied the fraction of core-collapse supernovae that occur within superbubbles. By considering the temporal and spatial clustering of OB stars within superbubbles, they came to the conclusion that $\sim 85\%$ of core-collapse (Types II and Ib/c) supernovae occur within superbubbles. Since these core-collapse supernovae account for 85% of galactic supernovae, $\sim$75% of all Galactic supernovae are expected to occur within superbubbles (they also found that only a small fraction ($\sim$10%) of Type Ia supernovae are expected to occur in superbubbles). The mean time between supernovae in OB associations is $\sim 3 \times 10^5$ years, depending on the number of massive stars in the association. Measurements of the abundance of ^{59}Ni, a radioactive isotope that is produced abundantly in the fast r-process nucleosynthesis of a core-collapse SN, have been used to put a lower limit on the amount of time GCR source material exists within OB associations before acceleration. Since ^{59}Ni decays to ^{59}Co only by electron capture with a 7.6×10^4 year half-life in the laboratory, ^{59}Ni GCR nuclei will not decay after acceleration, as the orbital electrons will be removed by peripheral coulombic interactions with the ISM. Observations by Wiedenbeck et al. (1999) using the ACE/CRIS experiment have found that the ^{59}Ni had entirely decayed into ^{59}Co before acceleration, meaning that material formed in a SN is not accelerated by that SN's shock waves, but by another many years later. Wiedenbeck et al. (1999) put a lower limit of $\sim 10^5$ years between synthesis and acceleration of the massive star component

of the GCR source. More recent observations by ACE found the presence of ∼15 ^{60}Fe nuclei (Israel et al., 2015). ^{60}Fe decays via β^- decay into ^{60}Co with a 2.6 × 10^6 year half-life. After propagating the measured abundance at the ACE/CRIS instrument back to the GCR source and comparing with models of ^{60}Fe production in massive stars, this gives an upper limit on the residence time after nucleosynthesis before acceleration of ∼ 2.5 × 10^6 years. OB associations therefore have SN at an appropriate rate given the constraints of the ACE/CRIS measurements, and appear to be the natural astrophysical setting for the acceleration of GCR.

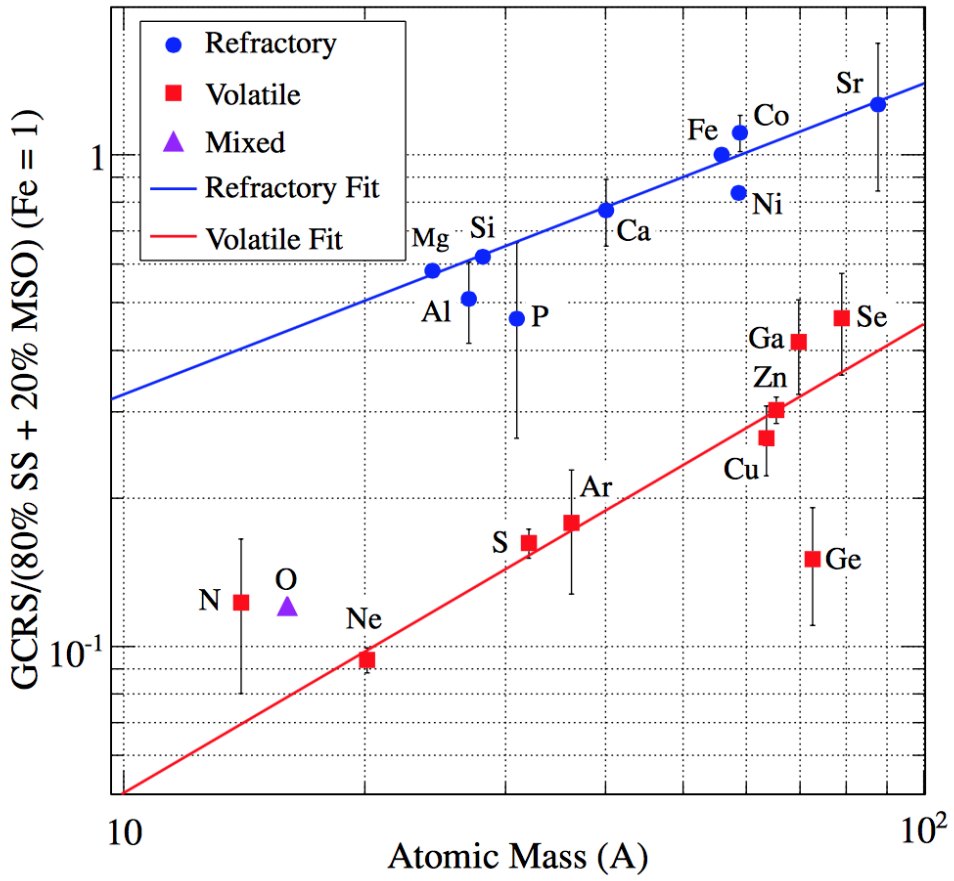

Figure 1.4: Figure from Rauch et al. (2009) showing the ratio of GCR source abundances to material with 80% Solar System abundances and 20% Massive Star Outflow abundances vs atomic mass A. Used with permission.

While Figure 1.3 shows the TIGER measured GCR source compared to the normal ISM/Solar System abundances, Figure 1.4 compares the same GCR source to an OB association-like source, with 80% of the source material with SS abundances from Lodders (2003) and 20% material that is a mixture of massive star outflow from WR stars and ejecta from previous SN (WR stars are also SN precursors). The massive star outflow and ejecta abundances are based on the work of Woosley and Heger (2007), who found elemental yields integrated over a Salpeter initial mass function for solar metallicity stars with initial mass 12 to 120 $M_{\odot}$. More detail on the mixing can be found in Rauch (2008).

The clear enhancement of the refractory elements continues here to a much higher A than in Figure 1.3. This 20% massive star component is similar to the $\sim 18\% \pm 5\%$ calculated by Higdon and Lingenfelter (2003), and the calculations done by Rauch (2008) show a similar separation for models with massive star components ranging from 15% to 25%. Again, the mass-dependent trend for the refractory elements apparent in Figure1.4 is not predicted by the theoretical models of Ellison et al. (1997). The large uncertainty in the $_{38}$Sr abundance is largely statistical, as only 10 $_{38}$Sr were observed in the TIGER data. To ascertain whether this mass-dependent trend is significant, substantially more data are required. The SuperTIGER data to be presented in this thesis contains a significant increase in statistics that will dramatically shrink the UH error bars, particularly of the $_{38}$Sr point, and add new points (for example, $_{40}$Zr) to the graph in Figure 1.4.

1.3.2 Gamma Ray Observations

γ ray observations using the Fermi Large Area Telescope (LAT) (Ackermann et al., 2013) and ground-based arrays (Humensky and the VERITAS Collaboration, 2015) of γ-rays from SN explosions have provide direct evidence that SN remnants accelerate hadrons to high energies. Other γ-ray observations of OB associations have also seen distributed

γ-ray emission from a "cocoon" with morphology coinciding with the Cygnus superbubble (Ackermann et al., 2011), extending $\sim$50 parsecs from the Cygnus OB2 association. Ground-based gamma ray observations by VERITAS (Aliu et al., 2013) have also identified distributed γ ray emission near a supernova remnant. In 2015, the H.E.S.S. (High Energy Stereoscopic System) collaboration detected unambiguous γ ray emission from the 30 Dor C superbubble in the Large Magellanic Cloud (Abramowski et al., 2015). These γ-ray observations of particle acceleration within OB associations lend further support to the measurements of isotopic and elemental abundances that suggest an OB association origin for GCR.

1.4 The SuperTIGER Experiment

The SuperTIGER instrument is designed to measure relative abundances of Galactic Cosmic-Ray (GCR) nuclei from Neon ($Z = 10$) to Zirconium ($Z = 40$) with individual-element charge resolution and high statistical precision. These measurements will provide another test of the OB Association Model of GCR origins. The increased statistics SuperTIGER presented in this thesis will dramatically shrink the error bars on Figure 1.4, particularly of $_{38}$Sr point, and add further points, such $_{40}$Zr, another ultra-heavy, refractory element. This will serve to constrain the mass dependence of the acceleration of Refractory elements. Further Volatile points will also be added, constraining the best-fit GCR source mixture. The GCR source abundances derived from SuperTIGER data will also provide another measurement of the proportions of material with Solar System abundances and Massive Star Outflow and Ejecta in the GCR source.

Chapter 2

The SuperTIGER Instrument

The SuperTIGER instrument is designed to measure relative abundances of Galactic cosmic-ray nuclei from Neon ($Z = 10$) to Zirconium ($Z = 40$) with individual-element charge resolution and high statistical precision, while also making exploratory measurements of elements up to Neodymium ($Z = 60$). SuperTIGER is a balloon-borne instrument that successfully flew for 55 days flight from Williams Field, Antarctica, in 2012-2013. SuperTIGER builds on the heritage of the TIGER instrument, which flew two successful Antarctic long-duration balloon missions in 2001 and 2003.

The SuperTIGER instrument consists of two nearly-identical modules, each consisting of a suite of seven detectors. Three scintillation counters measure the differential energy loss, $\frac{dE}{dX}$ within the instrument, which is a function of a particle's charge Z and relativistic velocity β; two scintillating fiber hodoscopes measure particle trajectory; and two Cherenkov detectors, which give signals proportional to Z and β for particles above the Cherenkov threshold. Cosmic-ray particles traverse the instrument from top to bottom. The top detector is a scintillator detector (S1) that is used in the primary charge determination and to trigger coincidence. The top hodoscope layer (H1 or HT) records the particle (x, y) location at the top of the instrument. Below that, the Aerogel Cherenkov (C0) detector and Acrylic Cherenkov (C1) detectors measure the charge and energy of incident particles.

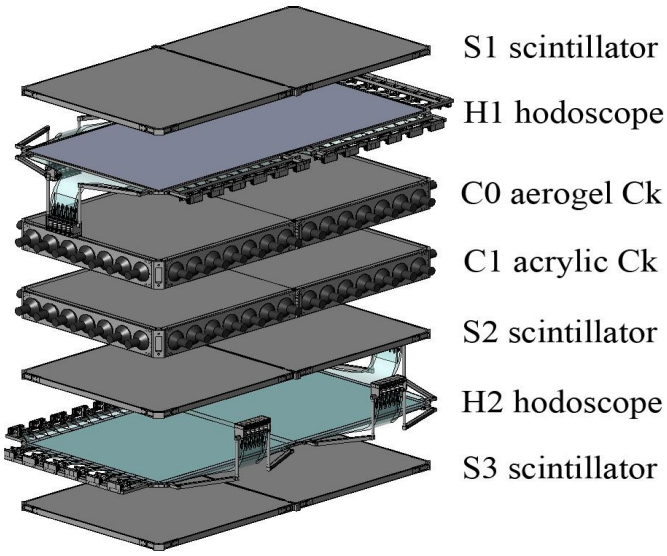

Figure 2.1: Diagram showing the components of one SuperTIGER Module (vertically expanded so each component can be clearly seen).

The S2 scintillator detector is also used for charge assignment and coincidence. The bottom (H2 or HB) hodoscope records the (x, y) location at the bottom of the instrument. The bottom (S3) scintillator detector is used for coincidence, as a backup to S2, and primarily to identify those particles that interacted with the instrument during flight. The instrument was designed to maximize geometric acceptance while still being lightweight enough to fly on a standard 1.11 million m^3 balloon. The active area of each module measures approximately 1.16m×2.4m, and the full geometry factor of both modules is $\sim$8.3m^2sr for particles whose trajectory zenith angle is less than 70 degrees. After accounting for interactions within the instrument, the "effective" geometry factor is $\sim$2.9 m^2sr, which is 7.2 times larger than the previous TIGER instrument. SuperTIGER uses custom front-end electronics (FEE) boards to read out the signals from individual photomultiplier tubes (PMTs) within each detector. Fast-shaping amplifiers on the scintillator FEE boards allow for triggering on particles with $Z \geq 10$. Events above the threshold were recorded in full on SSD drives on both modules

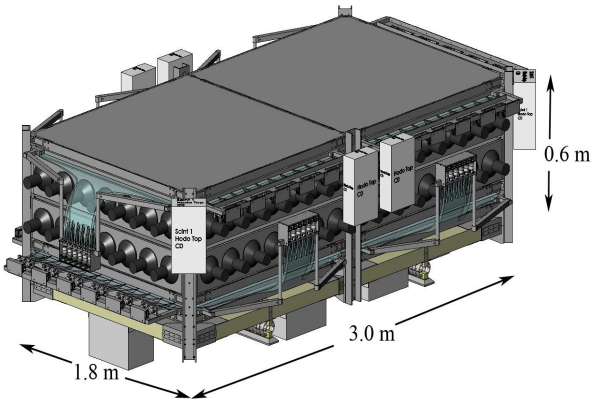

Figure 2.2: Dimensions of each SuperTIGER Module.

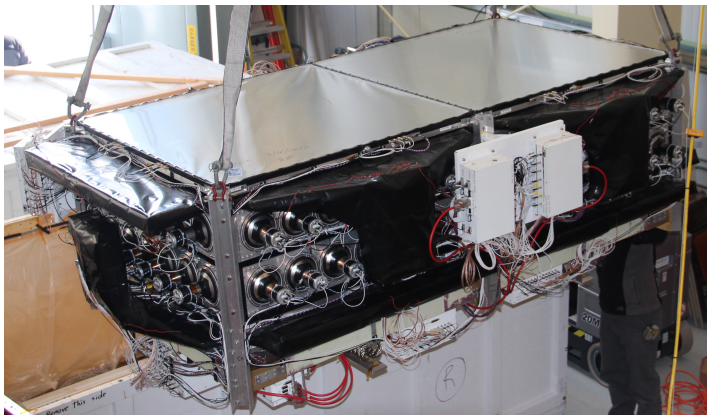

Figure 2.3: A SuperTIGER Module before installation on the Gondola.

(until those drives failed), and telemetered in a compressed format via TDRSS satellites when possible. A priority system assigned high priority to events with $Z \geq 22$. These high-priority events were telemetered before other data events when TDRSS bandwidth was limited. Averaged over the entire flight, TDRSS transmission was approximately 80% efficient for high-priority data.

2.1 Scintillator Detectors

Each SuperTIGER module has three layers of Scintillation Detectors, each layer consisting of two separate counters. Each counter has its own light-tight aluminum enclosure. The bottom of each enclosure is a Rohacell composite with aluminum face sheets attached, while the top of each counter is a 0.127 mm aluminum foil stretched over a frame. This lightweight composite and foil top were chosen to reduce the interactions of cosmic-ray nuclei within the detector. Each scintillator detector has a 116.2 cm $\times$ 116.2 cm $\times$ 1cm radiator of Eljen EJ-208B plastic scintillator. A layer of reflective mylar lies above and below each radiator to

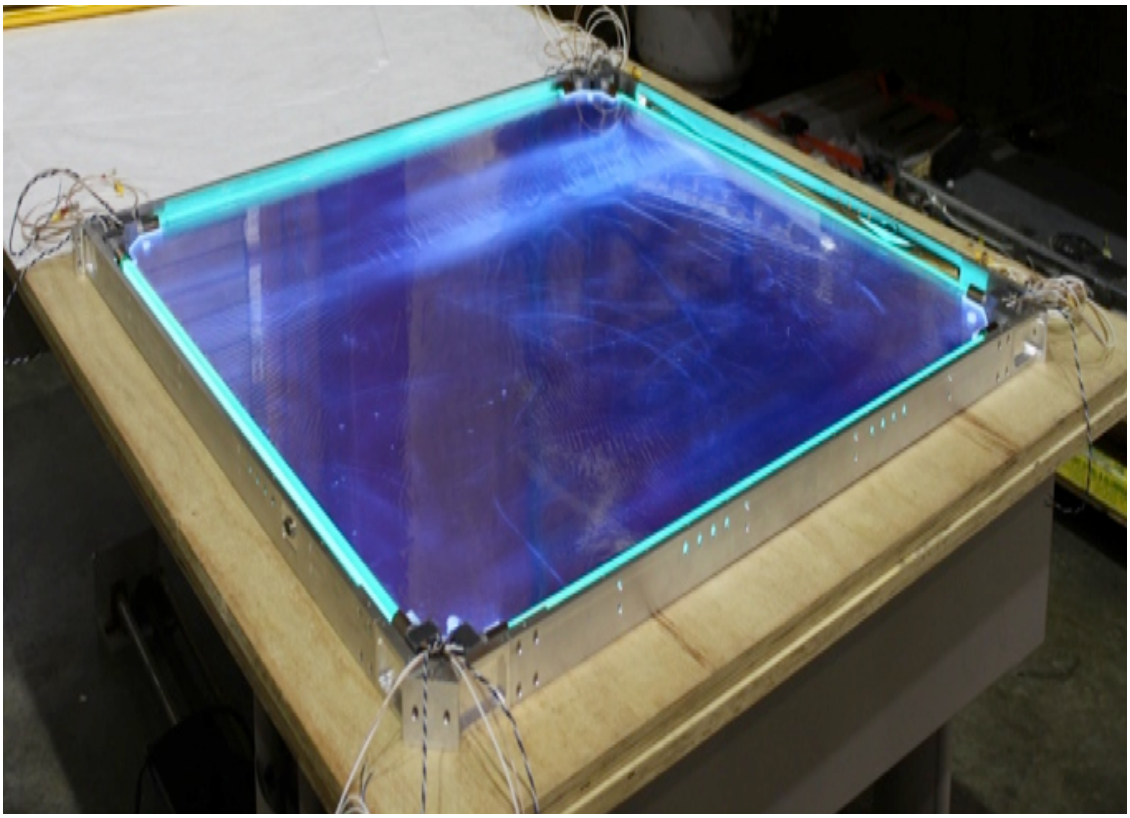

Figure 2.4: A Scintillation detector with the radiator and WLSBs clearly visible.

reflect back into the radiator any photons that escape. Four Eljen EJ280 Wavelength-shifter Bars (WLSB) surround the four sides of the detectors. Each WLSB has a Hamamatsu R1924A photomultiplier tube (PMT) epoxied to each end.

The size of the WLSBs and other electronics results in a ∼6.4 cm gap between the active areas of the side-by-side detectors in each scintillator layer. The SuperTIGER flight radiators were selected to have a relatively uniform thickness (<0.5%/cm thickness gradient over more than 90% of the surface, with a mean gradient of <0.25%/cm and a maximum gradient of <1.0%/cm, as measured at the factory with an ultrasonic gauge, and are the largest sheets available with this uniformity.

Blue scintillation light is created within the radiator when a cosmic-ray nucleus travels through the material. A fraction of this light is reflected internally to the edges of the

detector, where the blue photons are absorbed by the WLSBs. This light is re-emitted isotropically in the WLSB as green photons, a fraction of which are light-piped down the WLSB to the PMTs at the end of the bar. This configuration allows for the measurement of light from a large area of scintillator with a small number of PMTs.

The signals from the scintillators are used to determine the charge of particles below the threshold of the aerogel Cherenkov counter, to identify particles that interacted within the instrument, and for the in-flight event trigger. Each module had a separate event trigger, and if the signal was above a set threshold in S1 and either S2 or S3, the event would be recorded. The trigger threshold was chosen to trigger on a vertically incident $_{10}$Ne particle at the center of the radiator. Each scintillator FEE board had two independent coincidence triggers. For a scintillator detector with all 8 fully functional tubes, each coincidence channel summed the signal from one tube from each corner of the detector, and triggered if the sum of these four tubes was above the threshold. This threshold was scaled down as appropriate for those coincidence triggers with only three or two functional tubes.

2.1.1 Scintillator Readout System

The scintillator PMTs were hand-selected from the R1924A PMTs purchased for SuperTIGER for their higher gain and sensitivity to light in green wavelengths. Each PMT was potted in a base that provided positive high voltage and included radically tapered voltage dividers. The relative voltage ratios were: K-D1 1, D1-D2 0.17, D2-D3 0.17, D3-D4 0.24, D4-D5 0.24, D5-D6 0.34, D6-D7 0.34, D7-D8 0.5, D8-D9 0.67, D9-D10 1.0, D10-HV 1.0. This tapering, developed by the SuperTIGER group at Goddard Space Flight Center, gave a nearly linear response over a wide dynamic range. This range covered signals as large as 2×10^5 photoelectrons (pe) and an effective dynamic range of 2×10^4. This was sufficient to cover the charge range $10 \leq Z \leq 60$, including variations in the amount of light reaching

each PMT due to incidence angle and position. The flight HV values were chosen to take advantage of this dynamic range, and typical values were 650-800 V. Each scintillator base also included a preamplifier board that shaped the PMT signal before feeding it to the FEE board. Each scintillator PMT was wrapped with a single 0.1 mm thick layer of μ-metal foil to reduce the effects of the Earth's magnetic field, which varies with instrument location and orientation.

These PMTs were mounted to the aluminum detector box using a compliant RTV. The instrument was exposed to more stress due to transportation and thermal changes than expected before the flight. After the SuperTIGER thermal vacuum test at NASA's Plum Brook Station and transportation to the Columbia Scientific Balloon Facility (CSBF) in Palestine, TX, we discovered that the vacuum seal on two PMTs had been broken. These PMTs were replaced prior to shipment to Antarctica. However, upon arrival at the Long Duration Ballon Facility at Williams Field, Antarctica, 14 tubes (out of a total of 96 Scintillator PMTs) were discovered to be broken or unresponsive. Four of these PMTs were located in one of the top (S1) scintillator boxes on Module 2, so that box was replaced with the flight spare scintillator detector. One other S1 tube was replaced before launch. The other nine tubes could not be accessed without disassembling most of the instrument, so these tubes were not connected to a HV supply. HV caps were installed onto each HV wire that would have gone to these tubes to prevent arcing. The high voltage settings for each of these channels was reduced as much as possible (400 V below the HV board setting) as well to prevent arcing. In one case, a dead PMT required us to move a PMT signal cable to a different FEE board channel to ensure that the FEE board would trigger properly for coincidence detection. One more PMT stopped functioning approximately 18 hours into the SuperTIGER flight. Of the ten dead tubes, 1 was in S1 on Module 1, 6 were in S2 (4 on Module 1, 2 on Module 2), and 3 were in Module 2 S3. The scintillation detectors

were designed for graceful degradation, so these missing PMTs did not significantly impact in-flight performance.

2.2 Scintillating Fiber Hodoscope

The scintillating fiber hodoscope measures the trajectory of particles as they pass through the SuperTIGER instrument. Each module's hodoscope consists of two planes, one on the top and one on the bottom; each plane consists of 3 layers–one long layer, with active area ∼2.4 m long × 1.16 m wide, and two short layers side by side, each with active area 1.16 m × 1.16 m. These layers provide an (x,y) position of the particle at both the top and bottom of the instrument, which can be used to determine the trajectory. Each long fiber layer consists of ∼ 828 1.4 mm square fibers. These fibers are grouped into 144 "tabs" of 6-7 contiguous fibers, with 12 adjacent tabs grouped together in a "segment". The short fiber layers each have ∼ 1160 1 mm square fibers, also grouped into 144 "tabs" of 8-9 fibers. There are twelve segments on each short and long fiber layer. The hodoscopes use a coded readout system originally developed for TIGER to limit the number of Photomultiplier Tubes (PMTs) required. On the "coarse" side of each fiber layer, each segment of adjacent twelve fiber tabs is read out by a single PMT. A single tab from each segment goes to each of 12 PMTs on the opposite "fine" end of the layer. A "good" event gives a signal in the PMT on both the fine and coarse ends for both a long and short layer. Since each tab is read out on both ends, identifying the coarse and fine tube registering a "hit" signal for an event allows us to identify which tab was triggered. This method allows for the 144 tabs to be read out with just 24 PMTs, giving a segmentation resolution of 0.8cm and a root-mean-square resolution of $0.8/\sqrt{12} = 2.3$ mm.

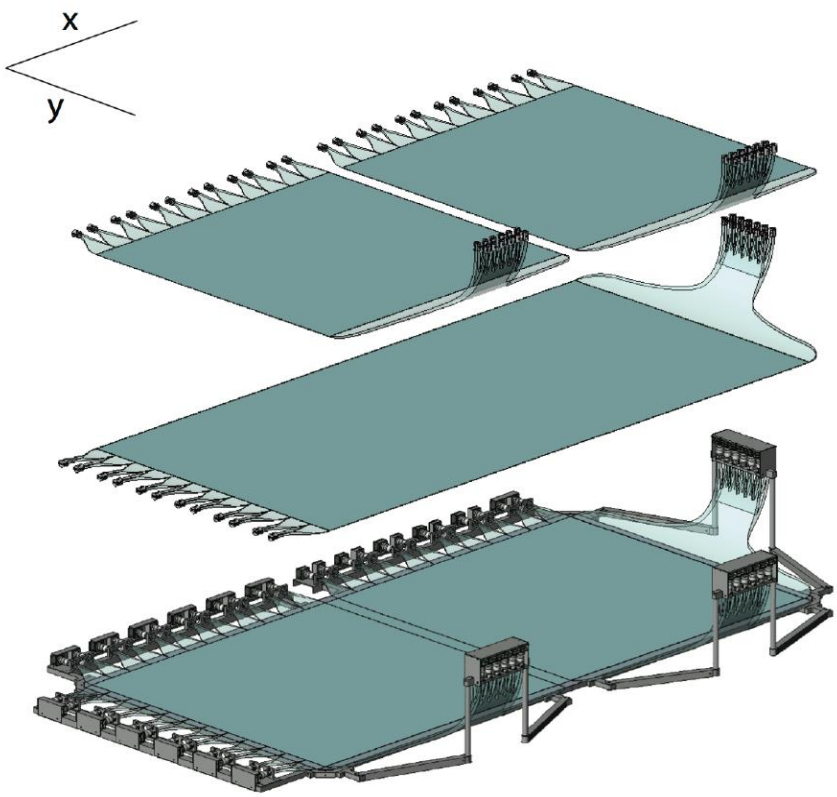

Figure 2.5: Drawing showing the components of a single hodoscope plane, expanded vertically. The short layers are shown on top, with a long layer below, and the combined short and long layers on the bottom. The coarse ends are on the top and left, while the fine ends are on the bottom and right.

2.2.1 Hodoscope Fibers

The fibers were made at Washington University out of a polystyrene plastic with two types of scintillator dyes (primary butyl-PBD 1% by mass and secondary dimethyl-POPOP 0.2% by mass) mixed in. The fibers were drawn over a slowly rotating aluminum wheel, then glued together into ribbons with Arathane 5753 adhesive and cut to size. The long fibers were then glued to a 1.59 cm thick Rohacell/Aluminum composite substrate, and the short layers were in turn glued to the top of the long layers. The layers were arranged on the substrate such that the active area of the fibers lies directly above/below the active area of the scintillation counters when in the instrument stack.

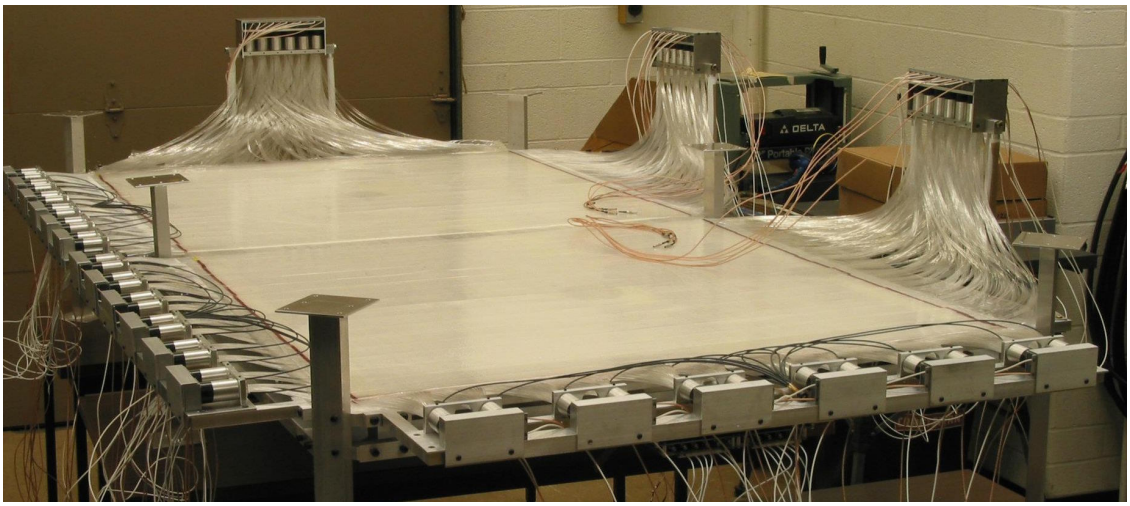

Figure 2.6: Hodoscope Fibers and PMTs for one plane.

When a cosmic-ray particle travels through the fiber, it excites the polystyrene molecules in the fiber, which transfer energy non-radiatively to the primary dye. The primary dye then radiates this energy as ultraviolet (UV) light, which is in turn absorbed by the secondary dye, which re-radiates it as blue light. This blue light is then light-piped through the fiber to the PMTs at both ends. To reach a PMT, the light may have to travel up to 2 m on a short layer or 3.2 m on a long layer. Therefore, prototype fibers were tested with a ^{90}Sr electron source to determine whether the light output and attenuation lengths were suitable for use. Since a vertically incident $Z = 10$ particle gives $\sim$80 times as many photoelectrons in the PMT as β-particles from the ^{90}Sr source, it was determined that these fibers had the appropriate attenuation properties after scaling the ^{90}Sr attenuation length results. More detail on the attenuation properties derived from in-flight data can be found in Appendix A.

To account for size variations and bends in the fibers, each layer was mapped before gluing the short layers to the long layers, and these maps were used to translate fiber positions into the instrument coordinate system. The hodoscope mapping is discussed at length in Appendix A.

2.2.2 Hodoscope Readout

The hodoscopes use 2.54 cm diameter Hamamatsu R1924A Photomultiplier tubes, the same model used for the scintillation counters. The hodoscope PMTs were selected from those PMTs not used for the scintillation counters, and banks of 12 were chosen such that the PMTs in a single bank had shown similar gain responses during testing. PMTs with higher gains were selected for the long fiber layers, to further counter the effects of attenuation in the long fibers. The twelve PMTs on each side are read out by a single Front-End Electronics (FEE) board and powered by two high voltage (HV) trim boards (with EMCO CA12P 1250V power supplies). The HV trim boards allow for the voltage on each PMT to be set independently (within ∼400V of the set power supply voltage).

Each PMT was tested with a blue LED at various voltage levels to determine the tube gain before being selected as either a scintillation counter, long-layer hodoscope, short-layer hodoscope, or spare tube. Each hodoscope tube is attached to a custom base, which provides power and contains a linear base circuit. This circuit was inspected visually and "burned in" by running at 1250 V at 60° C for 24 hours before being attached to a PMT. After verifying that the PMT and base work properly using a blue LED, the PMT and base are potted with RTV 627. The hodoscope bases each have a tan colored LEMO cable to carry the PMT signal to the FEE board and a white HV cable that is hard-wired and potted to the HV trim board.

2.3 Cherenkov Detectors

The Super-TIGER Cherenkov counters are used for identifying the charges of cosmic-ray nuclei that pass through the experiment. For events with energy below the C0 threshold (2.5 GeV/nucleon or 3.3 GeV/nucleon, depending on the index of refraction n of the aerogel,

1.04 or 1.025, respectively), Z is determined by a combination of C1 and the scintillator signals. Above the C0 threshold, C1 and C0 are used. The Super-TIGER Cherenkov counter design concept (light integration box and choice of radiators) was based on the Cherenkov counters successfully utilized in the TIGER experiment.

Each Cherenkov counter has an aperture of 118 cm $\times$ 240 cm and is 20 cm tall. For ease of handling during integration and recovery operations, each Cherenkov box can be split into two half-modules, each measuring 118 cm$\times$120 cm$\times$20cm. Each Cherenkov counter uses 42 Hamamatsu R877-100 12.7 cm (5 inch) diameter photomultiplier tubes (PMTs). All inside surfaces of the counters are covered with a layer of 0.25 mm-thick high reflectance GORE^{TM} DRP material. This material has a reflectivity of better than 93% and is a nearly Lambertian surface, which is isotropizing for directional Cherenkov light. The combination these two properties of the reflective lining maintains a relatively uniform and position-independent detector response (<25% for the acrylic C1) within this large-area counter. The Cherenkov radiators sit on an ultra-low-density composite, closed-cell Rohacell substrate with 0.1 mm Aluminum face sheets, chosen to minimize the probability of cosmic-ray particles interacting within the instrument. Each Cherenkov half-counter has a lid of thin aluminum foil stretched over a frame, similar to the scintillator detector lids.

2.3.1 Cherenkov Radiation

Cherenkov radiation is emitted when a charged particle travels through a dielectric medium at a velocity greater than the speed of light within that medium. This is the electrodynamic analogue of the shockwave (or sonic boom) created by an object traveling faster than the speed of sound in a medium. Light is emitted if the speed v exceeds the local speed of light:

$$v > \frac{c}{n(\omega)} \tag{2.1}$$

where $n(\omega)$ is the frequency-dependent index of refraction of the medium in question. The index of refraction thus determines the minimum threshold energy. The SuperTIGER Acrylic Cherenkov Counters (C1) have an index of refraction $n = 1.49$, while the Aerogel Counters (C0) have either $n = 1.04$ or $n = 1.025$. These indices correspond to energy thresholds of 300 MeV/nucleon for C1, and 2.5 GeV/nucleon and 3.3 GeV/nucleon for C0. Cherenkov emission is emitted at a characteristic angle relative to the particle's trajectory:

$$\theta_{Ch} = cos^{-1}\left(\frac{1}{\beta n(\omega)}\right) \tag{2.2}$$

To prevent total internal reflection, the top and sides of each C1 radiator were soda-blasted to roughen the surface. On the TIGER instrument, the bottom of the C1 radiators was roughened as well. The bottoms of the SuperTIGER radiators were not roughened due to an oversight.

The energy lost due to Cherenkov radiation as a function of pathlength is given by:

$$-\left(\frac{dE}{dX}\right) = \frac{Z^2}{c^2}\int_{\beta>1/n(\omega)} \omega\left(1 - \frac{1}{\beta^2 n^2(\omega)}\right) d\omega \tag{2.3}$$

The light collected by the SuperTIGER Cherenkov detectors includes contributions from Cherenkov emission as well as a small contribution (<5%) from scintillation light within the Cherenkov radiators. The integral above is bounded by the frequency dependence of the PMT response, and the transmission of the Cherenkov radiator. Assuming that the index of refraction is approximately constant over the frequency range the PMTs are sensitive to $(n(\omega) = n)$, the total amount of light detected can be written as:

$$L_{Ch} = KZ^2\left(1 - \frac{1}{\beta^2 n^2}\right) \tag{2.4}$$

Here, K is a constant unique to each detector. The Cherenkov signal thus depends on the particle's charge, Z, and a function of the particle's velocity. At the Cherenkov threshold ($\beta = 1/n$), this function goes to 0, and at large velocities, this function approaches a constant.

2.3.2 The SuperTIGER Cherenkov Radiators

In the Aerogel (C0) counter, 4 blocks of aerogel with nominal dimensions of 55 cm $\times$ 55 cm, each 3 cm tall, were placed in a 2 $\times$ 2 array to form the radiator for each half-module. The Super-TIGER aerogel blocks were purchased in the early 1990s from Airglass AB in Sweden, and were maintained in a protective-dry nitrogen storage environment at Caltech until installation in the experiment. To improve light yield, each aerogel block was baked at high temperature to eliminate any absorbed aerosol materials or remaining interstitial alcohol, using a technique originally developed for the IMAX experiment (Labrador et al., 1993). To protect the aerogel blocks from potential stresses due to deformation of the counter or shock during shipment, launch, landing, and recovery, each block was placed individually on a thin composite pallet covered in the same GORE^{TM} DRP used to line the inside of the counter. These blocks are held in place on the pallets by a layer of low-density UV-transparent polyethylene terephthalate, using a technique adapted from the BESS/BESS-Polar experiment (Asaoka et al., 1998) (Hams et al., 2005). Three of the four half-modules used aerogel blocks with index of refraction $n = 1.043$ (12 blocks total), while the remaining half-module used blocks with index of refraction $n = 1.025$ (4 blocks total). The Cherenkov energy thresholds for the aerogel half-modules are 2.5 GeV/nucleon and 3.3 GeV/nucleon, respectively.

In the Acrylic (C1) counters, the radiators are 116 cm $\times$ 116 cm sheets of 1.28 cm-thick UV-transparent acrylic in each half module. These radiators, which were cast by Spartech/Polycast, had a bis-MSB wavelength shifter dye added (25mg/L). This material has

Figure 2.7: One Aerogel block after installation in the C0 detector.

an index of refraction of $n = 1.49$, giving a Cherenkov energy threshold of 0.3 GeV/nucleon. The wavelength shifter absorbes the UV Cherenkov photons and re-emits this light in wavelengths visible to the PMTs, increasing the amount of the radiation that could be collected and reducing the angle-dependence of the detector signal. The wavelength shifter also provides additional isotropization of the wavelength-shifted Cherenkov photons. Furthermore, the top and sides of the radiators were soda-blasted to eliminate total internal reflection on those surfaces and allow the Cherenkov photons to leave the radiator and be diffused in the light-integration box. This soda blasting was done at GSFC with rented soda-blasting equipment.

2.3.3 Cherenkov Readout System

Each counter uses a total of 42 Hamamatsu R877-100 5-inch diameter high quantum-efficiency PMTs. To reduce the effects of the geomagnetic field on PMT gain, a light-weight

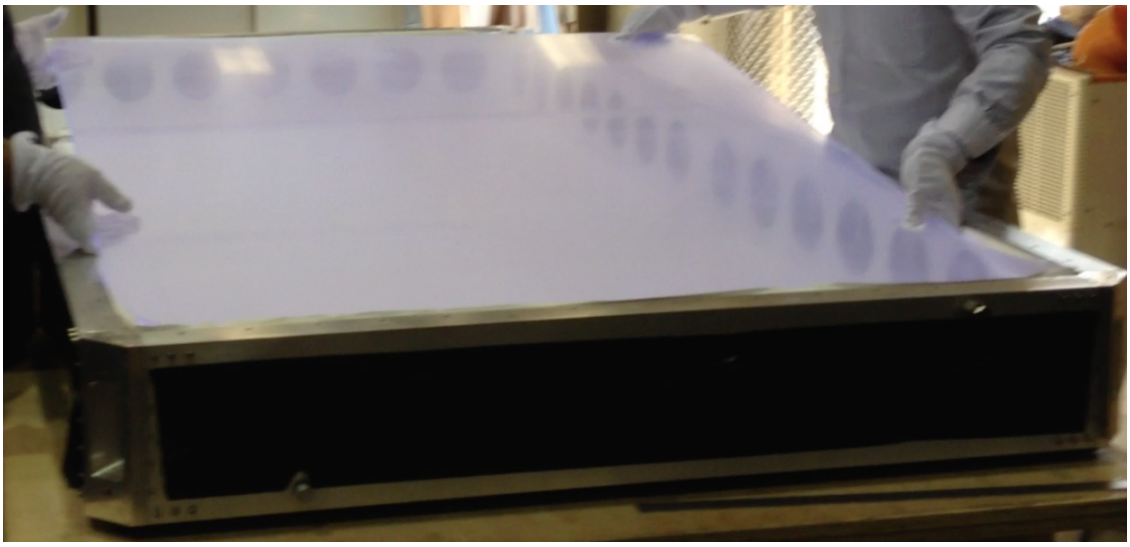

Figure 2.8: An Acrylic (C1) radiator being installed in the detector.

3.56 mm (0.14 inch) thick μ-metal shield, manufactured by Amuneal, is wrapped around each PMT. In addition, these shells also served as a mechanical mounting flange to the counter box and provided the ambient light seal to the counter volume. These PMTs are mounted from the outside into circular cutouts in the side walls, with 7 mounted on each short side and 14 mounted on each long side of each rectangular module. The gain of each PMT can be adjusted with the use of a High Voltage (HV) trim circuit. The nominal flight voltages of each PMT were set individually and chosen based on the results of gain-curve characterizations and ground-based muon testing to normalize the response throughout the counter. Flight voltages ranged from 950 V to 1200 V. In the C1 counters, each PMT is attached to a 1250 V EMCO CA12P HV supply. In the C0 counters, the PMTs on the short sides of the rectangular box are attached to CA20P 2000 V HV supplies. On each C0 long side, the PMTs alternate between being attached to 1250 V supplies and 2000 V supplies. This distribution of PMTs was designed to ensure a graceful degradation of data quality in the event of a HV supply failure, as the 2000V supplies seemed to fail at a higher rate than the 1250V supplies in thermal vacuum testing.

The dynamic range required for the SuperTIGER Cherenkov detectors was determined with the help of a Geant4 Monte Carlo computer simulation (Hams et al., 2011). Since the light produced in the Cherenkov counters goes as Z^2, single-charge resolution over the range $10 \leq Z \leq 60$ requires a large dynamic range. To meet these requirements and ensure a linear PMT response over the entire range, strongly tapered voltage dividers were developed (the relative voltage ratios were K-G 1.0, G-D1 1.0, D1-D2 0.17, D2-D3 0.17, D3-D4 0.33, D4-D5 0.5, D5-D6 0.5, D6-D7 0.75, D7-D8 1.0, D8-D9 1.2, D9-D10 1.5, D10-HV 1.2). An integrated charge-sensitive preamplifier board was included in the base of each PMT. These bases allowed the Super-TIGER PMTs to detect from 10 to ∼200,000 photoelectrons with only a 2% non-linearity over that range. Each PMT signal was read out using two separate readout circuits, each read out using a 16-bit analog-to-digital converter (ADC). One channel had a high-gain amplifier and one had a low-gain amplifier. The signal from both readout channels was recorded onto the flight data disk, but only one channel for each PMT was telemetered down via TDRSS. The channel that was telemetered down was chosen to provide the maximum amount of information, so if the high-gain channel was fully saturated the low-gain channel was used.

2.4 High Voltage and Readout Electronics System

SuperTIGER employed a custom suite of electronics that both controlled the High Voltage (HV) for each individual PMT and recorded the individual PMT signals. The electronics suite also analyzed the signals and triggered a coincidence signal if the signal was above set threshold. A custom computer system handled data storage, transmission, and interface with the Support Instrument Package (SIP), which provided ground-to-air communications. Each scintillator half-module (consisting of 8 PMTs), bank of 12 hodoscope

PMTs, and group of 7 Cherenkov detector PMTs[1] was controlled by its own Front-End Electronics (FEE) board. Figure 2.9 shows a block diagram for an example (scintillator) FEE board. Both the scintillator and Cherenkov PMT bases included a charge-sensitive preamplifier board. The preamplifiers for the hodoscope detectors were located on the FEE boards themselves. Each PMT output was fed to a shaping amplifier with a time-to-peak of 1 μs and was then read out by a peak sensitive analog-to-digital converter (ADC). The hodoscope ADCs had 14 bit resolution while the Cherenkov and scintillator ADCs had 16 bit resolution. As noted above, the Cherenkov tubes were read out by two 16-bit ADCs, differing by a gain factor of $\sim$8. Fast-shaping amplifiers and comparators on the scintillator and some C1 FEE boards were used to send signals to a field-programmable gate array (FPGA) programmed with the trigger logic. As noted above, the sum of 4 tubes was compared to the threshold for each trigger channel, and the trigger was logically S1 AND (S2 OR S3). Light-emitting diodes (LEDs) were attached to each FEE board and allowed for functional testing of all the PMTs on each detector. Each scintillator and hodoscope FEE board was attached to two slave HV trim boards, while each Cherenkov FEE was attached to one. The HV system was designed to accommodate the required dynamic range of each detector. Each scintillator HV trim board provided power to 4 PMTs, while the hodoscope and Cherenkov HV trim boards provided power to 6 and 7 PMTs, respectively. Each individual HV channel could be adjusted over a range of $\sim$400 V below the supply voltage, which provided the ability to normalize PMT gains. The hodoscope and scintillator HV trim boards used EMCO 1250V CA12P HV power supplies, while the Cherenkov counters used both EMCO 1250V CA20P and EMCO 200V CA12P supplies, as described above. All HV connections used shielded Reynolds 600 cable. Scintillator and Cherenkov PMT cables used Reynolds 600 series connectors. Hodoscope HV connectors were "pig-tails" without connectors that were soldered directly to the HV trim board. The hodoscopes were therefore hard-wired to their

[1]For C1, these groups of 7 were the adjacent tubes attached to one side of the Cherenkov half module; for C0, the 7 PMTs on each short side were one group, while each long side had two groups each consisting of alternating tubes. This was done to spread out the tubes powered by questionable HV supplies.

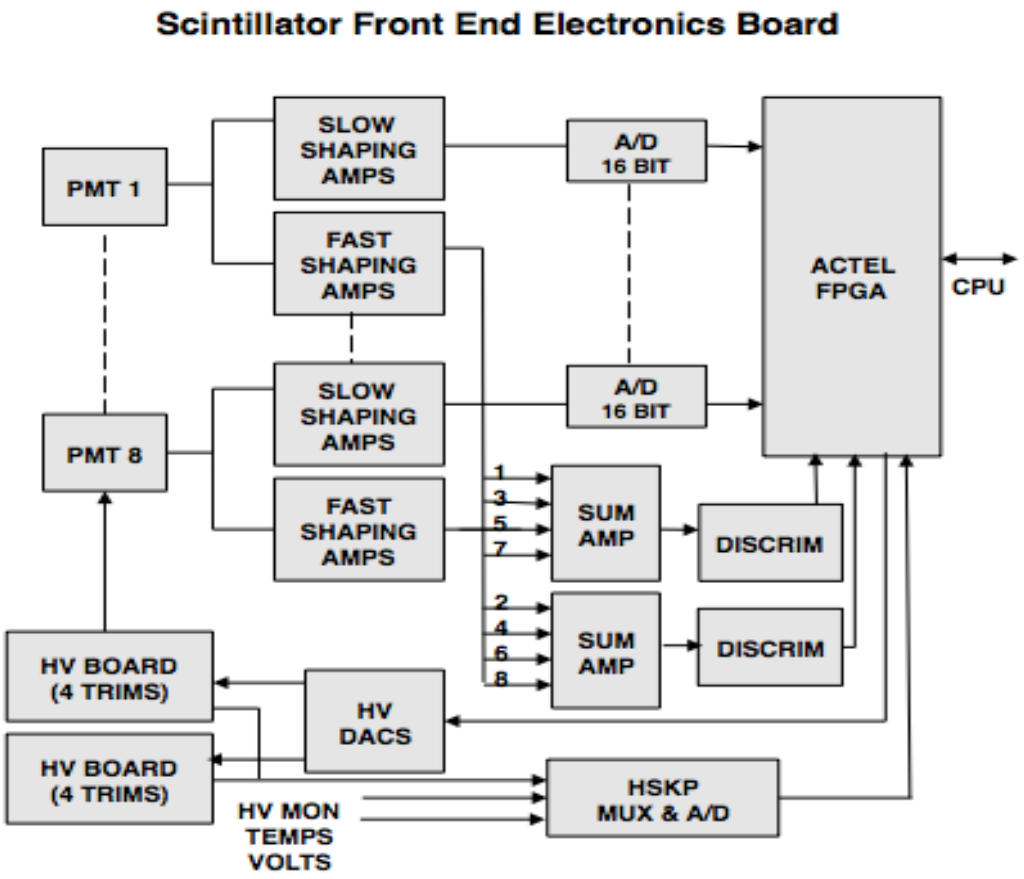

Figure 2.9: Block diagram of the SuperTIGER Scintillator FEE board. The Cherenkov and Hodoscope FEE boards are similar.

HV boards, which reduced the expense of HV connectors but meant that any modifications to the HV boards had to be done *in situ*. The HV trim board ends of each cable were potted to resist HV breakdown with a RTV compound and an epoxy (50-3150 RFR). Grounded copper plate over the HVPS and grounded copper mesh on the top and bottom of the trim circuit were added to reduce the local electric field penetrating the potting after the failure of many supplies at the SuperTIGER thermal vacuum test at NASA's Plum Brook Station. Before flight, every HV power supply was tested at temperatures and pressures expected during flight.

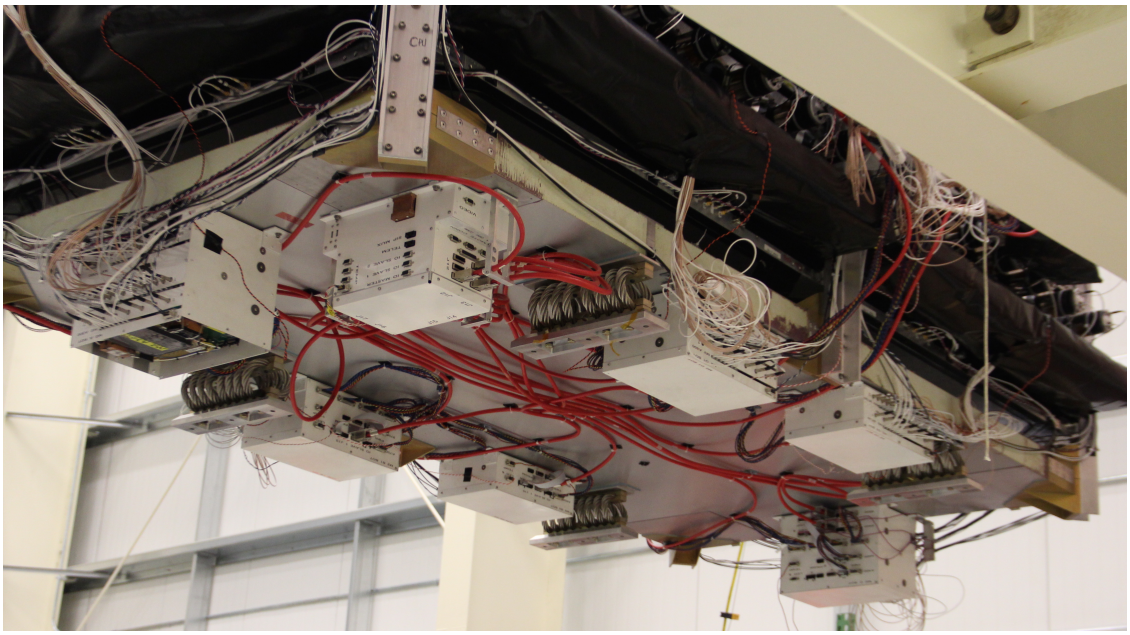

Figure 2.10: White electronics boxes are attached to the bottom of each module.

2.5 Flight Computer and Data Transmission

Each SuperTIGER module had its own CPU, each with a data disk and a root disk. All four disks were Intel 320 series solid state disks (SSDs). The data from both modules were passed through a multiplexer board located on Module 1 for telemetering down through a high-gain TDRSS (Tracking and Data Relay Satellite System) antenna. This high-gain antenna had a maximum speed of 90kbps. A 5kbps omnidirectional TDRSS antenna and an Iridium antenna were also used. Each module also had an S-band transmitter with a downward lobe antenna that was used when within line-of-sight (LOS) of the Long Duration Balloon Facility at Williams Field near McMurdo. These LOS antennae could accommodate data rates of up to 150 kbps. Command uplinks were available with all radio systems, but when outside of LOS all commanding was done using the Iridium uplink. The Iridium uplink was chosen despite its high latency because it was constantly available, while the TDRSS uplink required scheduled commanding windows. The commands sent from the ground were small packets of information and, for the most part, few and far between, so the Iridium

link was sufficient. Initial tuning and calibration of the instrument was done during the first several hours of flight, while the payload was within LOS, so the LOS uplinks were used.

During flight, the average event rate was ∼30 events/second. Full events were recorded by the flight software on the data disk SSDs, but TDRSS events were compressed in size. The size of each event telemetered via TDRSS was 398 bytes, which included the five brightest hodoscope PMTs on each side (with 12 bit resolution instead of the nominal 14 bits; the remaining bits were used to specify PMT channel), either the high or low gain Cherenkov signal (with 1 of the 16 bits used to specify which gain channel was used), and all of the scintillator PMT signals (with 16 bit resolution). Housekeeping events, that included information on current HV values, data rates, and temperatures, were telemetered every 4 minutes while there was an active downlink. These readings were used to watch for signs of HV power supply failure and adjust the voltages in flight.

Priority Scheme

Events were telemetered based on a priority scheme that assigned high priority to events whose detector signals exceeded those expected of vertically incident $Z \approx 22$ particles. We assigned a priority threshold to each scintillator detector and the Acrylic (C1) Cherenkov detector. Each priority threshold could be set individually via a command in flight, and we changed the priority threshold slightly after the data disk failure to ensure that all Z≥22 events were telemetered. If an event was above the high-priority threshold in S1 and one other detector, it was classified as a high-priority event. In addition, every 100th event was classified as high-priority regardless of whether or not it had any detector signals above the threshold.

The priority scheme was as follows for data telemetered from SuperTIGER: first, "reply" events that included confirmation of commands received or error messages were sent[2]. Then, the various housekeeping events were telemetered, with sensors housekeeping (voltage and temperature values), scalers housekeeping (data rates), and miscellaneous housekeeping (threshold values, etc.) were sent in that order. Pedestal calibration events were then sent. Then high-priority data events were telemetered. Finally, if there were no other events to send, low-priority data events were then sent.

2.6 Power System and Gondola

SuperTIGER utilized a photovoltaic (PV) power system consisting of two strings of 80 SunPower C-60 mono crystalline silicon cells connected in parallel. The cells of each string were connected in series and laminated onto substrates by Alain Chuzel of SunCat Solar. Each 80-cell string consisted of two 5x6 cell arrays and one 4x5 cell array, which was connected in series and mounted on the same plane. To protect against cell failure, bypass diodes were connected to each contiguous group of 10 cells, and a blocking diode was installed on top of each 80-cell array. These two arrays were mounted on the sun-pointing side of the gondola at an angle of $\sim$70°to the zenith. Other PV arrays were attached by CSBF to the SuperTIGER gondola to power the balloon electronics and telemetry system. Figure 3.1 shows the SuperTIGER instrument with PV arrays installed. The PV arrays fed into a Morningstar TriStar MPPT-45 Charge Controller operating in the 24 V mode, and charged three pairs of Panasonic LC-X1220P lead acid batteries. The voltage of the PVs as measured at the input was stable at 42 $\pm$ 2V. The output of the charge controller was fed into a relay circuit board for each module, which could be controlled by discrete commands. The 24 V main power fed two DC-DC converters on each module that provided the lower

[2]This caused an issue when the data Solid State Drives failed, as the error messages were sent rather than any data for several hours. See Appendix B for more details.

voltages used by the CPUs, FEE boards, and HV trim boards. The system provided $\sim$ 240-260 W of power to the instrument throughout the flight.

A rotator, provided by CSBF, kept one side of the SuperTIGER payload pointed at the sun. This allowed for only a single PV array to be used for powering the instrument, reducing the cost and weight of the payload. The rotator was attached to the four straps that connected to the gondola, below the parachute and termination package of the balloon. The rotator was accurate to within a few degrees, which was more than sufficient to provide constant power to the payload.

During flight, the two SuperTIGER modules rested on top of a 4.3 m $\times$ 3.4 m gondola. The gondola was designed to be lightweight but still satisfy CSBF structural requirements and provide protection for the detectors on landing. Aluminum C-channels formed the deck, and space frame elements made of 3 mm-walled aluminum tubing with machined end fittings provided the diagonal supports. With electronics and the extension of hodoscope fibers, each module had an area of 1.86 m $\times$ 3.1 m. Each module was attached to a 7.5 cm thick honeycomb pallet, which was in turn attached to the gondola deck using shock-absorbing cable isolators. Six C-channel uprights were attached to machine fittings that were bonded to the honeycomb structure, and the detector stacks were built up and attached to these uprights. This allowed the modules to be fully integrated and tested before being installed on the gondola. The gondola was powder coated white by Lone Star Powder Coating in Palestine, TX. Based on a comprehensive thermal model developed by Scott Cannon of New Mexico State University Physical Science Laboratory, a passive thermal control strategy was employed. The two SuperTIGER modules were covered by a single box of foam insulation, with 2.54 cm of Techlite insulation on top, 5 cm of Styrofoam insulation on the sides and 2.54 cm of Styrofoam insulation on the bottom. This foam box was covered by a layer of aluminized mylar with the mylar side out. The box and mylar were installed during pre-flight preparations in Antarctica.

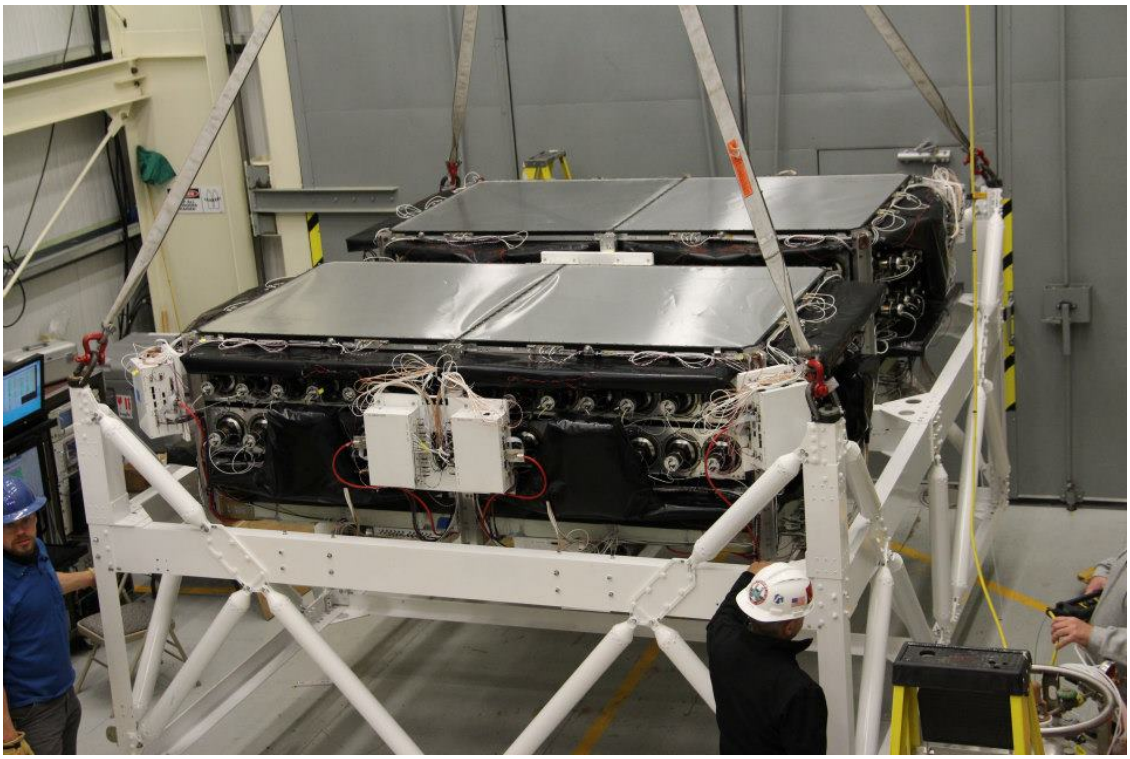

Figure 2.11: The two SuperTIGER modules after installation on the gondola.

2.7 Integration and Testing

The SuperTIGER hodoscopes were developed and built at Washington University in St. Louis (WUSTL), while the scintillators and Cherenkov detectors were built at NASA Goddard Space Flight Center (GSFC). The California Institute of Technology (Caltech) provided the aerogel radiators for the C0 detectors, and helped install them in the counters at GSFC. The electronics, HV, and power system were also developed at WUSTL. Integration of the whole instrument took place in early 2012 at GSFC. The Gondola was assembled initially at GSFC, then disassembled and shipped to NASA Columbia Scientific Balloon Facility (CSBF) in Palestine, TX.

During initial testing before integration, each FEE board, HV trim board, and PMT was thermal cycled after potting. The PMTs, bases, and FEE board were tested together

Figure 2.12: The SuperTIGER instrument being placed into the B-2 Thermal Vacuum Chamber at NASA Plum Brook Station.

with a blue LED during separate thermal cycle (-35C to +55C) and vacuum tests, but no initial thermal vacuum test was performed.

SuperTIGER had a full-system thermal vacuum test at NASA Glenn Research Center's Plum Brook facility in Sandusky, OH, on June 26-30, 2012. For this test, the two modules were stacked on top of each other on a mechanical support structure, shown in Figure 2.12. During this test, the entire system was brought to pressures and temperatures that were expected during flight. During the monitoring, suspicious drops in the high voltage reported by various PMTs and HV trim boards were discovered, particularly at cold temperatures. This was a sign of HV arcing in the near-vacuum of balloon altitude. A large number of HV power supplies ($\sim$49 out of 96) displayed signs of arcing. After this test, copper plates

over the HVPS and copper mesh on the top and bottom of the trim circuit to reduce the local electric field was added, and every HV power supply was tested at pressures and temperatures[3] expected during flight. Previously, vacuum tests that were done were performed in a full vacuum (or as close as the equipment would allow) rather than the ∼2-4 torr typical of balloon altitudes. The combination of the low pressure and cold temperature is thought to be responsible for the failure of the HV supplies.

After the Plum Brook test, SuperTIGER was integrated with the CSBF electronics and telemetry system in Palestine, TX. The SuperTIGER gondola was powder coated and then re-assembled. A full system checkout and compatibility test was carried out on August 10, 2012. After the compatibility test, the gondola, PV panels, and support equipment were shipped to Antarctica. Once the HV trim boards had been fixed and re-tested, they were added back to the electronics boxes. In early October, the SuperTIGER modules were shipped via commercial air to Christchurch, New Zealand, where they were in turn flown by the United States Antarctic Program to McMurdo Station.

[3]The Hodoscope HV boards were only tested to ∼-10°C due to limitations imposed by hard-wiring the HV trim boards to the instrument.

Chapter 3

The SuperTIGER Antarctic Balloon Flight and Recovery

SuperTIGER was launched on a NASA Long-Duration Balloon (LDB) at 20:45 UTC on December 8, 2012 from Williams Field, near McMurdo Station, Antarctica. SuperTIGER flew for 55 days, 1 hour, and 34 minutes, terminating on February 1, 2013 UTC. The payload made two and three-quarters orbits with the circumpolar vortex around the South Pole, and flew at a mean atmospheric depth of 4.4 g/cm^2. The payload was launched by personnel from NASA's Columbia Scientific Balloon Facility (CSBF) in Palestine, TX. After the flight, NASA announced that the flight broke two NASA records: the longest Antarctic Science Flight for a Heavy-Lift balloon, previously held by CREAM I with a 41 day, 21 hour, and 31 minute flight in 2003-2004 (and, before then, by the 32 day flight of TIGER in 2001), and the longest flight for a Heavy-Lift Balloon, previously held by the Super Pressure Balloon test in 2008-9 with 54 days, 1 hour, and 29 minutes. A few hours before termination, the instrument had been turned off entirely in preparation for termination, but the winds shifted and the instrument trajectory turned northward, so we were given approval to power the system back on again. We got an additional ∼3 hours of data from Module 2 (this is discussed further in Section 3.2.3) before being told to turn the system off again. The flight ended at 20:17 UTC on February 1, 2013. The instrument came to rest at 82.24°S 81.91°W, ∼1625 km

Figure 3.1: SuperTIGER on the launch vehicle before flight, December 2012.

from McMurdo and ∼600 km from the nearest long-term US camp at WAIS Divide. While recovery was initially planned for January or February 2013, terminating relatively late in the Austral summer season in a remote location meant that recovery had to be postponed until the next Austral summer. In January 2014, an unsuccessful recovery attempt was made that ended in an overflight of the payload, and discovered that the payload was upside down. The payload was finally recovered in December 2014-January 2015 and returned to the continental United States in April 2015.

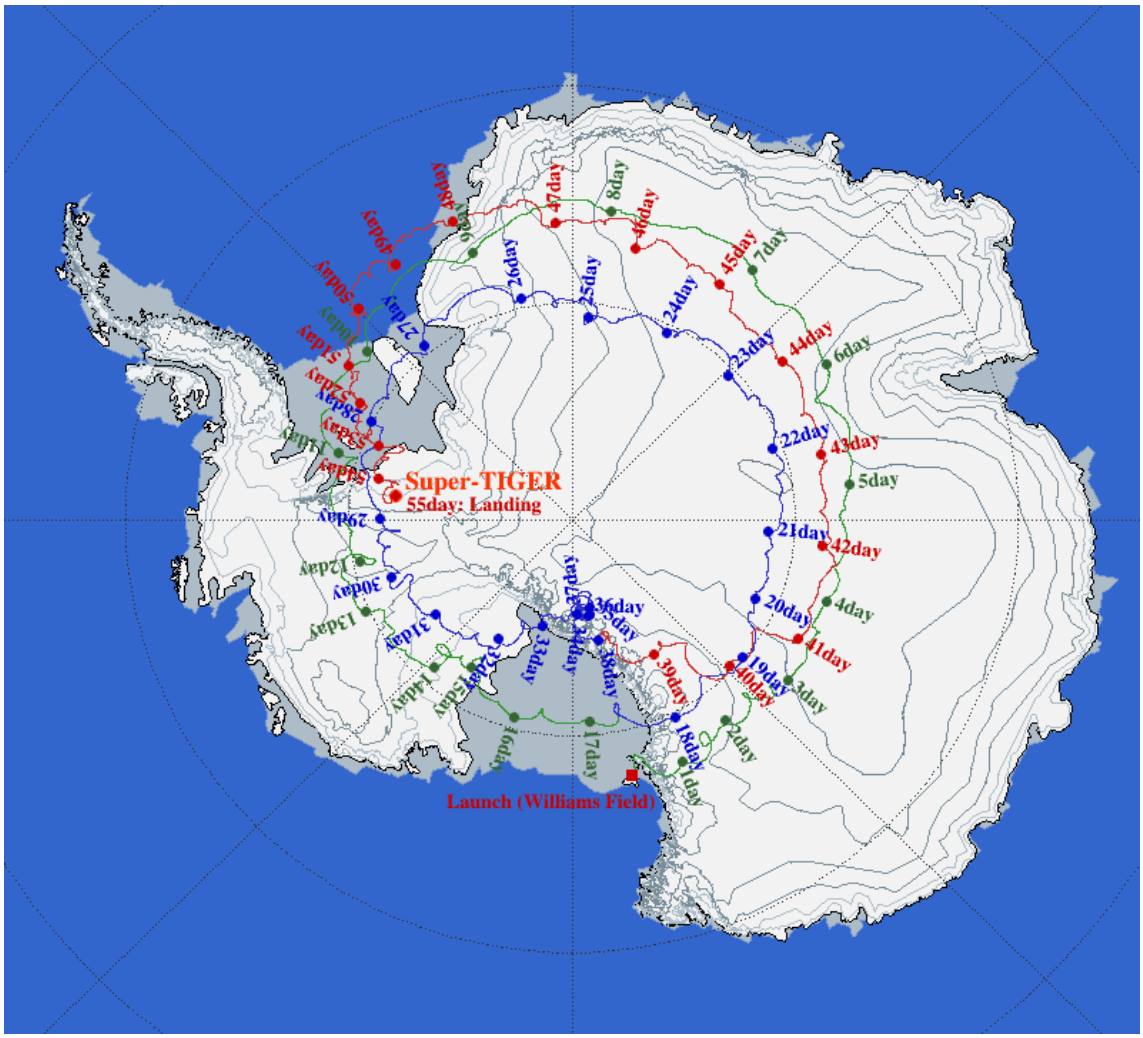

Figure 3.2: The SuperTIGER flight track.

3.1 2012-13 Flight Overview

Final preparations for the SuperTIGER flight were made at the Long Duration Balloon Facility (LDB) at Williams Field, Antarctica, ∼10 km from McMurdo Station. The gondola was re-assembled, the modules were installed on the gondola deck (after replacing one S1 counter and another scintillator PMT), ground-based muon testing was used to calibrate the instrument for flight, and another compatibility test verified that the instrument would work with the CSBF balloon and telemetry hardware. SuperTIGER was declared flight-ready on December 3, 2012 local (NZDT) time. After waiting for suitable weather, the CSBF

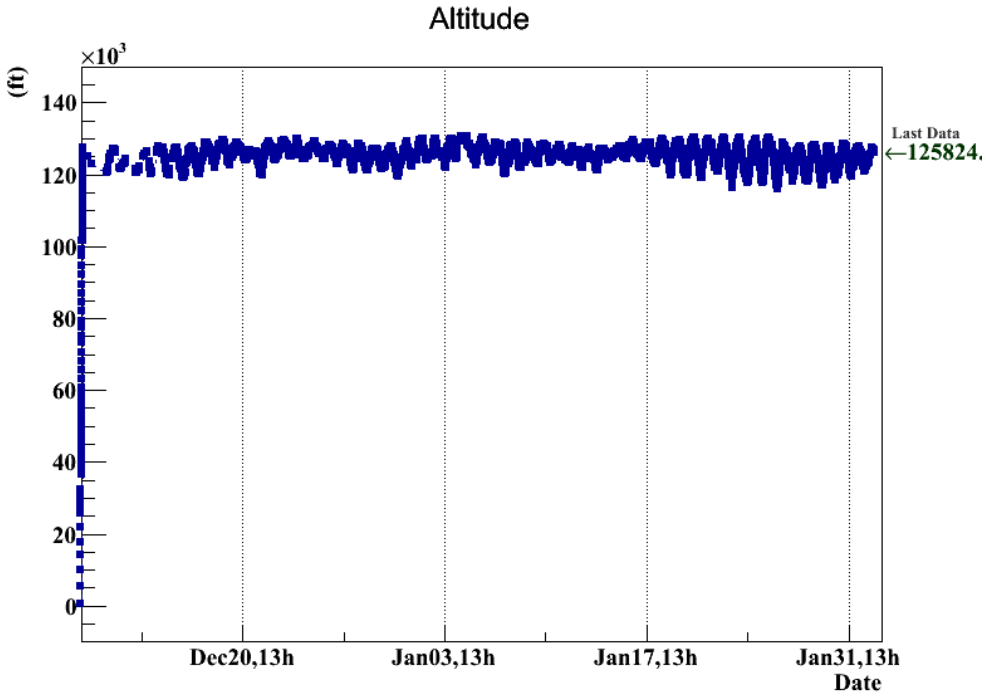

Figure 3.3: Balloon Altitude throughout the SuperTIGER flight. The diurnal variations are due to the angle of the sun in the sky.

meteorologist informed members of the team that there would be a launch opportunity at ∼1000 local time on December 9.

SuperTIGER was launched at 0945 local time on December 9 (20:45 UTC December 8), 2012. Photographs of the launch can be seen in Figure 3.4. The trajectory of the balloon can be seen in Figure 3.2. After launch, there is no way to control the path of the balloon, and the payload is at the mercy of the winds. However, the circumpolar vortex that sets up around the South Pole during the Austral Summer ensures that, despite day-to-day excursions and loops, the general trend is a counter-clockwise rotation around the pole. The altitude throughout the flight can be seen in Figure 3.3. The day-to-day variations are due to diurnal variations in altitude due to the thermal expansion and contraction of the balloon.

Figure 3.4: SuperTIGER Launch photos. Clockwise from top left: The SuperTIGER payload, launch vehicle, and inflated balloon; the balloon after release; the balloon and payload during ascent; the payload immediately after launch.

For most of the flight, data were telemetered down using the TDRSS (Tracking and Data Relay Satellite System) high-gain antenna. However, when the payload was within line-of-sight (LOS) of LDB, S-band transmitters on each module provided a data downlink (at a much higher data rate than the TDRSS antenna) and a command uplink. SuperTIGER was within LOS of LDB for the first ∼48 hours of flight, allowing for the initial calibration and fine-tuning of the instrument. An additional ∼79 hours of LOS data was obtained on December 25-28 NZDT, 2012 when the payload came back into LOS after the first orbit. This second LOS phase was a valuable addition, since the LOS downlink has the bandwidth to telemeter essentially all of the data down in real time, whereas on TDRSS the high-priority events were telemetered first and the low-priority events were telemetered only as bandwidth would allow.

3.1.1 Balloon and SIP

SuperTIGER was launched on a 1.11 million m^3 long-duration balloon manufactured for CSBF by Raven Aerostar. The balloon was made of polyethylene film ∼0.002 cm (0.0008 in) thick. While partially inflated at launch, the balloon fully inflates as it ascends through the atmosphere. The 1.11 million m^3 balloon is rated for a 2721 kg (6000 lb) suspended weight. The SuperTIGER science payload weighed in at 1853 kg (4085 lbs). CSBF equipment, including the parachute, rotator, SIP, UTP (Universal Termination Package), and 220 kg (485 lbs) of ballast, brought the total suspended weight at launch to 2721 kg (6000 lbs). The 1.11 million m^3 balloon is a "zero-pressure" balloon, which means that the balloon is not sealed. One advantage of launching from Antarctica is the constant daylight and relatively small change in the sun's altitude in the sky, which minimizes the diurnal thermal variations.

Data telemetry, commanding, and monitoring of the balloon and science payload are accomplished using the CSBF Support Instrument Package (SIP). The SIP is the communication

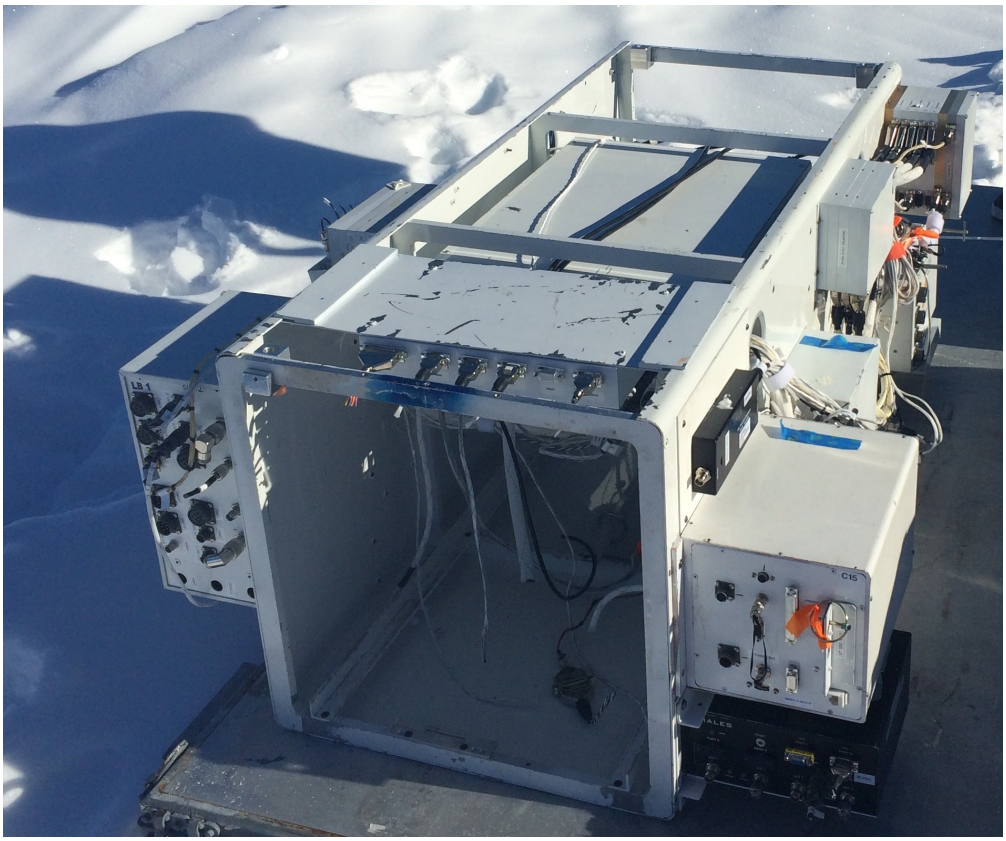

Figure 3.5: The SuperTIGER Support Instrumentation Package (SIP) after recovery.

interface between the ground, scientific instrument, and the balloon. The SIP controlled the high-gain TDRSS antenna that telemetered most of the SuperTIGER data, as well as the omindirectional TDRSS antenna and Iridium antenna that were used for supplemental data downlink. The Iridium antenna was also used for commanding. Figure 3.5 shows the SuperTIGER SIP during recovery, after having been detached from the payload.

3.2 Flight Performance

Throughout the flight, the SuperTIGER instrument demonstrated excellent performance and collected over 67×10^6 cosmic-ray nuclei. Throughout the flight, teams at NASA Goddard Space Flight Center (GSFC), Washington University in St. Louis (WUSTL),

the California Institute of Technology (Caltech), the Jet Propulsion Laboratory (JPL) and McMurdo station monitored the flight's progress. When required, changes to the high voltages, high-priority thresholds, and data rates were also commanded by these monitors. With the exception of the data rate throttle, which had to be adjusted due to changing TDRSS satellite angles and connection quality, this commanding was kept to a minimum. Data were transmitted from the payload over the TDRSS network to the TRDSS ground station at White Sands, NM, and from there sent to CSBF in Palestine, TX. Two SuperTIGER ground support computers were located at CSBF and recorded the incoming data. The two systems were redundant, which meant that there was no loss of data when one of the data recording programs froze and had to be re-started during flight.

Housekeeping data, including High Voltage (HV) monitors, temperature sensors, and data rate scalars were telemetered down every four minutes when there was a good TDRSS link. These data were used to create a monitoring webpage which included graphs of the values of each housekeeping parameter over time. This made it easy to detect suspected HV arcing, which manifested itself in the data as sudden drops in the value of a particular HV channel. These housekeeping data were used to detect the failure of the scintillator PMT that died $\sim$18 hours into flight. The webpage was updated automatically every 30 minutes. Two parallel webpages were created, one at WUSTL that was used by the monitors based in North America, and one that ran locally on a ground support computer in McMurdo. In addition, quick-look software could be run on the computers at CSBF that would scan the data for certain types of events and display them. This software was used by some monitoring shifts to confirm that commands had been received by the instrument without waiting for the webpage to update.

3.2.1 High Voltage Failures

After the thermal vacuum test at Plum Brook, each HV trim board was re-tested with pressures and temperatures expected during flight. Every board was tested for at least 12 hours and passed the pre-flight test. However, during flight, there were still several HV issues. These issues were detected using two methods: first, and most seriously by observing sudden drops in the HV values reported in the housekeeping event, and, second, by observing broad pedestal readings. Each PMT signal channel had a pedestal value that was, in principle, constant. Issues with HV arcing can broaden the distribution of pedestal readings. A series of pedestal calibrations was taken at regular intervals throughout the flight, and the distribution of pedestal readings was displayed on the monitoring webpage. In total, only 6 HV power supplies required adjusting[4] after the initial calibration of the instrument was completed.

The most serious issue encountered was with a 2000 V HV supply on the Module 2 Aerogel Cherenkov detector (M2 A600). Broad pedestals and voltage drops were first reported on December 15. Over the next several days, the HV was lowered several times but the voltage drops persisted. At 07:30 NZDT on December 24, 2012, all the voltages from this supply dropped to 0 and the PMTs stopped recording any events. The supply was quickly shut off. Because the PMTs on the long side of the Aerogel Cherenkov counter were alternated between 2000 V and 1250 V HV supplies to ensure graceful degradation, this failure did not significantly affect the data.

Three other HV supplies showed sudden voltage drops and had their voltages reduced. One of these was on the short side of the Module 2 Aerogel Cherenkov detector (M2 A200). The reduced voltage in the Cherenkov PMTs did not significantly affect the data from that

[4] A commanding error at one point set all Module 2 HV power supplies to 850 V, but this was quickly noticed and rectified.

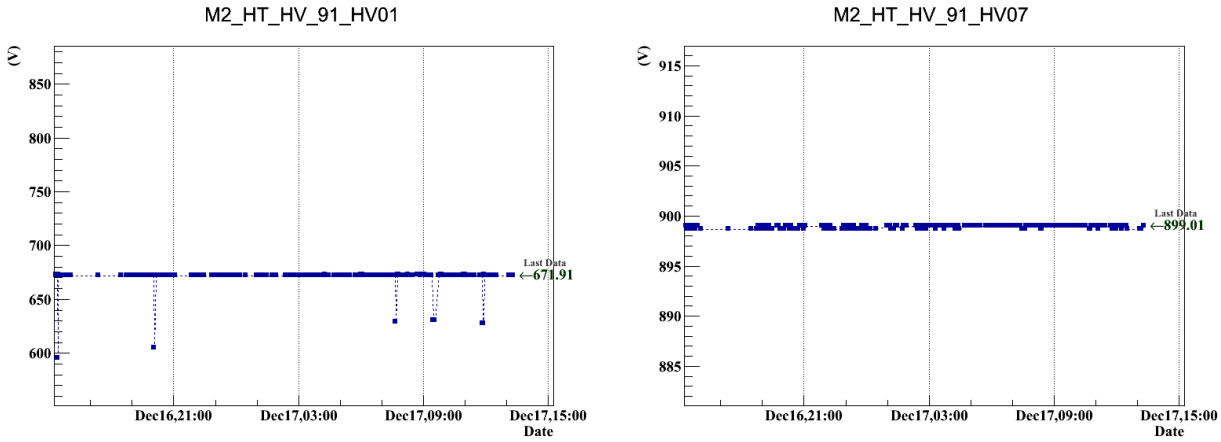

(a) A problematic HV Monitor channel.

(b) A normal HV Monitor channel.

Figure 3.6: Monitor webpage plots showing a HV channel with sudden voltage drops (a sign of arcing) and a normal HV channel over the same time period on December 16-17, 2012.

detector. The other two reduced HV power supplies were also on Module 2, one on the top hodoscope (M2 9100 HVPS1) and one on the bottom (M2 9C00 HVPS1). The reduced voltage did not significantly impact the efficiency of trajectory assignments for high-Z nuclei.

Two more HV power supplies had their voltages reduced due to broadening pedestal distributions. These were both hodoscope supplies, and their reduced voltages did not significantly affect the efficiency of trajectory assignments for high-Z nuclei. One of these supplies was on Module 1 (M1 9100 HVPS1) and one was on Module 2 (M2 9500 HVPS2).

3.2.2 TDRSS Transmission Efficiency and SSD Failure

For most of the SuperTIGER flight, the data downlink was dependent on the high-gain TDRSS antenna. Due to variations in satellite angle from the payload (which got worse at higher latitudes) and the availability of TDRSS satellites, the rate of data telemetered down varied throughout the flight. Typical transmission rates were ∼75 kbps, but maximum data rates of ∼20 kbps or ∼10 kbps were not uncommon. Based on the quality of transmission between the payload and the satellite, the rate at which data were sent down could be

throttled via a command to the flight CPU. A rate of ∼20 kbps allowed for nearly all of the high-priority data to be telemetered, while at 75 kbps nearly all of the data was transmitted. Periodically, however, no TDRSS satellite would be within range of the payload, and consequently no telemetry would get through. Overall, considering the telemetry outages, and the very low data rate periods, TDRSS data transmission was ∼ 80% efficient for high-priority events ($Z \gtrsim 22$). This gave the equivalent of ∼44 effective days of data. All triggered events were transmitted during the two LOS data periods at the beginning of the flight and at the end of the first orbit/beginning of the second orbit. In addition, prior to the data SSD failure, all events were written in full to the data SSDs on both modules.

Approximately 10.5 days into flight, the two Intel 320 series Solid State Disks (SSDs) that were used to store flight data failed. Later in the flight, the two remaining SSDs on the SuperTIGER instrument also failed. More detail on the failure of the SSDs can be found in Appendix B. The SSDs were recovered in January 2015, and data recovery from the flight disks is ongoing. The data presented and analyzed in this thesis are the data that were telemetered during flight, either via TDRSS or LOS.

3.3 Payload Recovery

The SuperTIGER payload was designed to be easily recoverable, so that the instrument could be repaired and reused on future balloon flights. Recovery of the payload therefore became a priority after the conclusion of the flight. The SuperTIGER recovery was initially planned for January or February 2013, shortly after the conclusion of the flight. Two members of the recovery team arrived in McMurdo on January 7, 2013, joining the two members of the SuperTIGER collaboration monitoring the flight there. At that point, the plan was to terminate the SuperTIGER flight when it next got close to McMurdo. However,

on January 9, 2013, we were given approval by the NASA Balloon Program Office (BPO) and the National Science Foundation (NSF) to continue the flight for a third revolution around the continent. By the time the SuperTIGER flight ended, it was too late in the 2012-2013 Austral summer season to mount a recovery effort, so the whole effort was postponed to the 2013-2014 Austral summer. The remote location of the payload after flight—82.24°S 81.91°W—complicated the matter, requiring significant aircraft resources.

3.3.1 January 2014 Recovery Attempt

A four-person recovery team, consisting of John W. Mitchell, John G. ("Grant") Mitchell, and Thomas Hams of GSFC, and JohnE Ward of WUSTL, arrived in McMurdo on January 3, 2014. They planned to fly to the SuperTIGER site via the South Pole, establish a camp, disassemble the payload, and return it to McMurdo. However, limited aircraft availability due to the 2013 US Federal Government Shutdown and warm weather in Antarctica (which led to planes being diverted from on-continent work to intercontinental flights between McMurdo and Christchurch, NZ) meant that this plan had to be scrapped. Instead, the team was offered a number of flights with a small de Havilland Canada DH-6 Twin Otter airplane (operated by Kenn Borek Air) out of Amundsen-Scott South Pole Station. The team arrived at the South Pole and waited for suitable weather. In the end, only a single flight out to the payload was possible. On January 22, 2014, a three person team (Thomas Hams of the science recovery team, Scott Battaion of the Antarctica Support Contract, and Bill McCormick, a mountaineer) flew out on a Twin Otter from the South Pole to the SuperTIGER site. After a stop at a fuel cache to refuel, they arrived at the payload at around 1330 local time. At that point, the Twin Otter had ∼15 minutes of fuel to find a spot to land or the pilot would have to return to the South Pole. Due to large

Figure 3.7: The SuperTIGER payload upside down and buried in snow on January 22, 2014. Photo by Thomas Hams.

irregular sastrugi, the plane was unable to land, but did make several low-altitude passes over the payload so that reconnaissance photographs could be taken.

The most surprising result of this reconnaissance flight was the discovery that the entire payload was upside down. Figure 3.7 shows the payload as seen during the January 2014 overflight. The instrument is nearly entirely buried in the snow, with only the lower parts of the gondola and ballast hopper visible. The ballast hopper and central C-channel of the gondola appear damaged, suggesting that the payload landed right side up and was then somehow tipped over.

3.3.2 2014-2015 Recovery

After the unsuccessful January 2014 recovery attempt, a new attempt was planned for the 2014-2015 Austral summer season. Conditions observed during the January 2014 overflight suggested that large sastrugi would make landing near the payload impractical. Therefore, the plan was for a four-person groom team to fly out to the SuperTIGER site via the West Antarctic Ice Sheet (WAIS) Divide field camp, land as close to the payload as possible, and establish a camp. From there, this team would, using ground-penetrating radar to avoid crevasses, traverse over to the SuperTIGER payload and re-establish a camp. The groom team would then groom a skiway near the payload, flattening out the surrounding sastrugi and snow to create a suitable strip for planes to land on. A four-person science recovery team would then fly in via WAIS Divide, camp for $\sim$10 days, disassemble the instrument, and return to McMurdo in time to pack the instrument up for shipment back to the United States by sea.

Most of the four-person science recovery team—Thomas Hams and Sean Fitzsimmons of GSFC, as well as myself—arrived in McMurdo on December 3 (the fourth member, Dana Braun of WUSTL, was already in McMurdo working on preparing the ANITA balloon-borne experiment for launch). While en route from the United States, we got word that a Kenn Borek air Twin Otter operating out of the NGO camp at Union Glacier had done a reconnaissance overflight of the SuperTIGER payload, and reported that the sastrugi conditions had improved considerably. A Twin Otter could thus land close enough to the SuperTIGER payload to establish a camp there directly. The recovery plan quickly changed in other ways as well, as poor weather conditions at WAIS Divide led to a local fuel shortage and the diversion of our recovery efforts elsewhere.

On December 24, 2014, the four person "Super Groom Team" left McMurdo on a New York Air National Guard LC-130 Hercules and landed at Thomas Hills (84°27S 65°

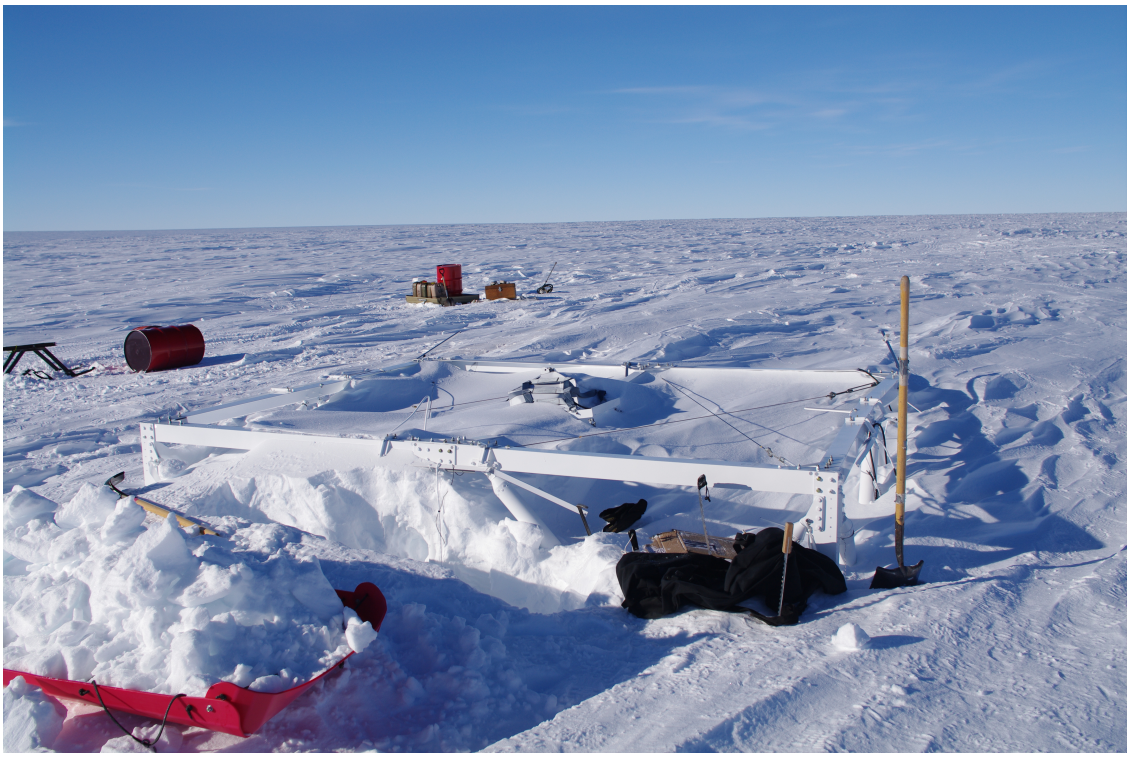

Figure 3.8: The SuperTIGER payload after the arrival of the Super Groom Team. Photo by Dave White.

36 W), a field camp ∼180 nautical miles from SuperTIGER recently established for a geology group. The Super Groom Team consisted of Thomas Hams of GSFC, the science representative, James King, the camp supervisor, Lyra Pierotti, a mountaineer, and Dave White, a snowmobile mechanic. On December 29, three Twin Otter flights shuttled the Super Groom Team from Thomas Hills to the SuperTIGER site. The team got to work grooming a skiway and excavating the payload, which was nearly entirely buried. After digging out a large pit surrounding the payload, Thomas began disassembling the gondola and the detector stacks.

Meanwhile, the rest of the recovery team (the "Tiger Tail" team, consisting of Sean Fitzsimmons of GSFC as well as Dana Braun and myself from WUSTL) prepared to join the team in the field shortly via the South Pole station. The Tiger Tail team arrived at the South Pole on January 5, 2015. On January 8, a Twin Otter flight from the South Pole

Figure 3.9: The field camp established at the SuperTIGER recovery site.

brought the Super Groom Team a new snowmobile, and returned with the CSBF SIP, as well as Dave White, who had injured his leg. The Tiger Tail team planned to fly to the SuperTIGER site on a Kenn Borek Air Basler BT-67, a modified Douglas DC-3 airframe with an extended fuselage and turboprop engines. Mechanical failures and poor weather conditions delayed the Basler's arrival at the South Pole until January 15. Flights out to the SuperTIGER site required good weather conditions at the South Pole and near-perfect conditions at the site, so no flights were possible until January 24. On January 24, 2015, Sean Fitzsimmons and I, along with the four person Basler crew, flew out to the SuperTIGER site. By the time we arrived, Thomas had disassembled the entire gondola, and removed all the S2, S3, and bottom hodoscope detectors from both modules. The remaining detectors were stacked on top of each other with only insulation foam between them, so the recovery was a matter of removing the detectors from the pit that Thomas had dug and loading them on the airplane. In $\sim$4.5 hours on the ground, we were able to load all of the detectors and most of the gondola onto the Basler. Thomas, Sean, and I flew back with the equipment

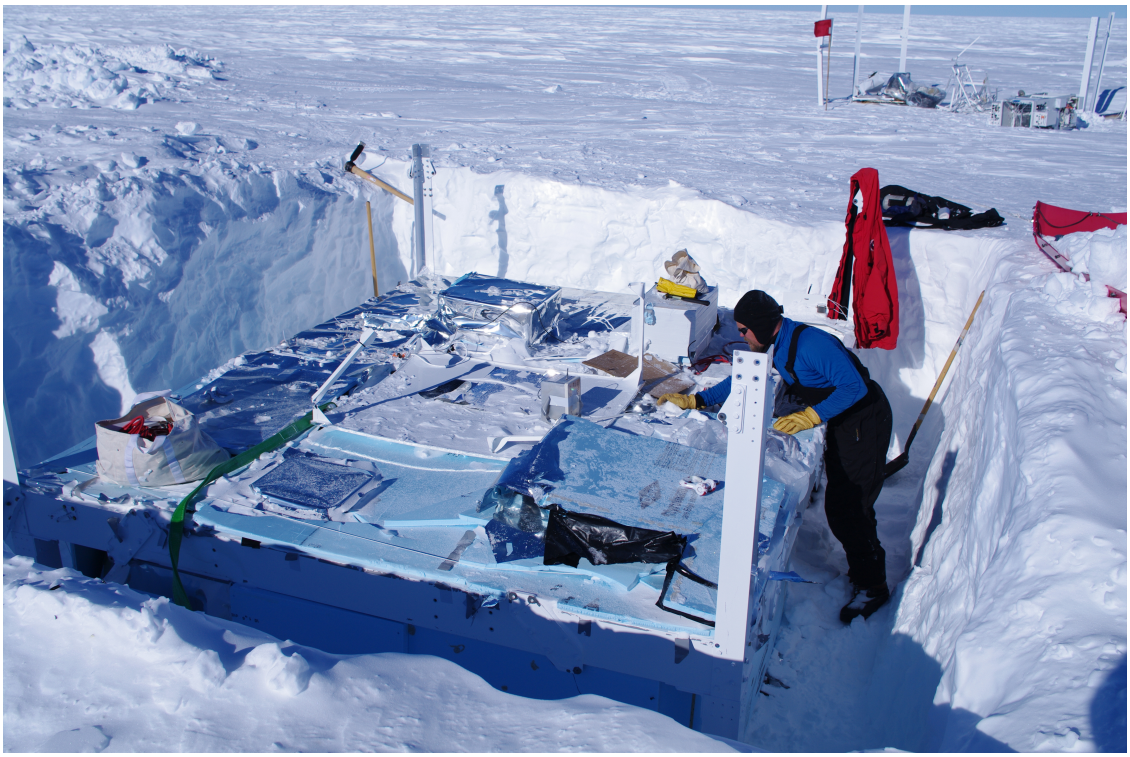

Figure 3.10: The SuperTIGER payload in the pit at the recovery site. Photo by Dave White.

to the South Pole. The Basler crew returned to the site the next day to get the rest of the science equipment, most of the camp equipment, and James and Lyra. A third flight a few days later removed the rest of the camp equipment and trash. Overall, most of the detectors appeared to be in good condition. When the payload flipped over and landed upside down, one module landed directly on top of the CSBF rotator, which damaged the two S1 scintillator detectors and bent the substrate of the top hodoscope of that module. The two scintillator detectors were noticeably deformed and their radiators cracked. One hodoscope fiber was accidentally cut during the recovery process, and several aluminum lids to scintillator detectors were damaged. Post-flight testing is ongoing.

Once back at the South Pole, we prepared the various detectors for shipment back to McMurdo. In total, the SuperTIGER detectors and recovery tools took up one standard-size Air Force 436L master pallet of tools, electronics boxes, and other gear, one double-size "T2" pallet with the Cherenkov detectors, scintillator detectors, and honeycomb pallets,

Figure 3.11: Moving the hodoscopes to the recovery plane.

and an "overflow" standard pallet with the hodoscopes. These pallets filled the cargo hold of a LC-130 Hercules flight from the South Pole to McMurdo on January 28, 2015. Once in McMurdo, the detectors[5] were re-stacked in a single stackup and secured in a shipping container. A second shipping container contained the electronics boxes, cables, and other recovery tools. These containers were picked up for shipping on January 30, ∼1 hour before the shipping deadline for the 2015 cargo vessel. The gondola parts arrived in McMurdo in early February 2015, and will be shipped back on the 2016 cargo vessel. The SuperTIGER detectors arrived in the United States in April 2015, and post-recovery testing is ongoing.

[5]With the exception of the two damaged scintillator detectors

Chapter 4

Charge Assignment

Two complementary techniques were used to assign a charge Z to SuperTIGER data events. At low energies (above the C1 threshold of ∼300 MeV/nucleon but below the C0 threshold of 2.5 GeV/nucleon or 3.3 GeV/nucleon, depending on the half-module the event went through), the charge was determined using a combination of signals from the top two layers of scintillator detectors (S1 and S2) and the Acrylic (C1) Cherenkov detector. At energies above the C0 threshold, the charge was determined with a combination of the C1 and Aerogel (C0) Cherenkov detector. Cosmic-ray events were sorted into two datasets, the Above and Below C0 datasets. These techniques were applied after the mapping and other corrections discussed in Section 4.1 and the interaction cuts discussed in Section 4.2. These complimentary techniques allowed us to identify charge over a broad energy range. The data were analyzed using the ROOT data analysis library for C++ and by a custom ROOT library called stlib that was developed by Makoto Sasaki of NASA Goddard Space Flight Center (GSFC), based on the code library from the BESS (the Ballon-Borne Experiment with a Superconducting Spectrometer) data analysis. I used two major types of computer programs to analyze the data. Selector programs, which ran on the so-called "DST" files each containing all the cosmic-ray events from one day of flight, analyzed each event to see if it met selection criteria, and then processed the selected data as instructed, often by creating and filling histograms with detector signals or calculated charge values. Selector programs

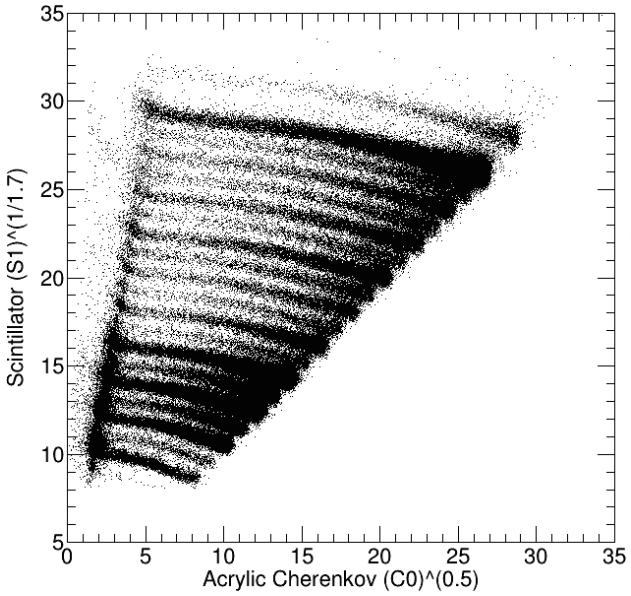

Figure 4.1: Cross-plot comparing Scintillator and Acrylic Cherenkov signals used in low-energy (Below C0) analysis.

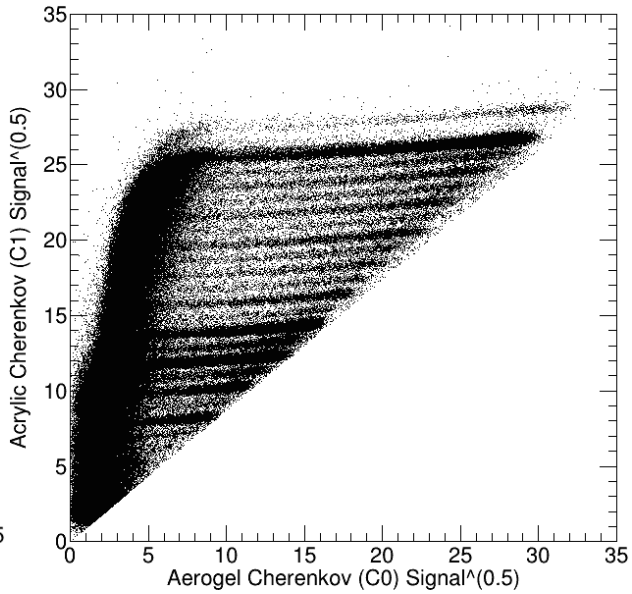

Figure 4.2: Cross-plot comparing Aerogel and Acrylic Cherenkov signals used in high-energy (Above C0) analysis.

created .root files that were analyzed by secondary programs. These secondary programs took the objects in the .root files and analyzed them–e.g. by fitting a gaussian function to a histogram filled by a selector file. In general, when future sections talk about filling a histogram, that was done by a selector file, while fitting a histogram with some function is done by a secondary program.

This chapter covers the pre-processing and calibration of the data before analysis, the cuts we used to identify and reject events that underwent nuclear interactions in the instrument, and the two methods of charge identification. The results of these analysis methods–the numbers of events observed within the instrument–are found in Section 4.6.3.

4.1 Data Pre-Processing and Calibration

The SuperTIGER data were telemetered in an ASCII text-based format. The data telemetered down via the LOS antennae were in an uncompressed format, while the data telemetered via TDRSS were compressed as described in Section 2.5. After the flight, Makoto Sasaki of GSFC converted these data files to useable Data Storage and Transfer (DST) files. Appendix C describes the processing that went into these files, which included calibration, gain-mapping, and an iterative area mapping correction. A trajectory was also calculated and assigned when possible.

One DST file included 24 hours of flight data (from 00:00:00 NZDT to 23:59:59 NZDT on a given day). For each event, the file listed an event number, an event time, and then two sets of information about the event, a "header" including information about the general state of the instrument, and a "dst" set including information about the event itself. The "header" for each event in the DST file contains information about the state of the instrument when that event was recorded, including the latitude, longitude and altitude from the SIP, the pressure from 3 different SIP barometers, whether the event was classified as high-priority or low-priority, and whether the event came over the LOS or TDRSS downlink. The "dst" set of parameters for each event in the DST file includes 32 different pieces of information about each event, including which module it occurred in, how many hodoscope fibers it gave a good signal in, the (x, y) positions in the top and bottom hodoscopes, the incidence angle, the total signal observed in each detector, and a rough estimate of the charge from each detector. For the data analysis, this total signal observed in each detector is what we refer to as the signal, e.g. "S1 signal" is the total signal from the S1 scintillator detector.

These DST files were what I used to analyze the data for the rest of the chapter and the primary analysis. An expanded "raw" set of DST files was also generated, which included information on each PMT for every event. These raw files were used when doing analysis

on a single-PMT level, such as finding the Hodoscope Attenuation Length in Appendix A, but proved unwieldy and unnecessary for the primary data analysis. Appendix C gives the details about the corrections and processing that created these files.

4.2 Interaction Cuts

As cosmic-ray particles traverse SuperTIGER instrument, some fraction will undergo nuclear interactions within the instrument, causing a change in the charge Z. Interaction cuts are therefore required to ensure that the particles being included in the data analysis are those which have not changed charge within the active area of the instrument. However, high-Z particles are significantly more likely to interact within the instrument, so these interaction cuts cannot be too restrictive. For the SuperTIGER analysis, we primarily used two different interaction cut regimes: a loose cut, which increased the number of UH particles observed but had poorer resolution, and a restrictive cut, which was used to develop and test the charge assignment methods described below. Before interaction cuts were applied, all events that did not have a well-defined path (calculated using the top and bottom hodoscope) were excluded. We were able to assign a well-defined path to ∼82% of all cosmic-ray events we recorded. We also exclude all events that do not have a signal from every functional tube in each scintillator detector the particle passed through.

Restrictive Regime

The restrictive regime defined a number of cuts requiring agreement between various detectors. First, a S1 vs C1[6] cut, shown in Figure 4.3 cut away events that have spuriously

[6]Unless otherwise specified, these interaction cuts were made using cross-plots of detector signal in roughly charge units, so the S1 vs C1 cut was actually done on an $S1^{(1/1.7)}$ vs $C1^{(1/2)}$ cross-plot. To get to rough charge units, we took the 1.7th root of the Scintillator signals and the square root of the Cherenkov signals.

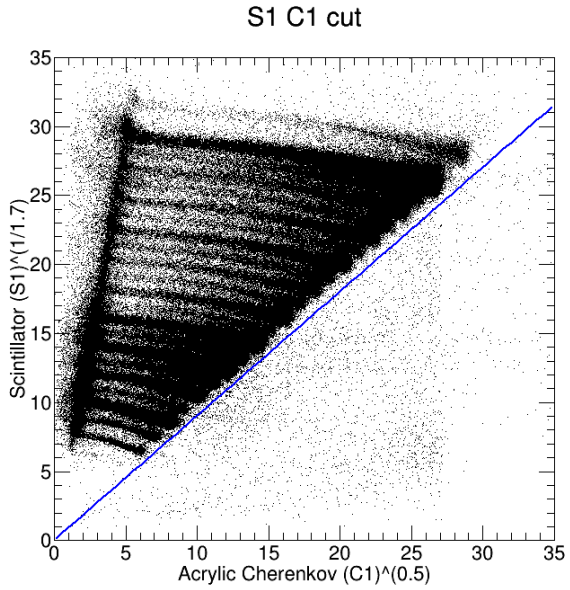

Figure 4.3: S1 vs C1 interaction cut used in SuperTIGER data analysis. We accepted events to the left of the line shown. Similar cuts were defined using S2 and S3 vs C1 cross-plots.

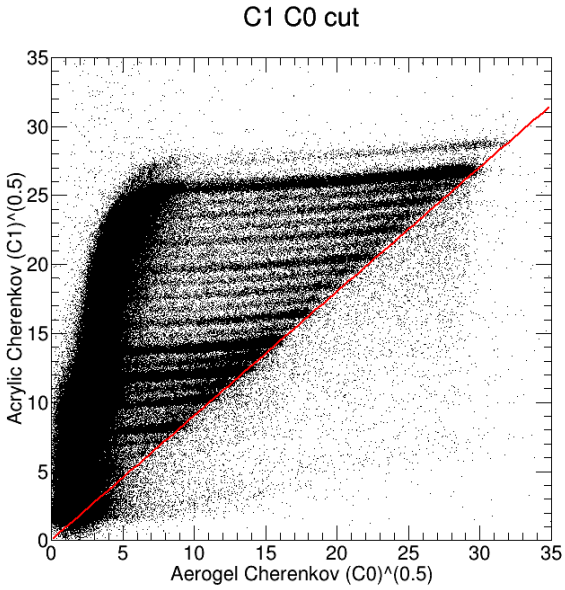

Figure 4.4: C1 vs C0 interaction cut used for Above C0 data set. We accepted events to the left of the line shown.

low S1 signals (or spuriously high C1 signals). This cut eliminated ∼1% of those particles we were able to reconstruct a good trajectory for.

A similar cut was performed for S2 vs C1 and S3 vs C1. Figure 4.4 shows the cut made on the C1 vs C0 cross plot to throw away events with spuriously high C0 and/or spuriously low C1 signals. This cut eliminated ∼4% of events with good trajectories. These events with abnormal signals are not analyzable using the techniques described below. The restrictive regime also required agreement between S1 and S2, as shown in Figure 4.5. Those events in Figure 4.5 below the lower line are interacted events, as they have a lower signal in S2 than in S1. The events above the top line are low-energy events that have slowed down within the SuperTIGER instrument, and therefore give a higher signal in S2 than S1. These low-energy events were left out of the restrictive regime to improve charge resolution. Similar cuts were applied using the S3 vs S1 and S3 vs S2 cross-plots. In the restrictive regime, this S2/S1

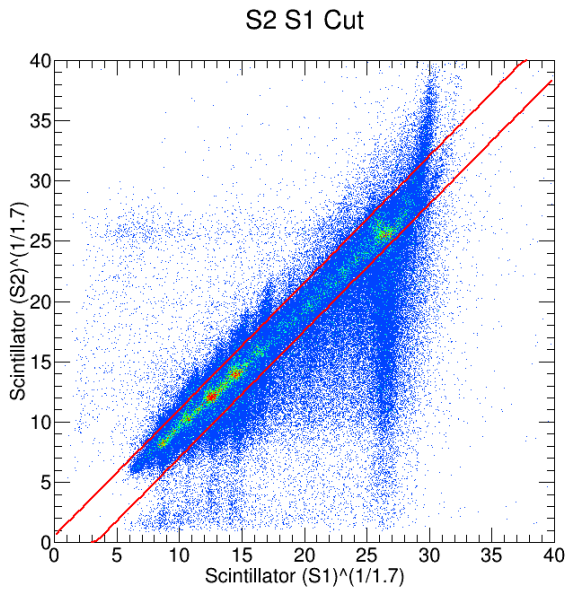

Figure 4.5: S2 vs S1 interaction cut used for Below C0 data analysis. We accepted events in between the two lines for the restrictive regime, and above the lower line for the looser regime. Similar cuts were defined using the S3 vs S1 and S3 vs S2 cross-plots.

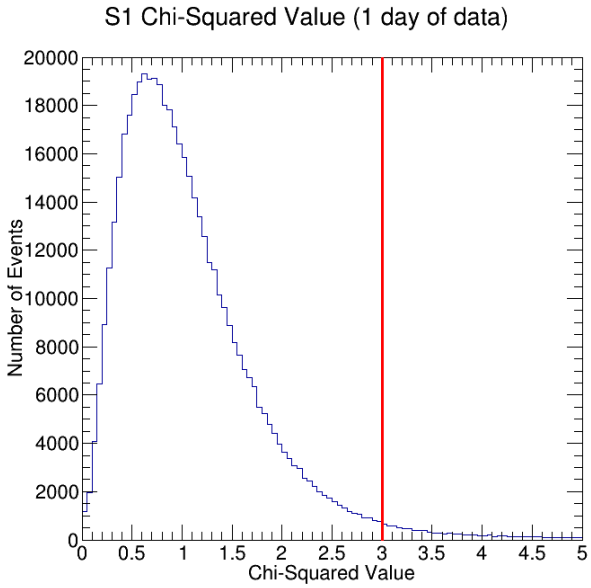

Figure 4.6: χ^2 cut for S1. We accepted all events to the left of the line shown. Similar cuts were defined for S2 and S3 χ^2 values.

cut eliminated ∼19% of particles with a good trajectory, while in the loose regime (where the low-energy particles are included) only ∼10% of particles with a good trajectory were eliminated.

A further cut is applied at the same time as the interaction cuts. Using the signals from individual tubes within one scintillator detector, we calculated a χ^2 value based on the variance of the (corrected) PMT signals within a detector. We then cut away those events with particularly high χ^2 values in one or more scintillator detectors. Only the actual scintillator detector on each layer that the particle passed through is considered for the χ^2 cut. The χ^2 cut eliminated ∼0.1% of events with a good trajectory.

Between all of the cuts in the restrictive regime, ∼40% of events with good trajectories were eliminated.

Loose Regime

The loose regime, which was used for the data analysis of the UH dataset, includes a subset of the cuts defined for the restrictive regime. For the Above C0 data, I used only the S1 vs C1 cut, the C1 vs C0 cut, and the S1 χ^2 cut. For the Below C0 data, I used the S1 vs C1 cut, the S2 vs C1 cut, the χ^2 cut for S1 and S2, and the bottom line of the S2 vs S1 cut (see Figure 4.5). This loose interaction cut increased the number of events accepted, which was necessary for the UH dataset, but gave slightly worse resolution (0.17 cu at $_{26}$Fe, compared to 0.16 cu with the restrictive cuts). In total, ∼12% of events with good trajectories were eliminated in the loose regime.

4.3 Above C0 Method

The Above C0 method compares signals from the Acrylic (C1) and Aerogel (C0) Cherenkov counters. Figure 4.7 shows an example cross-plot with one day of data. The method I used was first developed by Makoto Sasaki, a SuperTIGER collaborator from NASA's Goddard Space Flight Center. First, an Above C0 threshold cut was applied. This cut eliminated all particles to the left of the line shown in Figure 4.7. The equation of this line was found by looking at the C0 signal distributions for each even Z in the range$14 \leq Z \leq 28$ and finding the Cherenkov turn-on signal (see Figure 5.1 in the next chapter).

The charge bands on this cross-plot follow straight lines, which becomes apparent when re-examining Equation 2.4. This equation gives the total light output of a Cherenkov

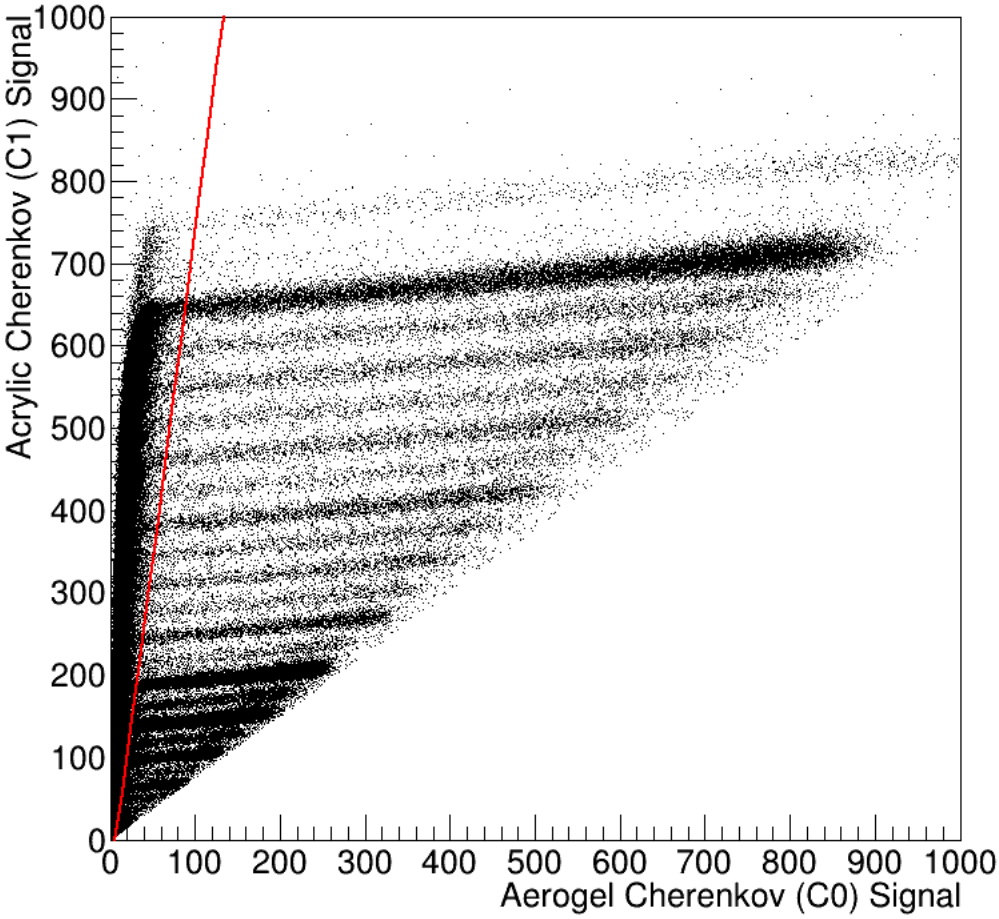

Figure 4.7: C1 vs C0 cross plot used in the Above C0 data analysis. Red line shows the C0 threshold cut used for $n = 1.04$.

detector:

$$L_{Ch} = KZ^2 \left(1 - \frac{1}{\beta^2 n^2}\right). \tag{2.4}$$

Again, K is a detector-specific constant, so the signal from a Cherenkov detector depends on the charge Z squared, and a simple function of the index of refraction n of the counter and the relativistic velocity β, which goes to 0 at the Cherenkov threshold, where $\beta = 1/n$. The cosmic-ray events analyzed using the Above C0 method obviously have energies above the C0 threshold of 2.5 GeV/nucleon or 3.3 GeV/nucleon (depending on which half-module the particle passed through). At these energies, the energy loss between the two Cherenkov

counters (which are placed on top of each other in the detector stack) is very small, so β is essentially the same in each detector. If the particle does not interact between the C0 and C1 detector (and these events are excluded by our interaction cuts, so this applies to all the events analyzed with this method), the charge Z is also the same in the two detectors. Since we know the n for each of our Cherenkov radiators, that leaves us with two versions of Equation 2.4 with two unknowns, Z and β:

$$L_{C0} = K_{C0} Z^2 \left(1 - \frac{1}{\beta^2 n_{C0}^2}\right). \tag{4.1}$$

$$L_{C1} = K_{C1} Z^2 \left(1 - \frac{1}{\beta^2 n_{C1}^2}\right). \tag{4.2}$$

Combining these two, we can solve for the C0 signal as a function of the C1 signal:

$$L_{C1} = Z^2 K_{C1} \left(\frac{{n_{C1}}^2 - n_{C0}^2}{n_{C1}^2}\right) + \frac{n_{C0}^2}{n_{C1}^2}\frac{K_{C1}}{K_{C0}} L_{C0}. \tag{4.3}$$

This equation shows that the C1 signal can be expressed as a linear function of the C0 signal. The Z^2 factor on the intercept term means that charge bands of different Z will offset from each other, and the lack of a Z-dependent factor in the slope means that the lines will be parallel. The Z dependence of the Cherenkov signal also therefore depends on just Z^2, without the saturation term required in the Below C0 method described in the next section[7]. Before analyzing the data, I also cut away all the events below the C0 threshold, using the cut shown in figure 4.7.

To assign charge to the Above C0 data set we treated particles that went through the $n = 1.04$ and $n = 1.025$ aerogels separately, but with the same method. First, we divided the data into 30 bins based on incidence angle, each containing roughly (within $\sim$1%) equal numbers of Iron events. The data we analyzed in this way had already had mapping and

[7] I did apply the Below C0 method to the Above C0 data, and the coefficient for the deviation from Z^2 in the Voltz Model was negligible.

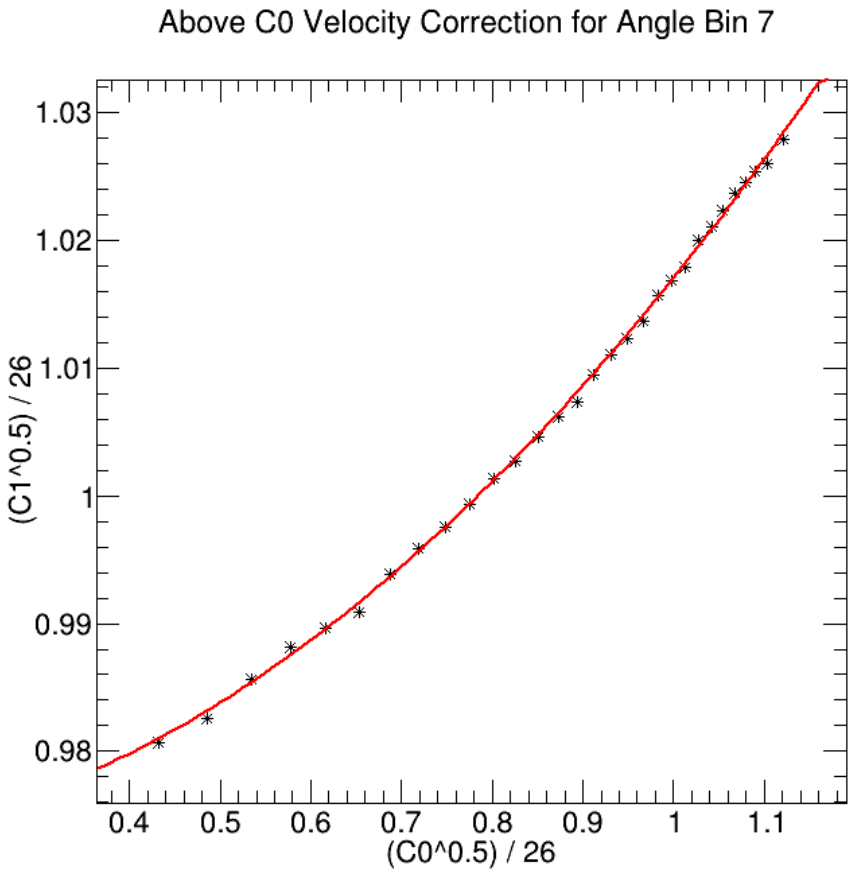

Figure 4.8: Velocity Correction graph for a typical angle bin.

a basic path-length correction applied, but a further angle correction was necessary. We then isolated the Iron ($Z = 26$) charge band on the cross-plot above, and broke it into 30 more bins with different C1 values with roughly (again within ~1%) equal numbers of Iron events. Within each bin, we filled a histogram with the ratio of the square root of the C1 signal values to 26 ($C1^{0.5}/26$). This factors out the Z^2 dependence. We then fit a gaussian function to each of these histograms to find the peak $C1^{0.5}/26$ value in each bin. A similar histogram of the ratio of the square root of the C0 signal values and 26 ($C0^{0.5}/26$) was also filled, and used to find the mean $C0^{0.5}/26$ value for each bin[8]. We then plotted a point for

[8]Fitting a gaussian function made sense for the C1 values, as we expect a nearly-gaussian charge distribution around $Z = 26$. The C0 values provide a measure of the particle's energy, and we would not expect a gaussian distribution in energy, so the mean value is used

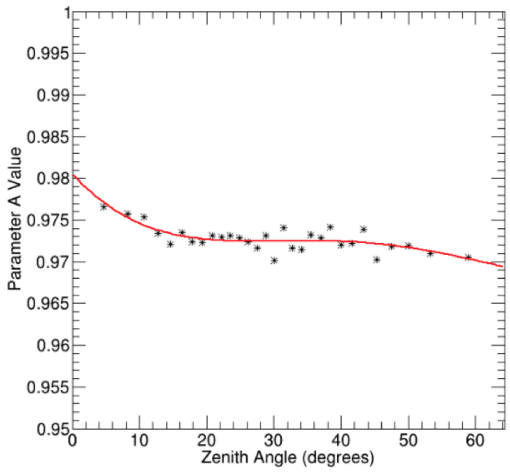

(a) Velocity Correction A vs angle

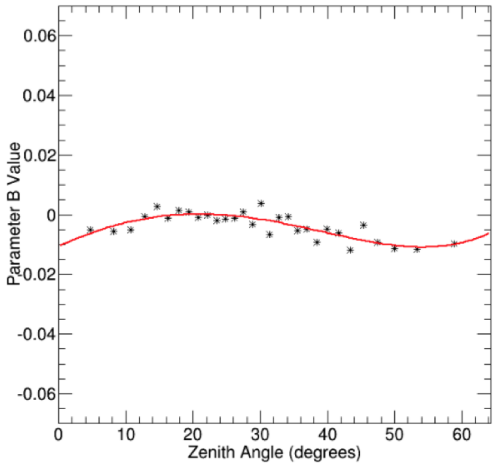

(b) Velocity Correction B vs angle

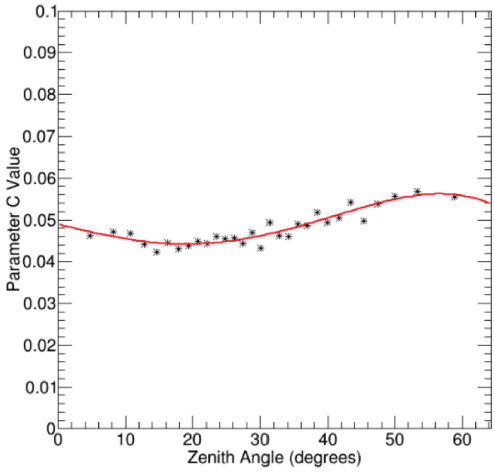

(c) Velocity Correction C vs angle

Figure 4.9: Plots showing the angle-dependence of parameters A, B, and C defined in Equation 4.4 and used in Equation 4.5.

each bin as shown in Figure 4.8, and fit this graph with a 2nd-order polynomial function ($y = A + Bx + Cx^2$).

With a value for each of the three parameters of this 2nd-order polynomial function in each of 30 angle bins, we then found the angle dependence of each parameter, as shown in Figure 4.9. This was done by plotting the parameter value against the mean angle value for that angle bin, and fitting a 4th-order polynomial function. This allowed us to assign a

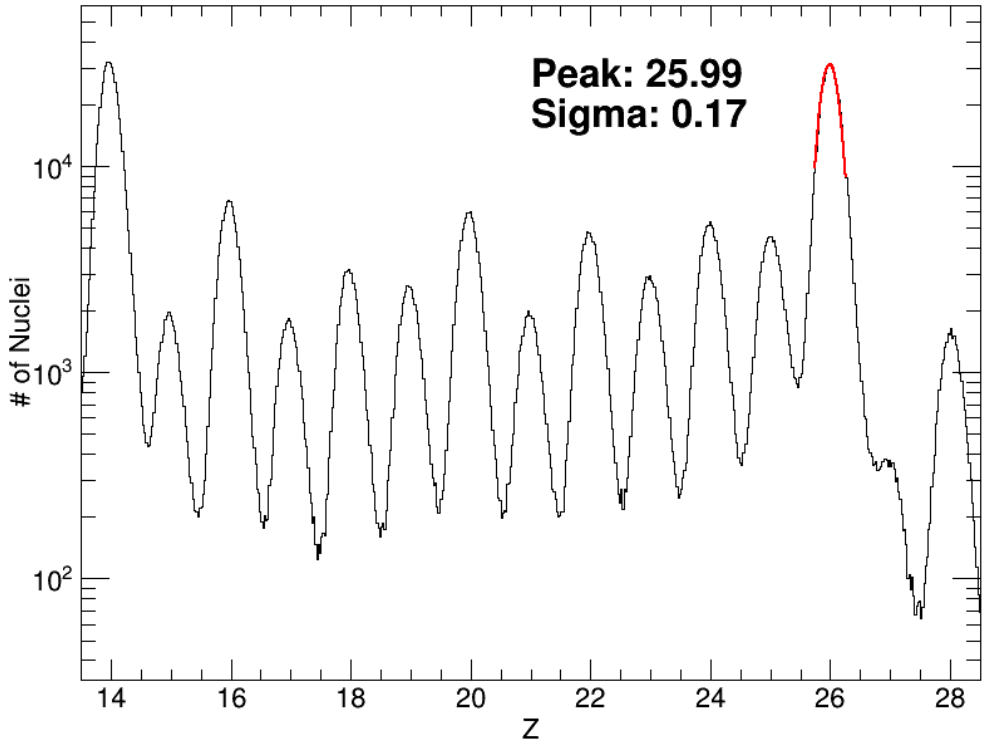

Figure 4.10: Charge histogram of Above C0 data after the velocity correction is applied.

value to A, B, and C for an arbitrary angle, and solve for our initial Above C0 Z_0 using the quadratic formula as follows:

$$y = A + Bx + Cx^2 : \qquad y = \frac{C1^{0.5}}{Z_0}, \qquad x = \frac{C0^{0.5}}{Z_0}. \tag{4.4}$$

Let

$$\alpha = A, \qquad \beta = B * C0^{0.5} - C0^{0.5}, \qquad \gamma = C * C0, \tag{4.5}$$

$$Z_0 = \frac{-\beta + \sqrt{\beta^2 - 4\alpha\gamma}}{2\alpha} \quad . \tag{4.6}$$

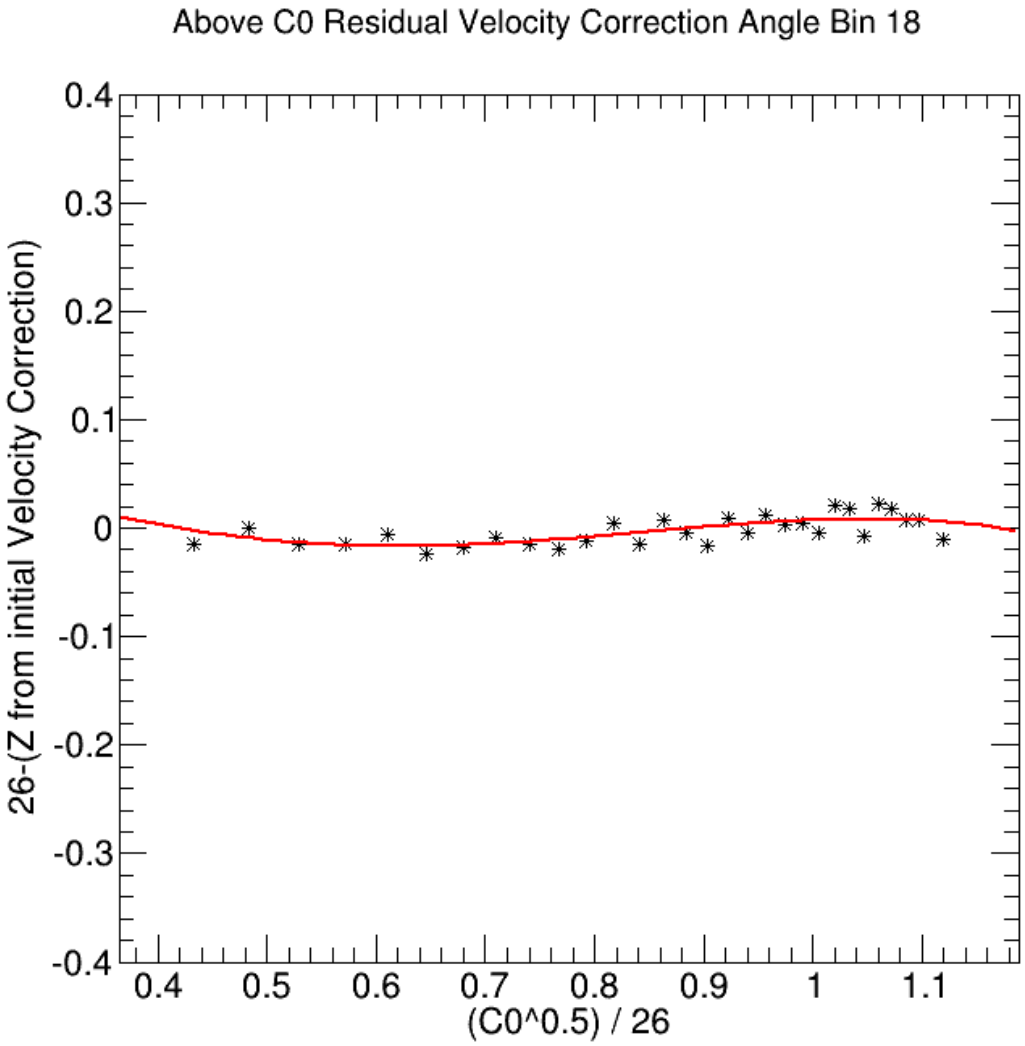

Figure 4.11: Residual Velocity Correction plot for a typical angle bin.

Figure 4.10 shows a histogram of the charges assigned using this method. It has a charge resolution at Iron similar to that obtained on the TIGER experiment, but better resolution can be obtained by making an additional energy correction. To make this correction, we first isolated the Iron events by choosing all events whose charge calculated so far fell in the range $25.5 \leq Z_0 \leq 26.5$. We again broke these events up into 30 bins each containing a roughly equal number of Iron based on the incidence angle, and then within each angle bin made 30 more bins based on C0 signal. Within each bin, we again filled a histogram with the $C0^{0.5}/26$ values, and took the mean value. We also filled a histogram with the values

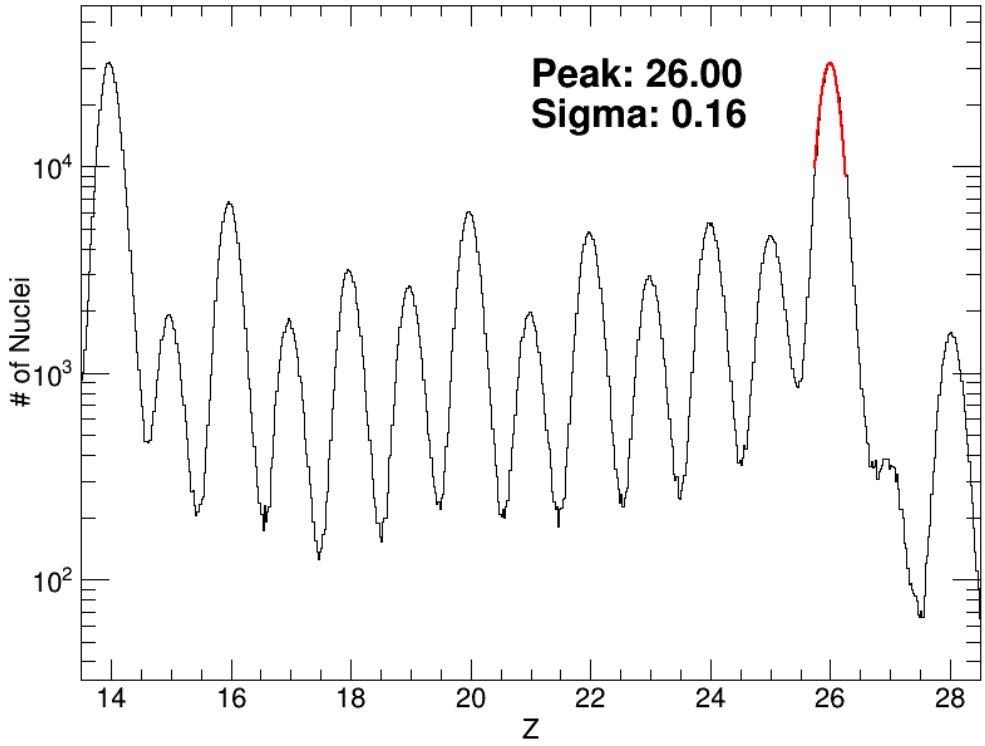

Figure 4.12: Charge histogram of Above C0 data after the residual velocity correction is applied.

of $26 - Z_0$, and fit a gaussian function to find the peak in each bin. We then plotted this peak against the mean $C0^{0.5}/26$ value for each bin, as seen in Figure 4.11, and fit this with a 4th-order polynomial function. We then assigned a charge $Z_1 = Z_0 - \Delta Z$ to each event, where ΔZ is the value of the appropriate (for the relevant incidence angle bin) 4th-order polynomial at $C0^{0.5}/26$. Figure 4.12 shows the charge histogram obtained with this method.

4.3.1 Re-normalization

The peaks of the charge histogram we obtain are well-defined and well-separated, but do not always fall on integer Z values. In order to effectively combine the Above C0 and Below C0 datasets, we re-normalized this data set by fitting a 4th-order polynomial to each

even peak from $12 \leq Z \leq 38$, and using this function to slightly shift the charge of each event so that the peaks line up with integer values. This resulted in well defined, well separated peaks within 0.01 charge units of their corresponding integer Z value.

4.4 Below C0 Method

Assigning charge to the Below C0 data set depends on finding a reasonably accurate description of the response of the scintillator light output to higher charges, as discussed in Section 4.4.2. While the signal from the Cherenkov detectors described in Section 4.3 depends on the charge of the particle squared, the scintillator signal gives a measurement of the amount of light emitted by the radiator as a function of the path length traversed by the ionizing particle, $\frac{dL}{dX}$. This light is emitted by a scintillating dye, which saturates at high energy densities. Thus, while the energy loss $\frac{dE}{dX}$ within the scintillator detector will be proportional to the charge Z squared, not all of this energy will be converted into scintillation light. To assign charge to high Z particles, we therefore need a model of scintillator response that takes these non-detectable energy losses into account.

The basic approach used to assign charge using the Below C0 method is similar to that used on TIGER data by Link (2003) and Rauch (2008). For each of 30 angle bins, I first found curves of constant charge on a S vs C1 cross plot, and then found the intersection of these curves with curves of constant energy. Then, 50 such curves of constant energy were fit with energy-independent models of scintillator response, and the energy-dependence of each model parameter was derived for the SuperTIGER scintillator detectors. To add in an additional angle correction, I then interpolated between angle bins to find a unique set of model parameters for an arbitrary energy and incidence angle.

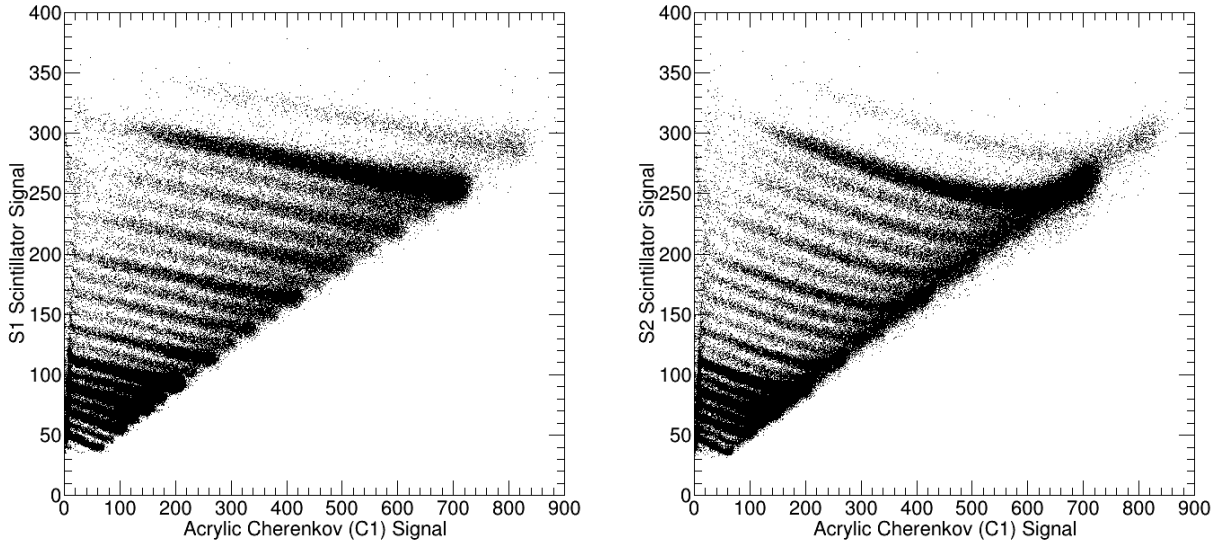

(a) S1 vs C1 cross-plot.

(b) S2 vs C1 cross-plot.

Figure 4.13: Cross-plots showing one day of data showing well-defined, separated charge contours. These cross-plots were used to assign charge for the Below C0 dataset.

Figure 4.13 shows cross-plots with one day of data for both S1 and S2 signal vs C1 signal. To find curves of constant charge, I manually drew lines in between each charge band, creating rough boundaries for each charge band, as shown in Figure 4.14. Since this charge assignment technique was only to be used for those events for which a good charge contour and scintillator response model could be fit, the events with saturated signals at high C1 signal values were cut away. A similar cut was made to eliminate the small number of low-energy particles to ensure that each charge contour was entirely within the hand-drawn boundary lines. Figure 4.15 shows the low-energy and Below C0 cutoff cuts that were made.

The Below C0 cutoff cut was applied to eliminate those events with overly saturated scintillator detector signals, for which we were unable to fit a good curve of constant charge. This cut corresponded to an energy value lower than the Acrylic Cherenkov (C0) threshold (see Section 5.2.1), so a portion of the total data collected by SuperTIGER ($\sim$10%) was not included in this analysis. A preliminary analysis using the Below C0 method showed that

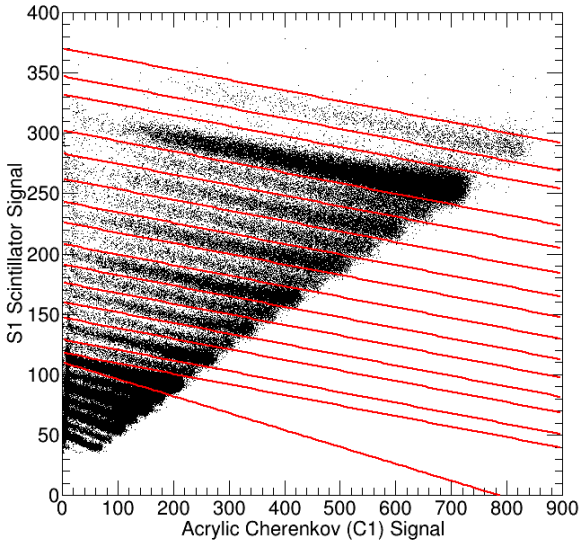

Figure 4.14: Hand-drawn lines between each charge contour for S1.

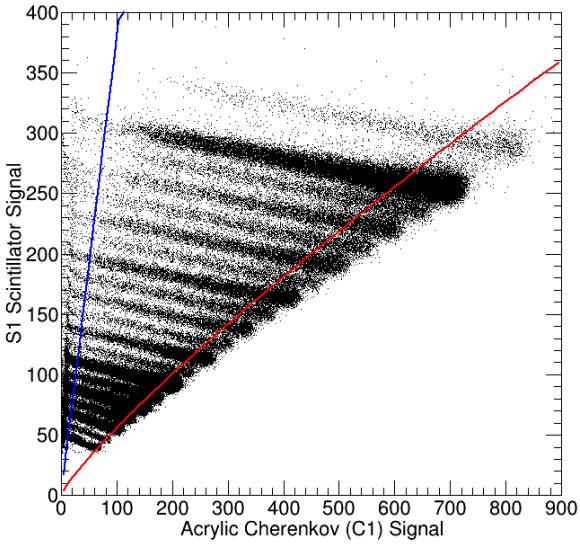

Figure 4.15: Low-energy (blue) and Below C cutoff (red) cuts on the S1 vs C1 cross-plot.

excluding these events did not introduce any bias into the derived abundances of ultra-heavy nuclei. A more detailed analysis of these data is planned before the SuperTIGER results are submitted for peer-reviewed publication. The data were then divided into 30 angle bins, each containing a roughly equal number of events in the Iron band. The rough boundary lines between charge bands proved to be acceptable regardless of the angle bin. These charge boundaries were defined for every element from Silicon ($Z = 14$) to Nickel ($Z = 28$).

Within each of the 30 angle bins, each charge band was then divided into 50 vertical bins based on the C1 signal, each containing roughly 2% of the events in that band. Events falling within each bin were placed into histograms based on the signal from the scintillator. Each of these histograms was fit with a gaussian function to find a typical value of the S signal. Figure 4.16 shows a typical histogram and gaussian fit. The peak of the gaussian (as the y-value), along with the mean C1 value (as the x-value), in each bin was used to plot a point on the S vs C1 cross-plot. The 50 points for each charge band were then fit by a 2nd-order polynomial function to give a curve of constant charge. Figure 4.17 shows the

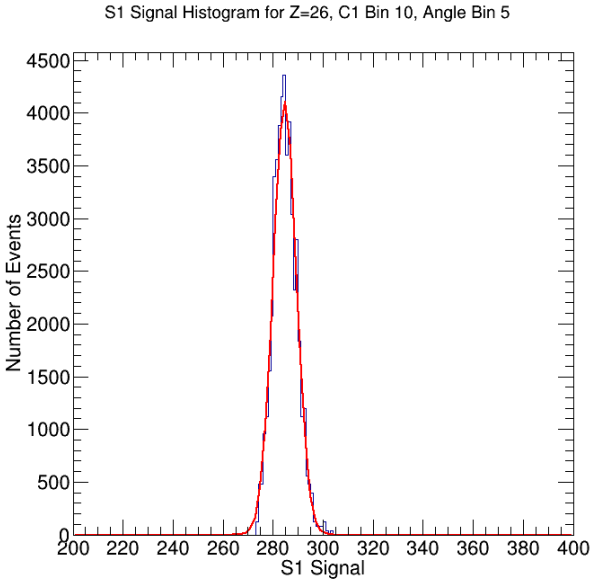

Figure 4.16: A typical histogram for a single Iron ($Z = 26$) bin.

curves of constant charge derived using this method for a typical angle bin in red. For the final analysis, the Cobalt ($Z = 27$) line was not used due to low statistics.

Next, I found curves of roughly constant energy. From Equation 2.4, we have an expression for the light output of our Cherenkov counters:

$$L_{Ch} = KZ^2 \left(1 - \frac{1}{\beta^2 n^2}\right). \tag{2.4}$$

Here, K is a constant that can be determined for each detector, and the index of refraction n is assumed to be a constant within our detector. The C1 signal thus changes based on the charge Z squared and the relativistic velocity β. I therefore used C1/Z^2 as a proxy for the energy of a particle passing through the detector, since events with the same C1/Z^2 value will have the same β value:

$$\frac{C1}{Z^2} = K \left(1 - \frac{1}{\beta^2} n^2\right). \tag{4.7}$$

To determine the Z value, I started with the approximation that the scintillator signal S is

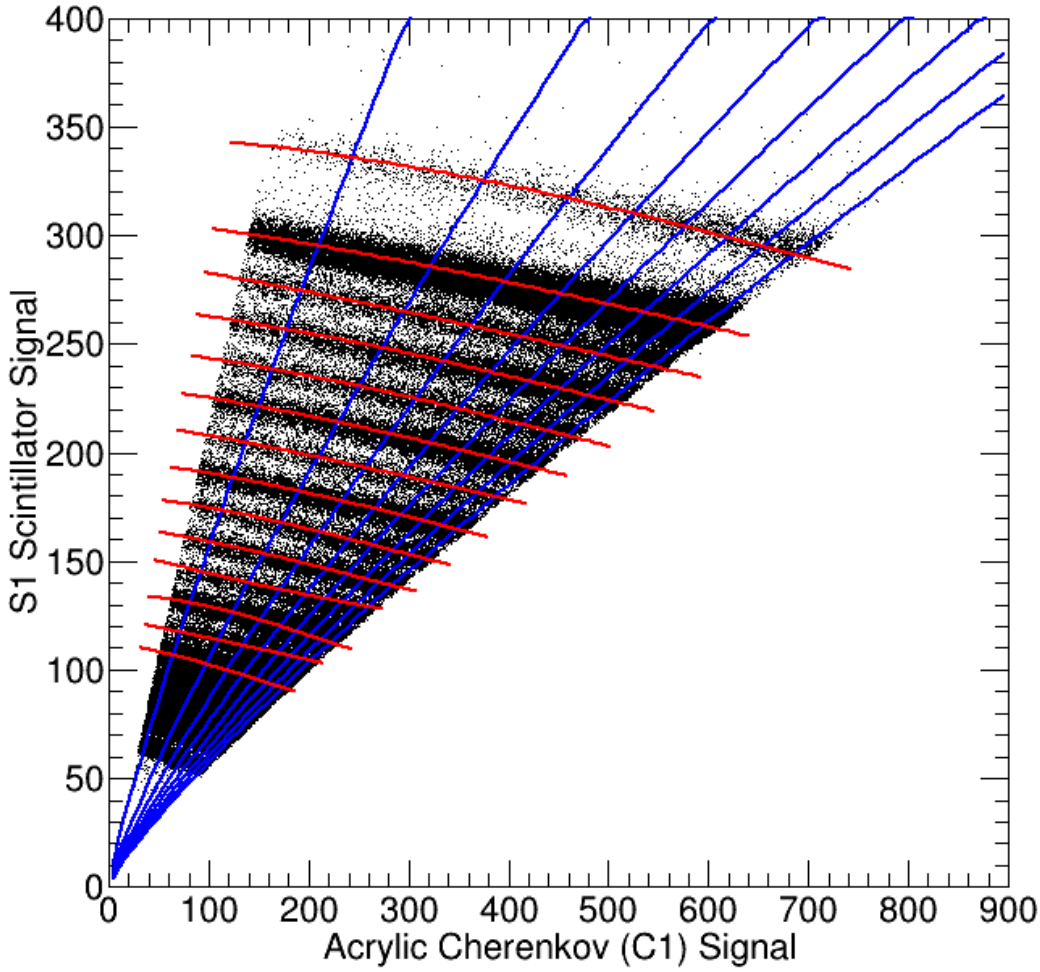

Figure 4.17: Curves of constant charge and curves of constant energy on the S1 vs C1 plot.

given by $S = Z^{1.7}$. This approximation was developed for the TIGER scintillator detectors by Link (2003), which were very similar to the SuperTIGER scintillator detectors. This approximation was used the first iteration through the Below C0 analysis method to assign a charge. After that iteration, I used a more complex approximation for Z, which assumed that S1 $\sim Z^{\alpha}$, with α a function of C1 and $S^{1/1.7}$. The curves of constant "Energy" were therefore derived as follows:

$$\frac{C1}{Z_1^2} = \xi. \tag{4.8}$$

Where ξ is a constant that is the same for particles with the same β. Here, Z_1 is the charge determined after iterating this charge assignment method once, assuming that $S = Z^\alpha$, where α is a function of C1 and $S^{1/1.7}$:

$$Z_1 = S^{1/\alpha},$$

$$\alpha = K_0 + K_1\frac{C1}{Z_0^2} + K_2\left(\frac{C1}{Z_0^2}\right)^2 + K_3\left(\frac{C1}{Z_0^2}\right)^3 + K_4\left(\frac{C1}{Z_0^2}\right)^4 + K_5\left(\frac{C1}{Z_0^2}\right)^5 + K_6\left(\frac{C1}{Z_0^2}\right)^6, \quad (4.9)$$

where Z_0 is given by:

$$Z_0 = S^{1/1.7}.$$

The curves of constant charge defined by Equation 4.8 therefore depend on S, C1, and a constant. I used 50 curves of constant "Energy", each with a different constant ξ. These curves were chosen so that a roughly even number of Iron events were between each line. The curves of constant "Energy" and curves of constant charge can be seen in Figure 4.17. For each curve of constant "Energy", I found the intersection with each curve of constant charge from $Z = 14$ to $Z = 28$ (except for $Z = 27$) and plotted the S value of the intersection against Z, as shown in Figure 4.18. I then fit these plots of S as a function of Z with various models of scintillator response. Because these were fit along curves of roughly constant energy, the energy-independent form of each model could be used, greatly simplifying the process. A more detailed analysis of the models tried can be found in Appendix D, but the best model tested was the Voltz Model described in Equation 4.10, which has three parameters:

$$\frac{dL}{dx} = AZ^2 + BZ^2e^{-CZ^2}. \quad (4.10)$$

Fitting the Voltz Model gave a unique set of these three parameters A, B, and C for each curve of constant "Energy". Within each angle bin, I then plotted the parameter value as a function of "Energy" for each parameter, and fit that plot with a 6th-order polynomial.

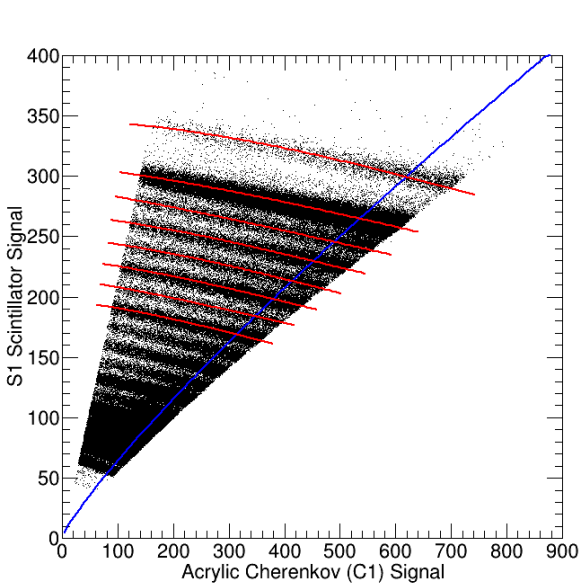

(a) One typical curve of constant "Energy" and the curves of constant charge it intersects.

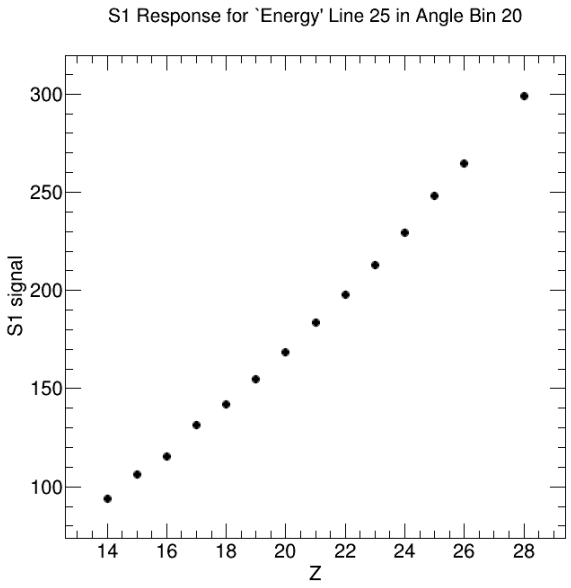

(b) The S1 value of the intersection of the curves of constant Z with this particular curve of constant E. This plot was then fit with the Voltz Model as defined in Equation 4.10 and the other scintillator response functions discussed in Appendix D.

Figure 4.18: Finding S as a function of Z for a curve of constant "Energy".

Figure 4.19 shows the "Energy" dependence of the three Voltz model parameters for a typical angle bin. For an arbitrary "Energy" defined by Equation 4.8 we can therefore calculate a unique set of three model parameters for each angle bin. These three parameters also depend on angle, and to generalize this to arbitrary angles, I simply interpolate between angle bins. For every unique incidence angle θ and "Energy", a unique set of parameters can be found based on the fit, and equation 4.10 can be solved for Z.

This method is applied to assign charges to the Below C0 data set using S1 and S2 as the scintillator function separately. The S1 and S2 charge assignments are then averaged to get a combined Below C0 charge. This method was also used historically to assign charge using the other scintillator response functions described in Appendix D.

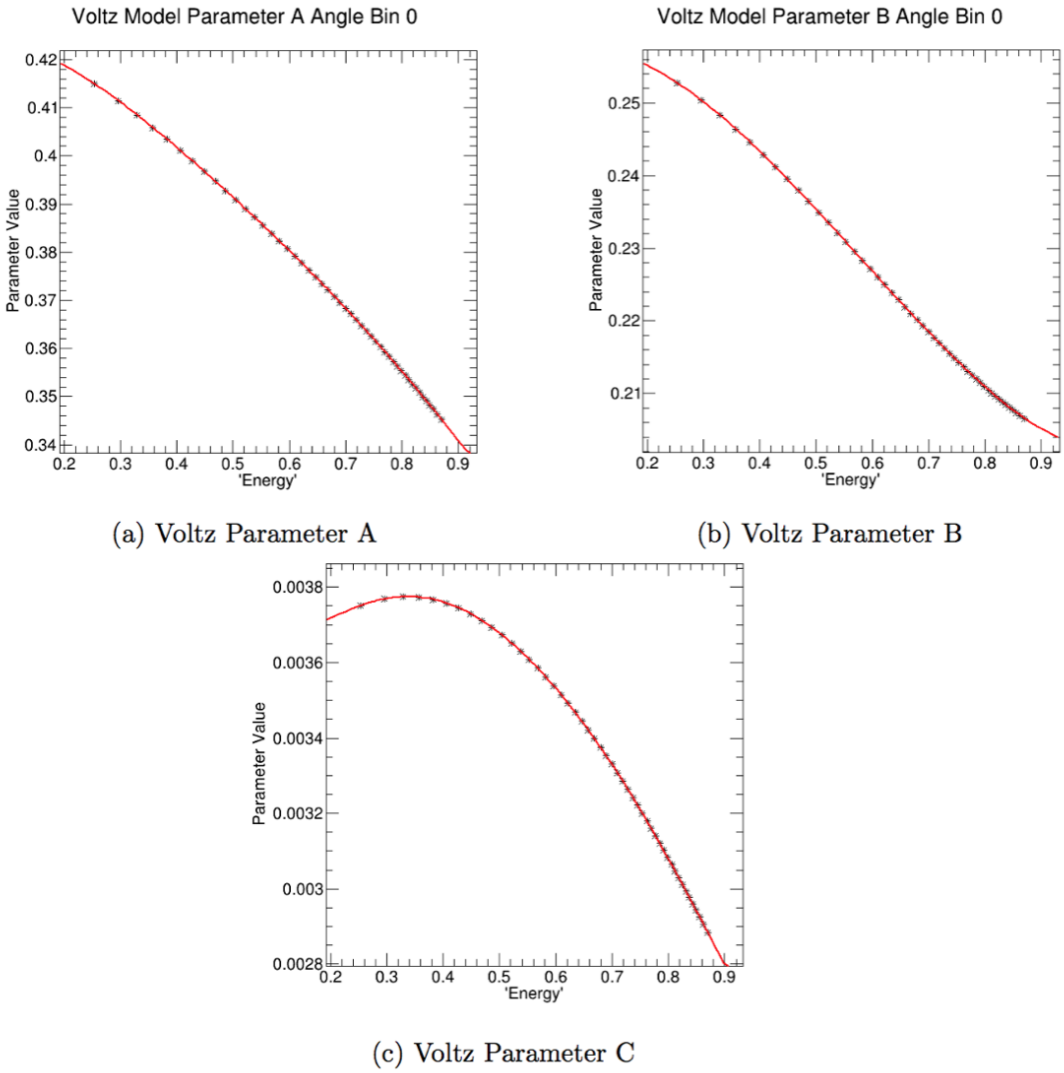

(a) Voltz Parameter A

(b) Voltz Parameter B

(c) Voltz Parameter C

Figure 4.19: "Energy" dependence of the Voltz model parameters A, B, and C defined in Equation 4.14.

4.4.1 Re-normalization

Figure 4.20 shows a histogram of the charge Z generated using the Below C0 method and the Voltz model as described above for both S1 and S2. Well defined, single-element peaks are visible, but the peaks are not evenly spaced and are not entirely aligned with integer charges. In addition, the S1 and S2 peaks are not aligned with each other, which leads to significantly worse charge resolution when the two charges are added together.

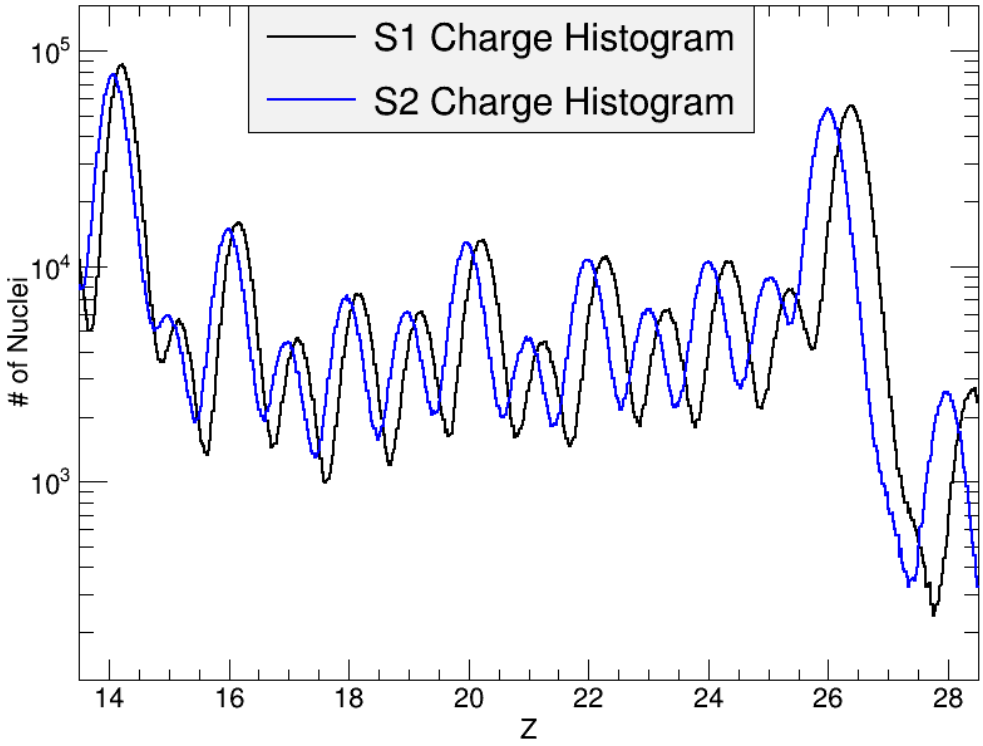

Figure 4.20: Charge histograms from S1 and S2 before re-normalization. The renormalization ensures that the individual charge peaks line up before combining the two charge assignments.

Since we know that the cosmic-ray nuclei that pass through the detectors do not contain any fractional charges, we re-normalize the data by applying a small linear correction that ensures that the $Z = 14$ and $Z = 28$ peaks align with their integer values for both S1 and S2. This correction was found by fitting the $Z = 14$ and $Z = 28$ peaks in 10 "Energy" bins in each of the 30 angle bins used previously, and re-normalizing all of the data within each angle and "Energy" bin so that these peaks lined up with integer values. This allowed the successful combination of the S1 and S2 charges, and led to a histogram with improved charge resolution, as shown in Figure 4.21. This re-normalization was successful at combining the two scintillator charges, but in order to combine the Below C0 data with the above C0 data, I added another step in the re-normalization. This took the resulting combined Below C0 histogram from the previous paragraph and fit a gaussian to every even-Z peak from $Z = 12$

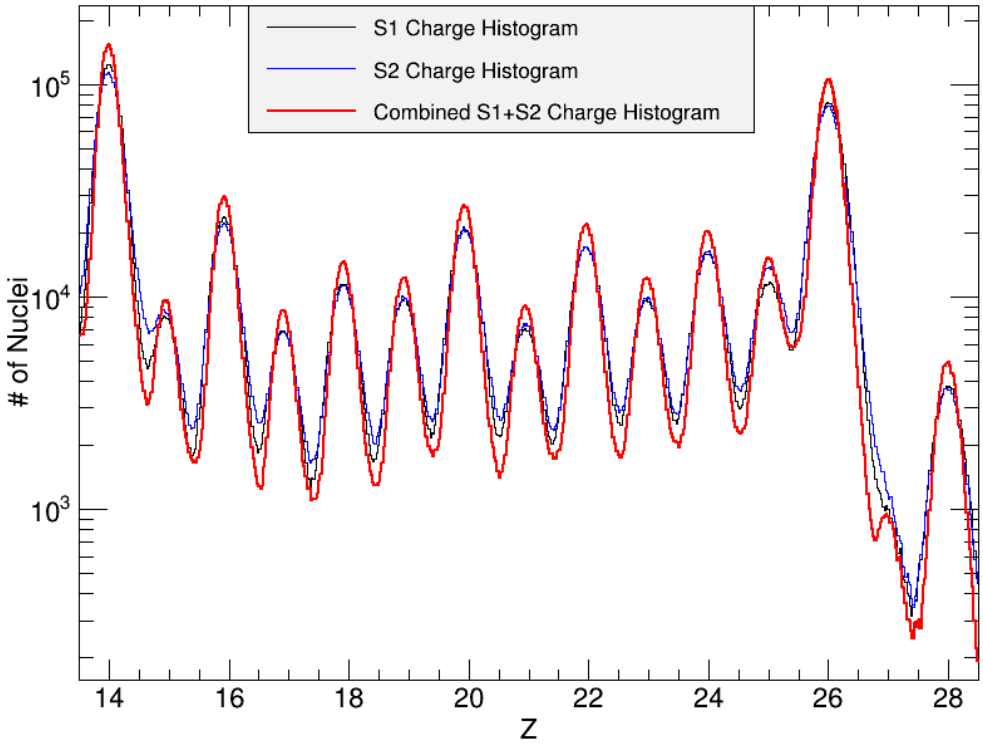

Figure 4.21: S1, S2, and combined (S1+S2)/2 charge histograms after renormalization.

to $Z = 38$. I then fit a 4th-order polynomial to the difference between the fitted peak locations and their corresponding integer Z values, and applied this 4th-order correction to all of the Below C0 data. The resulting data set had well-defined, single-element peaks that fell within 0.01 charge units of an integer value from $Z = 12$ to $Z = 38$. Figure 4.22 shows this charge histogram.

4.4.2 Scintillator Saturation

The SuperTIGER scintillator detectors provide a measurement of the amount of light emitted by the radiator as a function of the path length traversed by the ionizing particle, $\frac{dL}{dX}$. The radiator of each scintillator is comprised of a base material, with a small amount

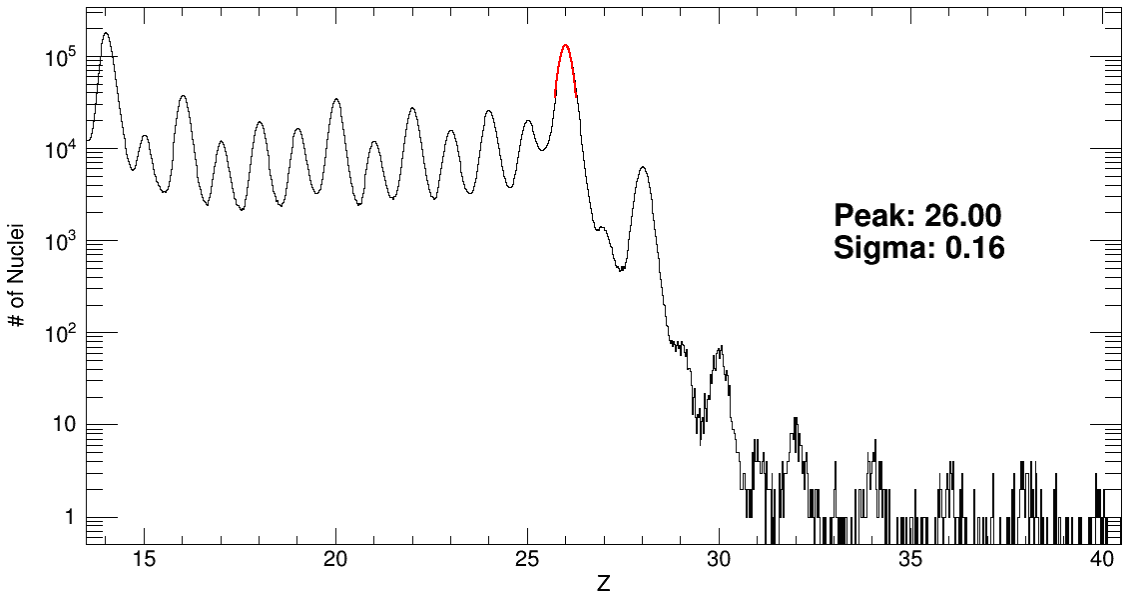

Figure 4.22: Charge histogram for the Below C0 data set after final renormalization..

of primary and secondary dyes. In an ideal scintillator, the amount of scintillation light produced will be proportional to the energy loss given by the Bethe-Bloch equation (adapted from the treatment in Leo (1994)):

$$-\frac{dE}{dx} = 2\pi N_A r_e^2 m_e c^2 \rho_{ab} \frac{Z_{ab}}{A_{ab}} \frac{Z^2}{\beta^2} \left[ln\left(\frac{2m_e\gamma^2 v^2 W_{max}}{I}\right) - 2\beta^2 - \delta - 2\frac{C}{Z_a b}\right]. \qquad (4.11)$$

The first several factors of this equation–N_a, Avogadro's number, r_e, the classical electron radius, m_e, the mass of the electron, c, the speed of light, and 2π–form a constant, $2\pi N_A r_e^2 m_e c^2 = 0.1535 MeV cm^2/g$. The remaining terms outside the bracket show that the amount of energy lost depends on atomic number to atomic mass ratio (Z_{ab}/A_{ab}) of the absorbing material, the density of the absorbing material ρ_{ab}, the charge of the incident particle squared (Z^2), and the inverse square of the relativistic velocity ($\frac{1}{\beta^2}$). The natural log term depends on the maximum energy that can be transferred in a single collision (W_{max}), the mean excitation potential of the absorbing medium (I), and the velocity of the incident particle ($v, \gamma = 1/\sqrt{1-\beta^2}$). For nuclei, the incident mass is much greater than the mass of an electron, so that $W_{max} \simeq 2m_e v^2\gamma^2$. The remaining terms include a quantum mechanical

correction ($-2C/Z_{ab}$), where C is a shell correction term), a term for the relativistic increase in energy loss ($-2\beta^2$), and a density correction ($-\delta$).

When a particle deposits a large amount of energy in a small volume of the scintillator, however, saturation occurs. This means that the actual energy converted to light as a function of path length (dL/dx) is a fraction of the stopping power (dE/dx) that decreases with increasing density of ionization. To fit the SuperTIGER Below C0 dataset, a number of different models of scintillator response were tested. For initial calibration and response cross-plots with scales roughly equivalent to integer charge units we used the simple assumption that the scintillator signal went as $S = Z^{1.7}$. This naive assumption is sufficient to find an Iron peak but does not give well-defined peaks for $Z > 26$.

Voltz et al. (1966) proposed that the region closest to the path of a sufficiently energetic particle (the "core") will be fully quenched, and therefore not sensitive to changes in dE/dx, while an outer region (the "halo"), will luminesce due to the energy deposited by knock-on electrons, and the light emitted in this region will depend on dE/dx. The Voltz Model is given in Ahlen (1980) as:

$$\frac{dL}{dx} = A_S \frac{dE}{dx}(1 - F_S) \exp\left[-B_S(1 - F_S)\frac{dE}{dx}\right] + A_S \frac{dE}{dx} F_S. \tag{4.12}$$

Here, A_S is an arbitrary scaling parameter, $\frac{dE}{dx}$ is the energy loss calculated from the Bethe-Bloch formula, B_S is a parameter describing the quenching behavior, and F_S is the fraction of total $\frac{dE}{dx}$ that escapes via knock-on electrons to the halo region. F_S is given by:

$$F_S = \frac{1}{2}\frac{ln(2m_e c^2\beta^2\gamma^2/T_o) - \beta^2}{ln(2m_e c^2\beta^2\gamma^2/I) - \beta^2}, \tag{4.13}$$

where I is the mean logarithmic ionization potential of the scintillator and T_o is a parameter describing the boundary between the core and the halo.

In the limit where the particles all have the same energy, $\frac{dE}{dx} \rightarrow C_{BB}Z^2$, the Voltz Model simplifies to a term that goes as Z^2 and a term that describes the energy that is not converted into light:

$$\frac{dL}{dx} = AZ^2 + BZ^2 e^{-CZ^2}, \tag{4.10}$$

where:

$$A = A_S C_{BB} F_S,$$

$$B = A_S C_{BB}(1 - F_S),$$

$$C = B_S C_{BB}(1 - F_S),$$

$$C_{BB} = 2\pi N_A r_e^2 m_e c^2 \rho_{ab} \frac{Z_{ab}}{A_{ab}\beta^2} \left[ln\left(\frac{2m_e\gamma^2 v^2 W_{max}}{I}\right) - 2\beta^2 - \delta - 2\frac{C}{Z_a b}\right]. \tag{4.14}$$

This is the energy-independent form of the Voltz Model that was used to fit the data in the method from earlier in this section. The Voltz model was also used to model the response of the scintillator detectors from TIGER by Link (2003) and Rauch (2008). A discussion of the other scintillator response functions tested for the SuperTIGER data analysis can be found in Appendix D.

4.5 Combined Above and Below C0 Charge Assignments

Re-normalizing the charge histograms from both methods allowed for the combination of the two datasets. Figure 4.23 shows the combined histogram and charge resolution at Iron. Figure 4.24 shows the combined data with a coarser bin size to highlight the well-defined peaks in the $30 \leq Z \leq 40$ charge range. This combined dataset has excellent resolution and statistics for all elements in the range $30 \leq Z \leq 40$. This is the first time that all elements

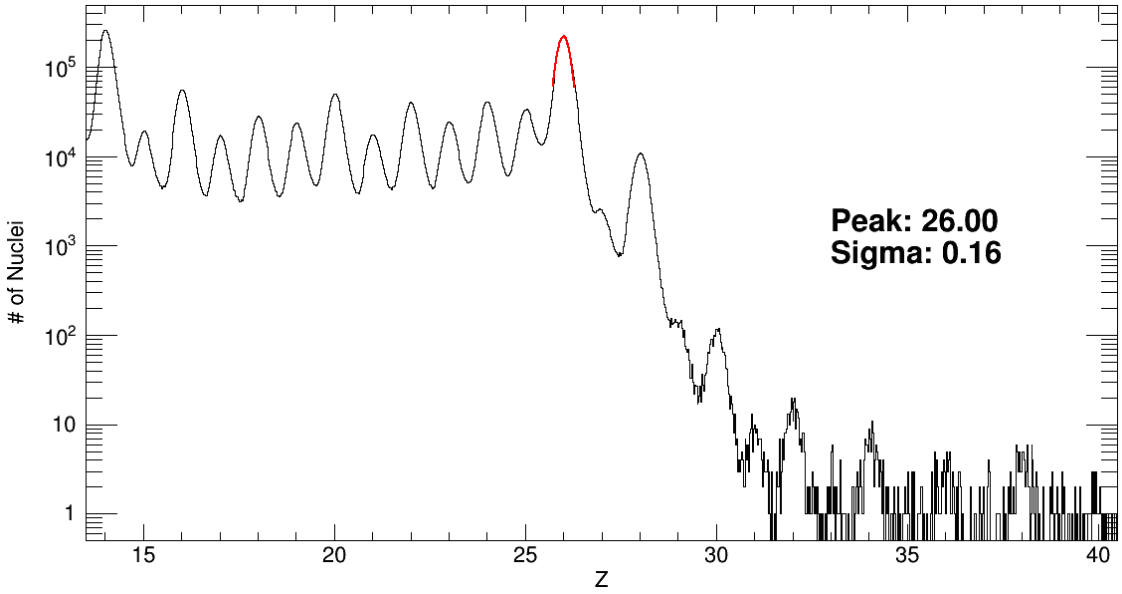

Figure 4.23: Combined Above and Below C0 charge histogram with 0.025 cu binning.

in this charge range have been measured in the Galactic Cosmic Rays with single-element resolution and good statistics.

4.6 Instrument Abundances

4.6.1 Multi-peak Gaussian Fitting

To determine the abundances of events with $Z < 33$, I used a multi-peak maximum likelihood fitting routine initially developed for ACE/CRIS by Scott (2005) and used on TIGER by Rauch (2008) called lsgaussfit. This routine uses a maximum-likelihood method to fit a multi-peaked gaussian function to an input file that contains data with peaks roughly one unit[9] apart and each having a similar standard deviation. The routine returns a location (in x) of each peak, the height of each peak, the area of each peak, and the standard deviation

[9]For SuperTIGER, this was always one charge, but the routine was also used to fit isotope data from ACE/CRIS, where individual isotope peaks are one atomic mass unit apart.

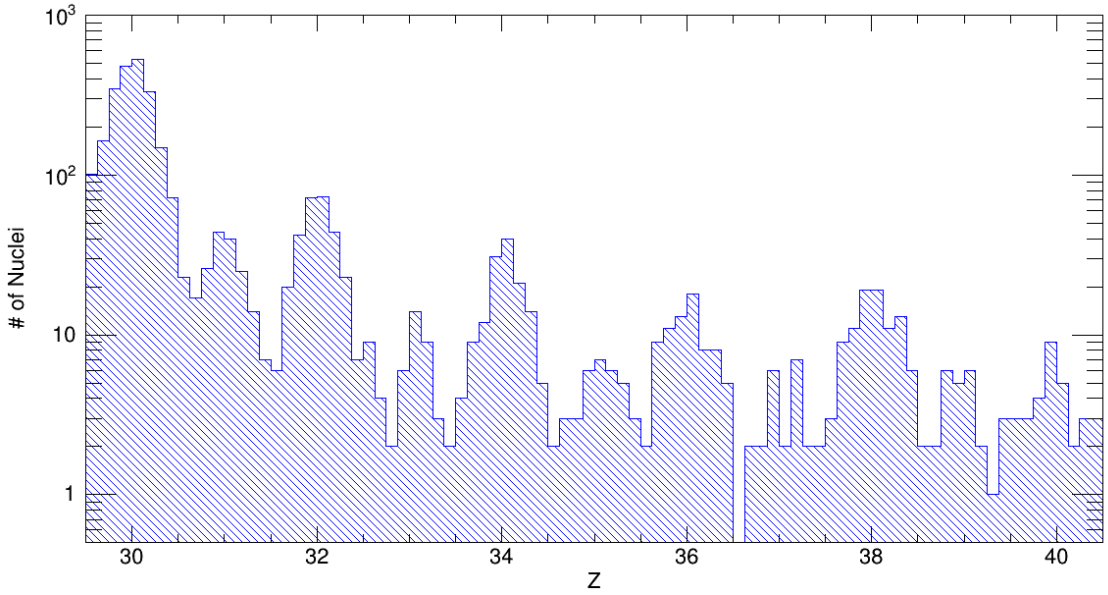

Figure 4.24: Combined charge histogram with 0.125 cu binning showing the UH charge range.

σ, which is assumed to be the same for all peaks. The fitting routine also provides a particle conservation index, which shows how many events the fit found divided by how many particles were in the input file, and for the SuperTIGER fits this conservation value was always within 0.3% of 1.

I assigned charge as described above, and then generated charge histograms for both the Above and Below C0 datasets. These histograms fit the requirements of the fitting routine, but subsequent tests found that the routine was more accurate (and significantly faster) fitting a smaller subset of the histogram than the entire charge range. I therefore generated text files containing the location of the bin center and bin content for a range of 5 cu around a particular peak–e.g. for $Z = 26$, the text file contained information about the histogram bins from $Z = 23.5$ to $Z = 28.5$. I then used the fitting routine to fit a 5-peak gaussian to the 5 single-element peaks in each charge range. This ensured that for the central peak in each 5-peak range, the fitting routine was able to fit the contamination from the two nearest peaks on either side. I then took the information from the central peak

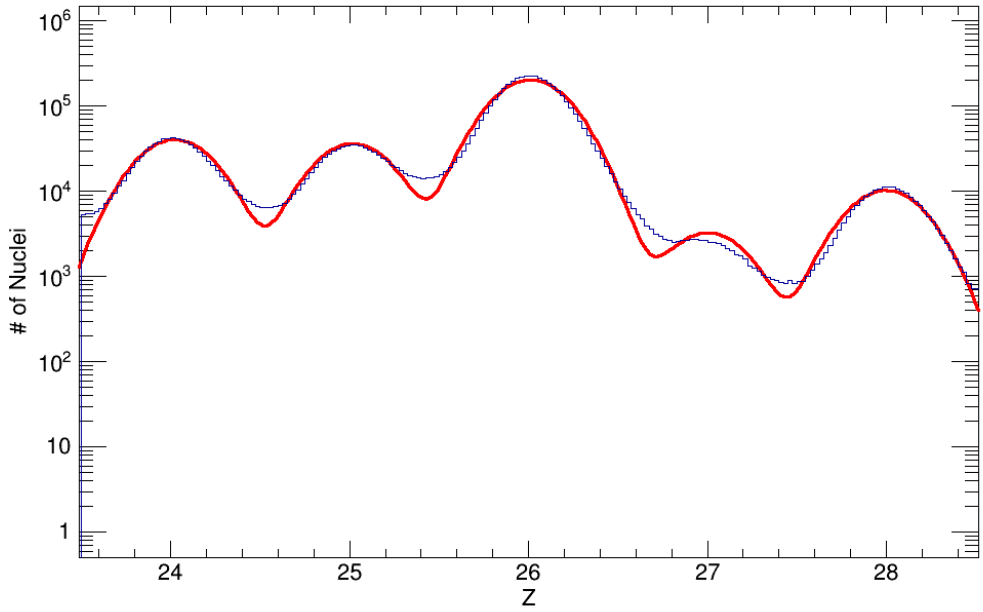

Figure 4.25: For Z $\leq$ 32, 5 adjacent peaks were fit with the multi-peak gaussian fitting routine developed by Scott (2005). A typical example set of 5 adjacent peaks is shown.

in each charge range and used that as the fit for the corresponding element. To find the $_{31}$Ga abundance, I used a similar method but with a 3 c.u. range and 3 peaks. This gave better results, as it eliminated spillover from the $_{28}$Ni peak, which is significantly more abundant. The 5 c.u. method was best for all other Z.

4.6.2 High-Z Method

For $Z \geq 33$ we simply counted the number of events for each Z. Figure 4.24 shows the well-defined, well-separated peaks in this charge range. To count, I first generated a list of all events with $Z \geq 30$. This list contained the charge Z generated using the charge method above, the incidence angle θ, and an indication of which method this charge Z was obtained using. I then sorted the list by Z from highest to lowest. Within this list, I looked for obvious divisions between peaks by looking at the difference in charge between a particular

Z	Element	**Above C0** events	(Fe=1)	**Below C0** events	(Fe=1)
26	Fe	1630390.1	1.00E+0	2529015.7	1.00E+0
27	Co	28270.5	1.73E-02	38439.2	1.52E-02
28	Ni	86386.6	5.30E-02	123543.2	4.89E-02
29	Cu	1546.4	9.49E-04	2090.7	8.27E-04
30	Zn	1017.5	6.24E-04	1274.0	5.04E-04
31	Ga	82.2	5.04E-05	100.8	3.99E-05
32	Ge	128.0	7.85E-05	181.0	7.16E-05
33	As	21	1.30E-05	25	9.95E-06
34	Se	60	3.66E-05	84	3.31E-05
35	Br	20	1.23E-05	17	6.72E-06
36	Kr	26	1.59E-05	49	1.94E-05
37	Rb	11	6.75E-06	16	6.33E-06
38	Sr	36	2.21E-05	67	2.65E-05
39	Y	12	7.36E-06	13	5.14E-06
40	Zr	15	9.20E-06	19	7.51E-06

Table 4.1: Maximum Likelihood fit results (for $Z \leq 32$) and counting method results (for $Z \geq 33$) for the full SuperTIGER combined dataset. For the Maximum Likelihood method, the combined charge histogram was fit separately from the Above and Below C0 histograms, so the number of events is slightly different.

event and its nearest neighbors in Z ($\Delta Z = Z_i - Z_{i-1}$ for the i-th event in charge). In general, these divisions were easy to spot by simply finding events with $\Delta Z >\sim 0.1$ c.u.. I then used multiple charge histograms with different bin sizes in this range to observe how binning affected the definition of the peaks and the location of the spaces in between them as a check that the divisions I was defining were reasonable. This method was effective at finding the division between every peak from $32 \leq Z \leq 39$. For the $Z = 40$ peak, I was unable to find a reasonable way to draw the line, so I simply fixed the boundary at $Z = 40.5$.

4.6.3 Numbers of Events

Table 4.1 shows the Maximum Likelihood fit results (for $Z \leq 32$) and counting method results (for $Z \geq 33$) for the combined dataset. These numbers were found using the loose

Z	Element	N TIGER	N SuperTIGER	ST/TIGER
26	Fe	556013.6	4159405.8	7.5
27	Co	7078.4	66709.6	9.4 *
28	Ni	27397.2	209929.8	7.7
29	Cu	413.8	3637.1	8.8 *
30	Zn	312.6	2291.5	7.3
31	Ga	39.4	183.0	4.6
32	Ge	34.2	309.0	9.0
33	As	4.9	46.3	9.4
34	Se	30.1	143.3	4.8
35	Br	5.8	37.0	6.4
36	Kr	9.4	75.0	8.0
37	Rb	6.3	27.0	4.3
38	Sr	10.4	103.0	9.9
39	Y	0.0	25.0	n/a
40	Zr	2.1	34.0	16.5

Table 4.2: Comparison of Combined Above and Below C0 instrument numbers of events from TIGER and SuperTIGER. The TIGER results are the results of a maximum likelihood fit from Rauch (2008). The SuperTIGER results are simply the sum of the Above and Below C0 numbers from Table 4.1. The SuperTIGER/TIGER ratio is also shown. *For $_{27}$Co and $_{29}$Cu, we report the SuperTIGER maximum likelihood fits for our loose interaction cut regime. The TIGER abundances were based on an extremely restrictive set of interaction cuts. We plan to derive abundances using an extremely restrictive interaction cut regime for the SuperTIGER data in the future.

interaction cut regime discussed in Section 4.2. These observed numbers of events and abundances have not been corrected for interactions within the instrument or en route through atmosphere or galaxy. These corrections will be discussed in detail in Chapter 5. The $_{27}$Co and $_{29}$Cu abundances shown here are the results of the fitting routine using the standard loose interaction cuts; to get more accurate measurement, a harsher interaction cut regime is necessary. Table 4.2 shows how the number of events for each Z recorded by SuperTIGER compares to the numbers observed by TIGER.

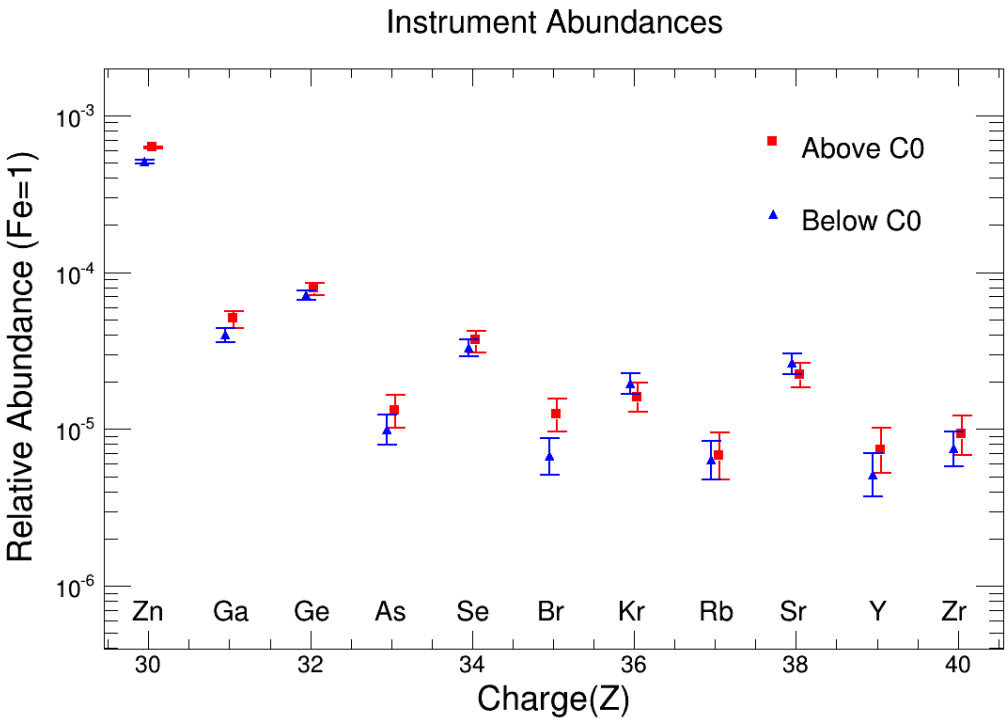

Figure 4.26: Comparison of Above C0 (Red) and Below C0 (Blue) instrument abundances with statistical uncertainties.

4.6.4 Comparison of Above and Below C0 Abundances

Figure 4.6 shows the abundances calculated for the Above and Below C0 methods in the charge range $30 \leq Z \leq 40$. The error bars represent statistical uncertainties. For elements with $N \geq 100$, we simply assigned a $\pm\sqrt{N}$ statistical uncertainty on N. For elements with $N < 100$, we used the upper and lower limits calculated by Gehrels (1986). With the exception of $_{30}$Zn and $_{35}$Br, the abundances calculated with the two methods agree to within statistical uncertainties. The $_{30}$Zn discrepancy is more troubling, but we have yet to come up with a satisfactory answer. The $_{35}$Br detected in the instrument is mostly secondary and the statistical error bars nearly intersect, so we decided that this near-agreement was sufficient and that the abundances from the two methods could be combined.

The Above and Below C0 abundances shown in Figure 4.6 and Table 4.1 are used as the starting point for the process of obtaining Galactic Cosmic Ray Source abundances described in Chapter 5.

Chapter 5

Derivation of Galactic Cosmic Ray Source Abundances

The instrument abundances reported in Section 4.6 represent the measured abundances of Galactic Cosmic Ray (GCR) particles within the active area of the instrument. These GCR are a mix of primary cosmic rays, secondary cosmic rays produced while traveling from the GCR source to Earth, and secondary particles created by GCR interactions within the atmosphere and the instrument itself. To derive Galactic Cosmic Ray Source (GCRS) abundances from this measurement, we need to correct for the contributions to the observed GCR abundances from these secondary sources. First, we adjust the GCR abundances for interactions that occurred within the instrument. Then, we correct for interactions within the atmosphere and incorporate a normalization factor to account for varying amounts of energy loss for each charge Z. Finally, we correct for secondary cosmic ray formation *en route* from the GCR source and derive our GCRS abundances.

5.1 Interactions Within the SuperTIGER Instrument

To find the flux at the top of the instrument, we need to calculate the fraction of each element that interacted within the instrument. The interaction cuts discussed in Section 4.2 eliminated those cosmic-ray particles that underwent nuclear interactions within the instrument that resulted in a change in charge Z. After determining the number of nuclei of each element observed in the instrument (see Table 4.1), we then corrected for interactions within the instrument using interaction mean free paths (based on the total charge changing cross-sections from Nilsen et al. (1995)) for each Z, and the appropriate path length within the instrument for each of the types of material that make up the SuperTIGER detector. We treated each type of material as a separate slab, and calculated the number of nuclei there must have been at the top of the slab to give us the number we observed at the bottom.

For a given type of material i, the number of nuclei at the top is given as follows:

$$N_i(TOP) = \frac{N_i(BOT)}{e^{-x_i/\lambda_i(Z)}}.$$

Where x_i is the thickness in g/cm^2 of the material and $\lambda_i(Z)$ is the interaction mean free path of a nucleus of charge Z in the material. This was repeated for each layer of the material. The interaction mean free paths we used were calculated based on works by Nilsen et al. (1995) and Westfall et al. (1979). A full table of these interaction mean free paths, which were also used for the same correction on the TIGER experiment, can be found in Rauch (2008). We used the total charge-changing cross sections because our interaction cuts eliminate those events that interact and change charge within the detector, so we do not need to worry about interacted higher-Z events showing up as lower-Z events in the data. The SuperTIGER detector cannot tell the difference between nuclei that interact and undergo a change in mass without a change in charge, so the total charge changing cross-sections are

appropriate. For the Above C0 dataset, we corrected for all the material above the center of the C1 radiator, as no detectors located physically below the C1 radiator were used in the analysis. For the Below C0 dataset, we corrected for the material above the center of the S2 radiator. We corrected for nuclear interactions that occurred between these starting points and the top of the S1 radiator.

The areal densities of each material in the SuperTIGER detector are shown in Table 5.1. This Table gives the areal densities used for the interaction corrections, from the C1 detector to the top of the active area of the instrument and from the S2 detector to the top of the active area. For reference, the total areal densities of each material in the instrument and the areal densities of the small amount of detector material above the active area are included. This material above the active area is treated as if it were a part of the atmospheric overburden, as we are unable to distinguish events that undergo nuclear interactions in this material from events that did so in the atmosphere. Appendix E contains a detailed description of the thicknesses of each material within the detector.

Material	C1 to Top g/cm^2	S2 to Top g/cm^2	C0 to top g/cm^2	S3 to Top g/cm^2	Above Active Area g/cm^2
Aluminum	0.325	0.420	0.222	0.609	0.030
PVT	1.046	2.093	1.046	3.139	0
PMMA	1.499	1.499	0.023	1.499	0.040
PS	0.395	0.382	0.284	0.648	0
PE	0.009	0.009	0.009	0.018	0
Rohacell	0.107	0.188	0.091	0.279	0
SiO_2	0.614	0.614	0.307	0.614	0
Mylar	0.053	0.072	0.055	0.109	0.025
Total	4.048	5.276	2.038	6.916	0.098

Table 5.1: The areal densities for each type of material in the SuperTIGER instrument for various interaction and energy corrections. PVT is Polyvinyltoluene, used in the Scintillator radiators; PMMA is Polymethyl Methacrylate, used in the Acrylic Cherenkov counter; PS is Polystyrene; PE is Polyethylene. A more detailed table of the materials in the SuperTIGER Instrument can be found in Appendix E.

We then determined the Top-of-Instrument abundances, normalized to $_{26}$Fe=1. We assigned a statistical uncertainty to each number of nuclei before the instrument interaction correction. For elements with $N \geq 100$, we simply assigned a $\pm\sqrt{N}$ uncertainty on N. For elements with $N < 100$, we used the upper and lower limits calculated by Gehrels (1986). We used these uncertainties to calculate fractional uncertainties in N for each Z. We took the same fractional uncertainties on N as the fractional uncertainties for N_{TOI}, the number of each element corrected to the top of the instrument. To find the uncertainties of the Top-of-Instrument ratios, which are $\mathrm{N}_{TOI}(Z)/\mathrm{N}_{TOI}(Fe)$, we add the fractional uncertainties of $\mathrm{N}_{TOI}(Z)$ and $\mathrm{N}_{TOI}(Fe)$ in quadrature, to get the fractional uncertainty of the Top-of-Instrument abundances for each Z.

The Combined abundances use the Above and Below C0 numbers for each Z propagated separately through the instrument and then added together. The uncertainties of the Combined abundances were calculated by finding the uncertainty in the Combined N_{TOI}(Z) for each element, then using this to find a fractional uncertainty. This fractional uncertainty for each Z was added in quadrature to the fractional uncertainty for $\mathrm{N}_{TOI}(Fe)$ to get a fractional uncertainty in the relative abundance, which was then multiplied by the relative abundance to give the uncertainties shown. The SuperTIGER Top-of-Instrument abundances (normalized to $_{26}$Fe=1 can be found in Tables 5.2 and 5.3.

5.2 Correction for Energy Losses in the Atmosphere and Instrument

As a cosmic-ray particle travels through the atmosphere and the SuperTIGER instrument, it gradually loses energy. This energy loss depends on the charge and atomic mass of the particle, the initial energy of the particle, and the type and thickness of the material it is

Z	**Above C0**	N_{RAW}	N_{TOI}	Fe=1	errors low	high
26	Fe	1630390.1	2610816.8	1.00E+00	7.83E-04	7.83E-04
27	Co	28270.5	45912.6	1.76E-02	1.05E-04	1.05E-04
28	Ni	86386.6	140147.2	5.37E-02	1.83E-04	1.83E-04
29	Cu	1546.4	2563.4	9.82E-04	2.50E-05	2.50E-05
30	Zn	1017.5	1700.3	6.51E-04	2.04E-05	2.04E-05
31	Ga	82.2	139.9	5.36E-05	5.89E-06	6.57E-06
32	Ge	128.0	220.4	8.44E-05	7.46E-06	7.46E-06
33	As	21.1	36.8	1.41E-05	3.03E-06	3.77E-06
34	Se	59.6	105.4	4.04E-05	5.25E-06	5.95E-06
35	Br	20	35	1.36E-05	3.01E-06	3.77E-06
36	Kr	26	47	1.79E-05	3.50E-06	4.25E-06
37	Rb	11	20	7.64E-06	2.27E-06	3.07E-06
38	Sr	36	66	2.52E-05	4.18E-06	4.94E-06
39	Y	12	22	8.44E-06	2.40E-06	3.21E-06
40	Zr	15	28	1.06E-05	2.72E-06	3.52E-06
Z	**Below C0**	N_{RAW}	N_{TOI}	Fe=1	errors low	high
26	Fe	2529015.7	4533128.0	1.00E+00	6.29E-04	6.29E-04
27	Co	38439.2	70114.6	1.55E-02	7.89E-05	7.89E-05
28	Ni	123543.2	225048.3	4.96E-02	1.41E-04	1.41E-04
29	Cu	2090.7	3912.1	8.63E-04	1.89E-05	1.89E-05
30	Zn	1274.0	2407.7	5.31E-04	1.49E-05	1.49E-05
31	Ga	100.8	195.0	4.30E-05	4.28E-06	4.28E-06
32	Ge	181.0	355.3	7.84E-05	5.83E-06	5.83E-06
33	As	25.2	50.0	1.10E-05	2.18E-06	2.66E-06
34	Se	83.7	169.8	3.75E-05	4.10E-06	4.56E-06
35	Br	17	35	7.64E-06	1.83E-06	2.34E-06
36	Kr	49	102	2.24E-05	3.20E-06	3.69E-06
37	Rb	16	33	7.38E-06	1.83E-06	2.34E-06
38	Sr	67	142	3.12E-05	3.82E-06	4.30E-06
39	Y	13	28	6.10E-06	1.67E-06	2.21E-06
40	Zr	19	41	9.01E-06	2.05E-06	2.58E-06

Table 5.2: Top-of-Instrument abundances for the Above C0 and Below C0 datasets. N_{RAW} is the number of nuclei detected in the instrument from Table 4.1. N_{TOI} is the number of nuclei calculated for the Top-of-Instrument.

Z		**Combined** N_{RAW}	N_{TOI}	errors Fe=1	low	high
26	Fe	4159405.8	7143944.7	1.00E+00	6.85E-04	6.85E-04
27	Co	66709.6	116027.1	1.62E-02	8.90E-05	8.90E-05
28	Ni	209929.8	365195.5	5.11E-02	1.60E-04	1.60E-04
29	Cu	3637.1	6475.5	9.06E-04	2.11E-05	2.11E-05
30	Zn	2291.5	4108.0	5.75E-04	1.69E-05	1.69E-05
31	Ga	183.0	334.9	4.69E-05	4.87E-06	5.12E-06
32	Ge	309.0	575.8	8.06E-05	6.42E-06	6.42E-06
33	As	46.3	86.8	1.21E-05	2.49E-06	3.07E-06
34	Se	143.3	275.2	3.85E-05	4.52E-06	5.07E-06
35	Br	37	70	9.81E-06	2.26E-06	2.86E-06
36	Kr	75	149	2.08E-05	3.31E-06	3.89E-06
37	Rb	27	53	7.48E-06	1.99E-06	2.61E-06
38	Sr	103	207	2.90E-05	3.95E-06	4.54E-06
39	Y	25	50	6.96E-06	1.94E-06	2.57E-06
40	Zr	34	69	9.61E-06	2.29E-06	2.92E-06

Table 5.3: Combined Top-of-Instrument abundances from the SuperTIGER instrument. N_{RAW} is the combined number of nuclei detected in the instrument from Table 4.1. N_{TOI} is the combined number of nuclei calculated for the Top-of-Instrument.

traveling through (which in turn depends on the incidence angle, as wider-angle particles travel through more material). Thus, while all particles at the $n = 1.04$ Aerogel Cherenkov (C0) threshold have nearly the same energy within the C0 radiator, that energy corresponds to a different energy at the top of the atmosphere for each element. Since heavier elements lose more energy traversing the same amount of material, it is necessary to include a normalization factor in the Top-of-Atmosphere abundances to ensure that we are deriving relative abundances using the same energy range for each Z to avoid biasing the data against higher-Z particles. Therefore, we need to find a good estimate of the energy range we are measuring for each Z at the detector, find the energy range that it corresponds to at the top of the atmosphere, and then normalize the abundances so that we are sampling the same energy bin for each Z. This normalization is based on an integral $_{26}$Fe spectrum in the observed energy range for each element.

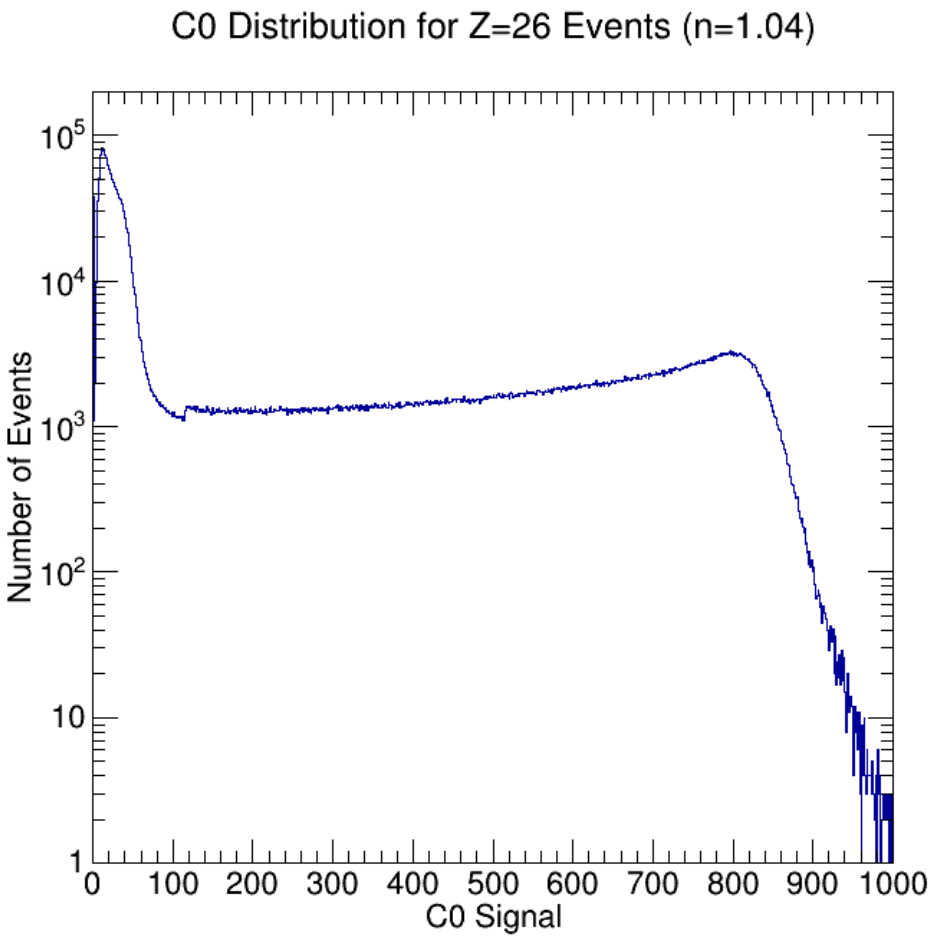

Figure 5.1: Distribution of signals in the n=1.04 Aerogel (C0) counter. The large peak on the left is scintillation signal within the Aerogel. The Cherenkov threshold is apparent in the sharp discontinuity at C0$\sim$115.

5.2.1 Determining the Energy Ranges

First, we must determine the energy ranges measured within the instrument. Theoretically, we begin using the Below C0 threshold at the C1 threshold of 325 MeV/nucleon, and the Above C0 method at the C0 thresholds of 2.5 and 3.3 GeV/nucleon, depending on which half-module the particle passes through. However, the Above C0, Below C0, and low-energy cuts defined in Chapter 4 are not perfectly aligned with the Cherenkov thresholds and are not perfectly Z- and energy-independent. Therefore, we need to find the energies of these cuts for each Z. Figure 5.1 shows a histogram of the C0 values for all $_{26}$Fe events on a

logarithmic vertical scale. It is dominated by a large peak on the left, which is scintillation signal within the C0 detector for those events below the C0 threshold passing through the detector. The C0 threshold, where light from Cherenkov emission takes over is apparent at C0$\sim$115. From that point on, the Cherenkov signal from the primary cosmic ray particle is given by Equation 2.4, with a slight offset A that represents the signal at the C0 threshold (where $\beta = \frac{1}{n}$, causing the 1-1/($\beta^2 n^2$) term to go to 0):

$$L_{C0} = K_{C0} Z^2 \left(1 - \frac{1}{\beta^2 n_{C0}^2}\right) + A. \tag{5.1}$$

To figure out the β value of our $n_{C0} = 1.04$ threshold cut, we need to find an estimate for K_{C0} and A. We found A by simply looking at the histogram in Figure 5.1 and noting where the uptick due to Cherenkov radiation occurred. To find K_{C0}, we must find the signal where $\beta = 1$. While Equation 5.1 describes the amount of light created from the Cherenkov effect, the histogram in Figure 5.1 shows that emission convolved with the input energy spectrum at the top of the atmosphere, and then smeared by a gaussian due to the limits of the detector resolution and contributions from knock-on electrons. Pinpointing the $\beta = 1$ location is therefore difficult, but we need only a reasonable approximation in order to get the limits we need for our energy integral.

Determining the Aerogel Cherenkov Thresholds and Below C0 Low-Energy Cut Energies

For determining the Cherenkov thresholds, we used two different assumptions to find $\beta = 1$: the peak of the Cherenkov signal distribution (on the right of Figure 5.1) and the far right half-maximum of the distribution. Previous analysis of the TIGER data showed that the $\beta = 1$ value would be located somewhere between these two signal values. Using these two assumptions, we calculated the β values of the Cherenkov threshold cuts for the

$n = 1.04$ and $n = 1.025$ Aerogel thresholds, and the β value of the Below C0 low-energy cut in C1. The difference in energy between the thresholds calculated by each method was ∼1%, so we used the average of the two energies as the limits to our integration for the energy correction factors. These average minimum detectable energies for each Z can be found in Table 5.4.

Energies in the SuperTIGER Instrument

Z		n=1.04 threshold cut MeV/nucleon in C0 radiator	n=1.025 threshold cut MeV/nucleon in C0 radiator	Low Energy threshold cut MeV/nucleon in C1 radiator	Below C0 cutoff MeV/nucleon in C1 radiator
26	Fe	2737	3650	420	2084
27	Co	2735	3649	420	2084
28	Ni	2734	3649	420	2084
29	Cu	2732	3649	420	2085
30	Zn	2731	3649	419	2085
31	Ga	2729	3649	419	2086
32	Ge	2728	3649	419	2087
33	As	2727	3648	419	2088
34	Se	2726	3648	419	2089
35	Br	2726	3648	419	2090
36	Kr	2725	3648	419	2091
37	Rb	2724	3648	418	2092
38	Sr	2723	3648	418	2094
39	Y	2723	3648	418	2095
40	Zr	2722	3648	418	2096

Table 5.4: Values of the various energy cuts within the SuperTIGER instrument for each Z.

Determining the Below C0 Cutoff Energy

Initially, we used the same methods to determine β, and therefore the detector constant K_{C1}, that we used for the Below C0 low-energy cut to assign an energy value to the Below C0 cutoff cut described in Chapter 4. However, the two methods different considerably (∼15%), so we used an alternate method to determine the detector constant K_{C1}. We isolated the

$_{26}$Fe contour on the C1 vs C0 cross plot (Figure 4.2) by taking those events above the C0 threshold that were identified as $_{26}$Fe, and then fit a line to the points. This was done for both the $n = 1.04$ and $n = 1.025$ C0 counters. Using the line that we fit to the distribution and a slightly modified version of Equation 4.3 (to account for the intercept we added to Equation 2.4 in Equation 5.1):

$$L_{C1} = Z^2 K_{C1} \left(\frac{{n_{C1}}^2 - n_{C0}^2}{n_{C1}^2} \right) + \frac{n_{C0}^2}{n_{C1}^2} \frac{K_{C1}}{K_{C0}} (L_{C0} - A_{C0}) + A_{C1}. \tag{5.2}$$

We were able to find the detector constant K_{C1}, using values for A_{C0} and A_{C1} derived from the C0 and C1 signal histograms. We determined K_{C1} using both the $n = 1.04$ and $n = 1.025$ C0 data, and these K_{C1} agreed to within 1%. To double-check that this was a reasonable value of K_{C1}, we used it to determine the location of $\beta = 1$. As Figure 5.2 shows, the initial value for $\beta = 1$ (blue line) was lower than the values of the C1 peak and half-maximum, which we expected it to be between.

We then included a correction for the signal contribution due to knock-on electrons. Using a parameterization of the knock-on electron curve in Grove and Mewaldt (1992) developed by Georgia de Nolfo during analysis of the TIGER instrument, we calculated the contribution to the signal from knock-on electrons we would expect. This shifted our predicted $\beta = 1$ value (red line) into the region we expected it to be in, as shown in Figure 5.2.

We then determined the β value of the Below C0 cutoff for each Z and converted that to an energy in MeV/nucleon, which can be found in the rightmost column of Table 5.4. The value of the Below C0 cutoff is lower in energy than the value for the C0 threshold because of the Below C0 cut that was made in Section 4.4 to avoid events with saturated scintillator signals, which are difficult to assign charge to using the Below C0 method.

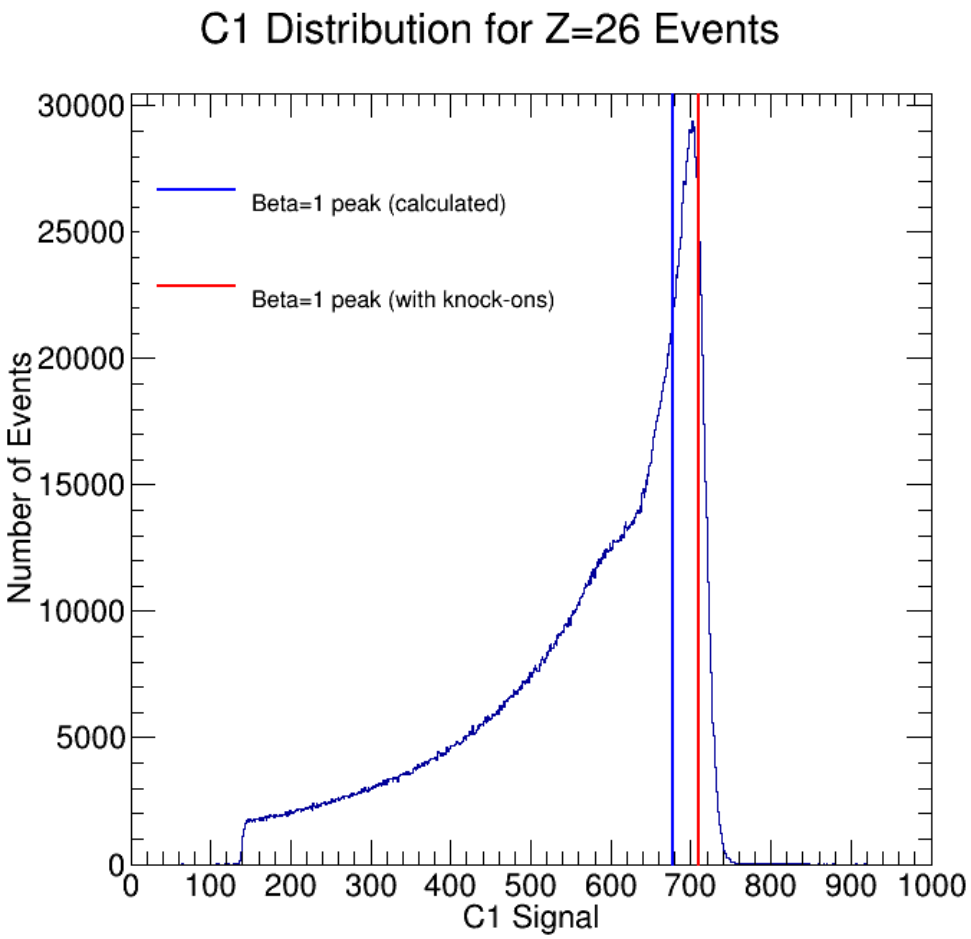

Figure 5.2: Distribution of signal in the Acrylic Cherenkov (C1) counter. The lines represent the C1 value at β=1 calculated using Equation 5.2 (blue) and that value shifted by a knock-on electron contribution (red). Only those particles that pass the Below C0 low energy cut are shown.

5.2.2 Calculating Energy Loss in the Atmosphere and Instrument

The energy lost by a cosmic-ray particle traveling through a given material depends on the charge and atomic mass of the particle, the initial energy of the particle, and the type and thickness of the material it is traveling through. To determine the energy loss, we used the online NIST PSTAR proton range table (NIST, 2015), which gives the distance a proton of a given energy can travel through a particular material before it loses all of its energy and stops. Given the energy per nucleon of a cosmic-ray particle at the bottom of a

slab of material E_b, we can look up the range of a proton with that energy in that material $R_P(E_b)$. We can then calculate the range of the proton at the top of the slab $R_P(E_t)$ using the equation:

$$R_P(E_t) = R_P(E_b) + \frac{Z_i^2}{A_i} x_{mat}, \tag{5.3}$$

where Z_i and A_i are the atomic number and mass of the incident particle, respectively. x_{mat} is the thickness, in g/cm^2 of the material in question. We can then look up the energy E_t that this range at the top of the slab $R_P(E_t)$ corresponds to. To simplify the process, values of the proton range in each material found in the SuperTIGER instrument at 10 MeV increments from 400 MeV to 5000 MeV were extracted from the NIST PSTAR proton range table, and a program was written to compute the range given a certain energy and energy given a certain range interpolating between these points. The proton ranges in each material in this energy range are smoothly-varying and roughly linear with energy, so this interpolation gives an accurate approximation.

We then treated each type of material within the SuperTIGER instrument as a separate slab. The thicknesses used are found in Table 5.1, which were then multiplied by the mean secant of incidence angle observed in flight. For the two Above C0 threshold cuts, we calculated the energy loss from the top of the instrument to the center of C0, including the material above the active area. For the Below C0 energies, we calculated the energy loss from the top of the instrument to the center of C1, again including the material above the active area. The material above the active area was treated as just another part of the appropriate slab for the energy corrections.

We then calculated the energy loss in the atmosphere. For each $Z \geq 26$, we calculated the mean atmospheric overburden by creating a histogram and filling it with the overburden for each event, which depends on the pressure from the SIP (in mbars) and the secant of the incidence angle. We then used this overburden as the thickness of the "air" slab to correct

for energy loss in the atmosphere. The calculated energies at the top of the atmosphere can be found in Table 5.5.

Top of Atmosphere Energies

Z		n=1.04 threshold cut MeV/nucleon	n=1.025 threshold cut MeV/nucleon	Low Energy threshold cut MeV/nucleon	Below C0 cutoff MeV/nucleon
26	Fe	2918	3833	661	2337
27	Co	2929	3845	677	2353
28	Ni	2932	3850	683	2361
29	Cu	2937	3856	692	2370
30	Zn	2938	3858	694	2375
31	Ga	2939	3859	696	2377
32	Ge	2940	3862	699	2383
33	As	2962	3884	725	2411
34	Se	2938	3861	697	2385
35	Br	2948	3871	710	2401
36	Kr	2945	3869	708	2400
37	Rb	2964	3889	730	2426
38	Sr	2965	3890	731	2429
39	Y	2963	3889	729	2431
40	Zr	2971	3897	740	2442

Table 5.5: Values of the various energy cuts at the top of the atmosphere for each Z.

5.2.3 Energy Correction Factors

The top of atmosphere energies can be used to make a correction to the abundances for the fact that we are not sampling the same energy range for each Z. To do this, we assume that for $Z \geq 26$ all elements have the same energy spectrum as $_{26}$Fe. Using a $_{26}$Fe spectrum from ACE/CRIS and HEAO C-3 provided by Kelly Lave (Lave et al., 2013), we can compute the integral fluxes for each Z between the limits given in Table 5.5. For the Below C0 data, we integrated between the low-energy cut and the Below C0 cutoff energy. For the Above C0 data, we integrated between the two C0 threshold energy values and infinity, and then took a weighted average of these fluxes. We interpolated between $_{26}$Fe energy spectra from

Bartels' Rotation	Start Date (UTC)	End date (UTC)	ϕ for $_{26}$Fe (MV)
2447	December 2, 2012	December 28, 2012	575
2448	December 29, 2012	January 24, 2013	535
2449	January 25, 2013	February 20, 2013	515

Table 5.6: Solar modulation parameter ϕ values measured for $_{26}$Fe by ACE/CRIS during the SuperTIGER flight. These values were provided by Mark Wiedenbeck of the Jet Propulsion Laboratory (priv. comm) and calculated using the method described in Wiedenbeck et al. (2005).

solar maximum (modulation parameter ϕ=900 MV) and solar minimum (ϕ=325 MV) to the average flight value of ϕ=543 MV for $_{26}$Fe. This flight value was calculated using the ϕ values for $_{26}$Fe for each Bartels cycle during the SuperTIGER flight, weighted by the number of days of data in each cycle. The in-flight ϕ values for $_{26}$Fe were measured by ACE/CRIS and the numbers were provided by Mark Wiedenbeck of the Jet Propulsion Laboratory (priv. comm). These in-flight ϕ values can be found in Table 5.6. These fluxes are normalized to $_{28}$Ni to find the energy correction factors. The atmospheric propagation code discussed in Section 5.3 requires these energy correction factors normalized to $_{28}$Ni, so $_{26}$Fe was not used for the normalization.

We also calculated the average energies at the top of the atmosphere for $_{26}$Fe in each energy range. These were calculated by integrating the $_{26}$Fe flux multiplied by the energy between the energy limits, and then dividing that by the integral of the flux in that range. For the Above C0 dataset, the average energy was 8295 MeV/nucleon, while it was 1313 MeV/nucleon for the Below C0 events and 1587 MeV/nucleon for the combined events.

5.3 Correction for Interactions in the Atmosphere

The correction for nuclear interactions that occurred within the atmosphere involves accounting for losses and additions to the flux of each element as it travels through the

Z		Combined Corr. Factor Ni=1	Below Corr. Factor Ni=1	Above Corr. Factor Ni=1
26	Fe	0.9740	0.9944	0.9656
27	Co	0.9907	0.9987	0.9873
28	Ni	1.0000	1.0000	1.0000
29	Cu	1.0076	1.0021	1.0099
30	Zn	1.0114	1.0024	1.0152
31	Ga	1.0129	1.0027	1.0173
32	Ge	1.0168	1.0034	1.0226
33	As	1.0441	1.0120	1.0585
34	Se	1.0159	1.0025	1.0217
35	Br	1.0299	1.0066	1.0402
36	Kr	1.0278	1.0055	1.0376
37	Rb	1.0528	1.0129	1.0708
38	Sr	1.0546	1.0132	1.0733
39	Y	1.0550	1.0126	1.0741
40	Zr	1.0641	1.0158	1.0861

Table 5.7: Energy Correction Factors for the SuperTIGER data. These were calculated based on integrals of the $_{26}$Fe flux from Lave et al. (2013) between the energy intervals in Table 5.5.

atmosphere. For the SuperTIGER atmospheric correction, we used the technique and code developed by Rauch (2008) for the TIGER analysis. This technique starts with an assumed top-of-atmosphere relative abundance for each element based on satellite measurements by HEAO-3-C2 (Byrnak et al., 1983), and HEAO-3-C3 and Ariel (Binns et al., 1989b). The change in abundances is then calculated in 1000 small steps through the entire atmospheric depth (provided as an input parameter). The process uses energy-dependent partial charge changing cross-sections from Nilsen et al. (1995), so the average energies calculated in Section 5.2.3 are used. Energy-independent total charge changing cross-sections from (Nilsen et al., 1995) are also used. The relative abundances for each element calculated at the end of these 1000 steps is then compared to the relative abundances at the top of the instrument. If the two abundances for a given element differ by more than 0.1%, an adjustment of half the magnitude of the difference is made in the top of atmosphere abundance. This process is repeated until the calculated abundance at the instrument and the top of instrument

abundances agree to within 0.1% for all charge species. The top-of-atmosphere numbers used for this final run are then reported as the top-of-atmosphere abundances. This propagation code was run by Brian Rauch of Washington University using inputs that I provided. More detail on this process can be found in Rauch (2008).

For the SuperTIGER data, the mean atmospheric depth used was calculated using the pressure data provided by the SIP. For each event, this pressure data was converted to g/cm^2 and then multiplied by the secant of the incidence angle to give the atmospheric overburden. We then used the mean overburden calculated for $_{26}$Fe events with a small addition for the material above the active area of the instrument. We calculated the areal density of this material and multiplied by the mean secant of the incidence angle observed during flight, which was 1.214. We then calculated the number of interaction lengths that this grammage represented and added an equivalent amount of air to the atmospheric overburden for the calculation. The mean atmospheric depth was 5.47 g/cm^2, and the material above the active area added the equivalent of 0.10 g/cm^2 of atmosphere, so the total overburden used for this calculation was 5.57 g/cm^2.

The energy correction factors calculated in Section 5.2.3 are then applied to correct the top-of-atmosphere abundances so that we are sampling the same energy range. Tables 5.8 and 5.9 show the energy-corrected Top-of-Atmosphere abundances obtained for the SuperTIGER data.

5.3.1 Determining the Uncertainties for Top-of-Atmosphere Abundances

To find the uncertainties for the Top-of-Atmosphere abundances, we made estimates of the systematic uncertainties in the propagation and of the propagated statistical uncertainties. The systematic uncertainties from the propagation arise from the uncertainties in the total

Z		**Above C0** Fe=1	combined low	errors high	statistical low	errors high	systematic low	errors high
26	Fe	1.00E+00	7.83E-04	7.83E-04	7.83E-04	7.83E-04	-	-
27	Co	1.63E-02	3.18E-04	3.18E-04	1.06E-04	1.06E-04	3.00E-04	3.00E-04
28	Ni	5.45E-02	1.93E-04	1.93E-04	1.85E-04	1.85E-04	5.18E-05	5.19E-05
29	Cu	9.91E-04	2.63E-05	2.63E-05	2.58E-05	2.58E-05	5.01E-06	5.00E-06
30	Zn	6.73E-04	2.15E-05	2.14E-05	2.14E-05	2.13E-05	2.24E-06	2.24E-06
31	Ga	5.15E-05	6.29E-06	6.95E-06	6.21E-06	6.88E-06	1.01E-06	9.79E-07
32	Ge	8.69E-05	7.96E-06	8.01E-06	7.93E-06	7.98E-06	7.04E-07	6.98E-07
33	As	1.21E-05	3.32E-06	4.12E-06	3.27E-06	4.07E-06	5.99E-07	5.98E-07
34	Se	4.16E-05	5.72E-06	6.47E-06	5.69E-06	6.46E-06	4.97E-07	4.93E-07
35	Br	1.28E-05	3.31E-06	4.13E-06	3.28E-06	4.11E-06	4.04E-07	3.98E-07
36	Kr	1.81E-05	3.88E-06	4.70E-06	3.86E-06	4.69E-06	3.64E-07	3.60E-07
37	Rb	6.66E-06	2.55E-06	3.43E-06	2.52E-06	3.41E-06	3.67E-07	3.64E-07
38	Sr	2.71E-05	4.70E-06	5.54E-06	4.69E-06	5.53E-06	3.44E-07	3.44E-07
39	Y	8.40E-06	2.71E-06	3.61E-06	2.70E-06	3.61E-06	2.29E-07	2.27E-07
40	Zr	1.12E-05	3.10E-06	4.00E-06	3.09E-06	4.00E-06	2.04E-07	2.03E-07
Z		**Below C0** Fe=1	combined low	errors high	statistical low	errors high	systematic low	errors high
26	Fe	1.00E+00	6.29E-04	6.29E-04	6.29E-04	6.29E-04	-	-
27	Co	1.42E-02	3.75E-04	3.75E-04	8.16E-05	8.16E-05	3.66E-04	3.66E-04
28	Ni	5.20E-02	1.54E-04	1.54E-04	1.48E-04	1.48E-04	4.35E-05	4.36E-05
29	Cu	9.01E-04	2.09E-05	2.09E-05	2.03E-05	2.03E-05	5.30E-06	5.28E-06
30	Zn	5.71E-04	1.63E-05	1.65E-05	1.61E-05	1.64E-05	1.99E-06	1.98E-06
31	Ga	4.14E-05	4.89E-06	4.86E-06	4.74E-06	4.72E-06	1.18E-06	1.18E-06
32	Ge	8.42E-05	6.55E-06	6.59E-06	6.50E-06	6.55E-06	7.60E-07	7.41E-07
33	As	8.98E-06	2.64E-06	3.18E-06	2.53E-06	3.09E-06	7.53E-07	7.41E-07
34	Se	4.01E-05	4.71E-06	5.21E-06	4.67E-06	5.19E-06	5.53E-07	5.44E-07
35	Br	6.03E-06	2.19E-06	2.77E-06	2.12E-06	2.72E-06	5.50E-07	5.37E-07
36	Kr	2.41E-05	3.78E-06	4.35E-06	3.75E-06	4.33E-06	4.70E-07	4.63E-07
37	Rb	6.38E-06	2.28E-06	2.88E-06	2.22E-06	2.84E-06	5.08E-07	5.02E-07
38	Sr	3.69E-05	4.66E-06	5.28E-06	4.64E-06	5.27E-06	4.25E-07	4.31E-07
39	Y	6.21E-06	2.07E-06	2.72E-06	2.05E-06	2.71E-06	2.58E-07	2.54E-07
40	Zr	1.03E-05	2.58E-06	3.24E-06	2.57E-06	3.23E-06	2.26E-07	2.23E-07

Table 5.8: Top of Atmosphere Abundances for the Above and Below C0 datasets.

Z		**Combined** Fe=1	combined low	errors high	statistical low	errors high	systematic low	errors high
26	Fe	1.00E+00	6.85E-04	6.85E-04	6.85E-04	6.85E-04	-	-
27	Co	1.49E-02	3.68E-04	3.68E-04	9.14E-05	9.14E-05	3.57E-04	3.57E-04
28	Ni	5.30E-02	1.73E-04	1.73E-04	1.66E-04	1.66E-04	4.93E-05	4.93E-05
29	Cu	9.36E-04	2.30E-05	2.30E-05	2.24E-05	2.24E-05	5.41E-06	5.39E-06
30	Zn	6.11E-04	1.82E-05	1.82E-05	1.80E-05	1.80E-05	2.12E-06	2.12E-06
31	Ga	4.51E-05	4.74E-06	5.69E-06	4.60E-06	5.57E-06	1.15E-06	1.13E-06
32	Ge	8.53E-05	7.10E-06	7.15E-06	7.06E-06	7.11E-06	7.57E-07	7.73E-07
33	As	1.01E-05	2.91E-06	3.56E-06	2.82E-06	3.49E-06	7.25E-07	7.07E-07
34	Se	4.07E-05	4.95E-06	5.72E-06	4.92E-06	5.69E-06	5.45E-07	5.37E-07
35	Br	8.56E-06	2.63E-06	3.29E-06	2.58E-06	3.25E-06	5.07E-07	4.98E-07
36	Kr	2.18E-05	4.06E-06	4.50E-06	4.03E-06	4.47E-06	4.41E-07	4.35E-07
37	Rb	6.46E-06	2.40E-06	3.11E-06	2.36E-06	3.07E-06	4.68E-07	4.63E-07
38	Sr	3.33E-05	5.10E-06	5.42E-06	5.09E-06	5.40E-06	3.93E-07	4.04E-07
39	Y	7.05E-06	2.33E-06	3.09E-06	2.32E-06	3.07E-06	2.55E-07	2.52E-07
40	Zr	1.07E-05	2.79E-06	3.56E-06	2.78E-06	3.56E-06	2.20E-07	2.21E-07

Table 5.9: Top of Atmosphere Abundances for the combined dataset.

and partial charge changing cross sections. Nilsen et al. (1995) give an uncertainty of ±15% on these partial cross sections and ±10% on the total charge changing cross sections. To make a conservative estimate of the effect of these uncertainties, all of the the partial charge changing cross sections were all reduced by 20%, and then the propagation code was re-run. Then, these cross sections were increased to 20% more than their initial values and were re-run. This process was then repeated for all the total charge changing cross-sections, increasing and decreasing by 10% from their initial values and re-running the propagation code. The differences in the Top-of-Atmosphere abundances derived from these changed cross sections and their initial values are reported as the systematic uncertainties in the abundance for each Z in Table 5.8.

To propagate the statistical uncertainties from the Top-of-Instrument abundances to the top of the atmosphere, the Top-of-Instrument abundances were varied individually. For each Z, the Top-of-Instrument abundance was first increased to its likely upper value given its Top-of-Instrument statistical uncertainty, and the propagation code was re-run. Then,

		Combined	errors	
Z		Fe=1	low	high
26	Fe	1.00E+00	6.85E-04	6.85E-04
27	Co	8.09E-03	2.00E-04	2.00E-04
28	Ni	5.53E-02	1.81E-04	1.81E-04
29	Cu	9.19E-04	2.26E-05	2.26E-05
30	Zn	6.40E-04	1.90E-05	1.90E-05
31	Ga	4.26E-05	5.13E-06	5.38E-06
32	Ge	7.01E-05	5.83E-06	5.87E-06
33	As	-	-	-
34	Se	4.32E-05	5.41E-06	6.06E-06
35	Br	6.50E-06	2.00E-06	2.50E-06
36	Kr	1.49E-05	2.62E-06	3.08E-06
37	Rb	6.99E-06	2.60E-06	3.37E-06
38	Sr	4.10E-05	5.77E-06	6.68E-06
39	Y	7.14E-06	2.36E-06	3.12E-06
40	Zr	1.07E-05	2.80E-06	3.57E-06

Table 5.10: SuperTIGER Galactic Cosmic Ray Source abundances calculated using the TIGER propagation.

the Top-of-Instrument abundance was decreased to its lowest likely value given its Top-of-Instrument statistical uncertainty and the code was run another time. The abundances of all other Zs were kept constant. The differences in the Top-of-Atmosphere abundances derived from these modified Top-of-Instrument abundances and the initial Top-of-Atmosphere value are reported as the statistical uncertainties in the abundance for each Z in Tables 5.8 and 5.9. For $_{26}$Fe and $_{28}$Ni, which are mostly primary cosmic rays, the fractional uncertainties for the Top-of-Instrument abundances were used to calculate the uncertainties of the Top-of-Atmosphere abundances. The statistical and systematic uncertainties are then added in quadrature to give the total uncertainties in Tables 5.8 and 5.9.

5.4 Galactic Cosmic Ray Source Abundances

The SuperTIGER Galactic Cosmic Ray Source (GCRS) abundances were calculated using the galactic propagation done for the TIGER data in Rauch et al. (2009). This calculation was done by Mark Wiedenbeck of the Jet Propulsion Laboratory using a "leaky box" propagation model (described in Wiedenbeck et al. (2007)). This model included fragmentation loss and production, radioactive decay, ionization loss, and escape from the galaxy using the same parameters that were used for the TIGER data analysis. In addition, partial cross sections based on Silverberg et al. (1998) and total destruction cross sections derived from Webber et al. (1990) were used.

This model starts by assuming a set of source isotopic abundances for the GCR source, in this case Solar System abundances from Lodders (2003), with an energy spectrum of the form from Davis et al. (2000). The propagation of each element is then modeled individually. These interstellar propagation results are then used as the input to a spherically symmetric "Fisk Model" calculation of the solar modulation. The elemental abundances are then calculated by summing the isotope spectra and extracting the abundance at the median energy of the dataset. The propagated and modulated abundances are then compared to the Top-of-Atmosphere relative abundances. The GCR source relative abundances are then adjusted until the propagated and modulated abundances match the observed Top-of-Atmosphere relative abundances. The GCRS relative abundances are assumed to have the same fractional uncertainties as the Top-of-Atmosphere relative abundances. For $Z \leq 38$, we used the propagation from Rauch et al. (2009). For $_{39}$Y and $_{40}$Zr, we used a propagation calculation done using the same method for a SuperTIGER funding proposal in 2013 that propagated hypothetical GCRS abundances. Rauch et al. (2009) did not obtain a GCRS abundance for $_{33}$As, which is almost entirely secondary, so we do not report a SuperTIGER GCRS abundance.

Table 5.10 shows the SuperTIGER GCRS relative abundances along with associated errors. These abundances will be compared with other experiments and models of GCR origin and acceleration in the following chapter.

Chapter 6

Science Results

The SuperTIGER Top-of-Atmosphere and Galactic Cosmic Ray Source (GCRS) relative abundances derived in Chapter 5 can be directly compared to elemental abundances reported by previous experiments. In this chapter, we make these comparisons and then compare the SuperTIGER results to various models of the GCR source. We compare the SuperTIGER GCR source abundances to various models of GCR source composition and acceleration fractionation. As was seen in TIGER (Rauch et al., 2009), preferential acceleration is seen for refractory elements, found in interstellar dust grains, over volatile elements, which are primarily in a gaseous state. The SuperTIGER results support the OB association/superbubble model for GCR origins, with a mixture of mostly material with solar system abundances enriched by a small component from massive stars as the GCR source.

6.1 Comparison of SuperTIGER Top of Atmosphere Abundances with Previous Data

Figure 6.1 shows the SuperTIGER Top-of-Atmosphere data compared to GCR relative abundances observed in space near Earth by HEAO-3-C2 and ACE-CRIS, and compared to

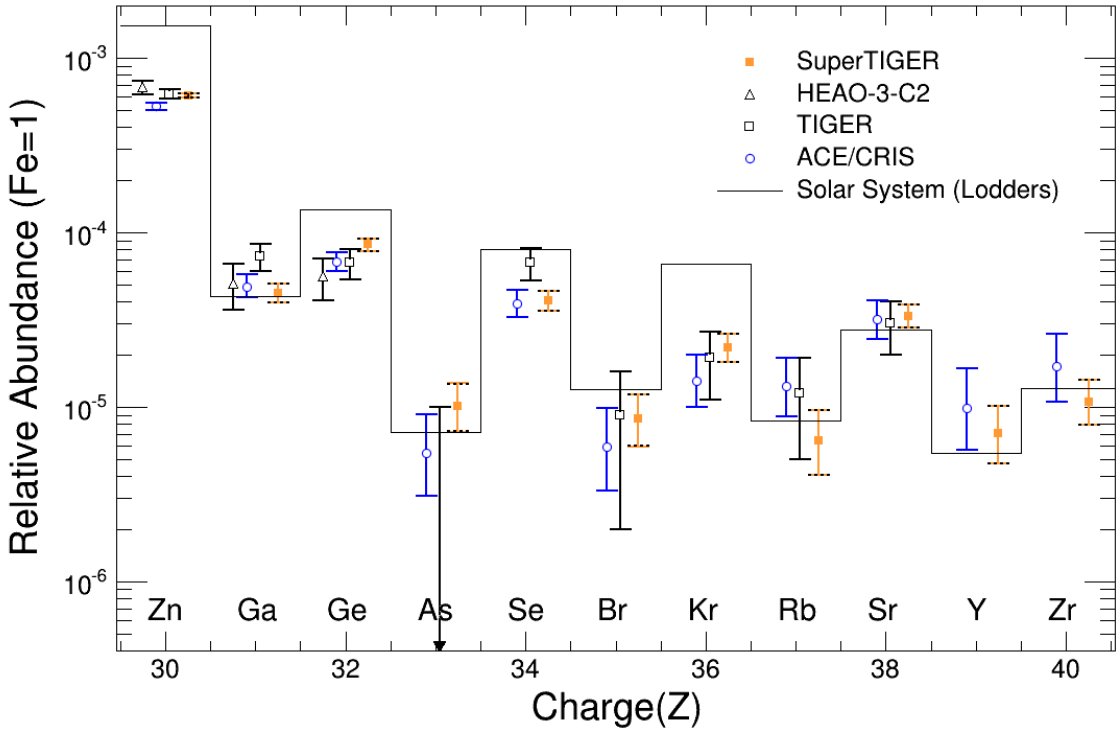

Figure 6.1: Comparison of SuperTIGER Top-of-Atmosphere abundances with space abundances from ACE-CRIS (Binns et al., 2013) and HEAO-3-C2 (Byrnak et al., 1983), and Top-of-Atmosphere abundances from TIGER (Rauch et al., 2009). For the SuperTIGER points, combined statistical and systematic errors are shown as orange error bars, and statistical-only error bars shown as black dashed lines. The statistical-only uncertainties are barely distinguishable from the combined statistical and systematic uncertainties.

GCR Top-of-Atmosphere relative abundances from TIGER, and Solar System abundances from Lodders et al. (2009). For the SuperTIGER points, the combined statistical and systematic error bars are shown in solid orange, while the statistical-only error bars are shown as dashed black lines. The statistical errors dominate the total error, and for the most part the systematic uncertainties are negligible. The ACE-CRIS error bars are purely statistical, while the TIGER error bars are Top-of-Instrument statistical uncertainties propagated through the atmosphere(using the same method as described in Chapter 5). The HEAO-3-C2 error bars are those reported in Byrnak et al. (1983).

The SuperTIGER data points generally agree with previous experiments, but with significantly smaller error bars. Where SuperTIGER and TIGER Top-of-Atmosphere relative abundances differ, SuperTIGER agrees with data from ACE-CRIS. Of particular note are $_{31}$Ga and $_{32}$Ge. TIGER measurements showed nearly equal abundances for these two elements, while SuperTIGER shows a lower abundance for $_{31}$Ga and a higher abundance for $_{32}$Ge. This impacts the amount of Massive Star Outflow (MSO) required when modeling the GCRS source mixture, as we will see in Section 6.3.1.

6.2 Comparison of SuperTIGER GCRS Results with FIP Acceleration Model

An early model of GCR acceleration, discussed in Section 1.2.1, suggested that the GCR source is material from the coronae of ordinary stars. This coronal material would then be injected into the space around the star by stellar winds and flare events before being accelerated by a nearby supernova explosion. This would result in an overabundance in the GCR relative to Solar System abundances of elements with lower First Ionization Potential (FIP). Figure 6.2 shows GCR source abundances divided by Solar System abundances from Lodders (2003). Wherever possible, SuperTIGER GCRS numbers are used. For lower-Z elements GCRS relative abundances from HEAO-3-C2 (Engelmann et al., 1990) are used, and TIGER GCRS relative abundances from Rauch et al. (2009) were used for $_{27}$Co and $_{29}$Cu. While there is a general mass-dependent trend, elements such as $_{32}$Ge and $_{27}$Co have nearly the same FIP but dramatically different GCRS/SS ratios. FIP does not not appear to adequately explain the SuperTIGER data.

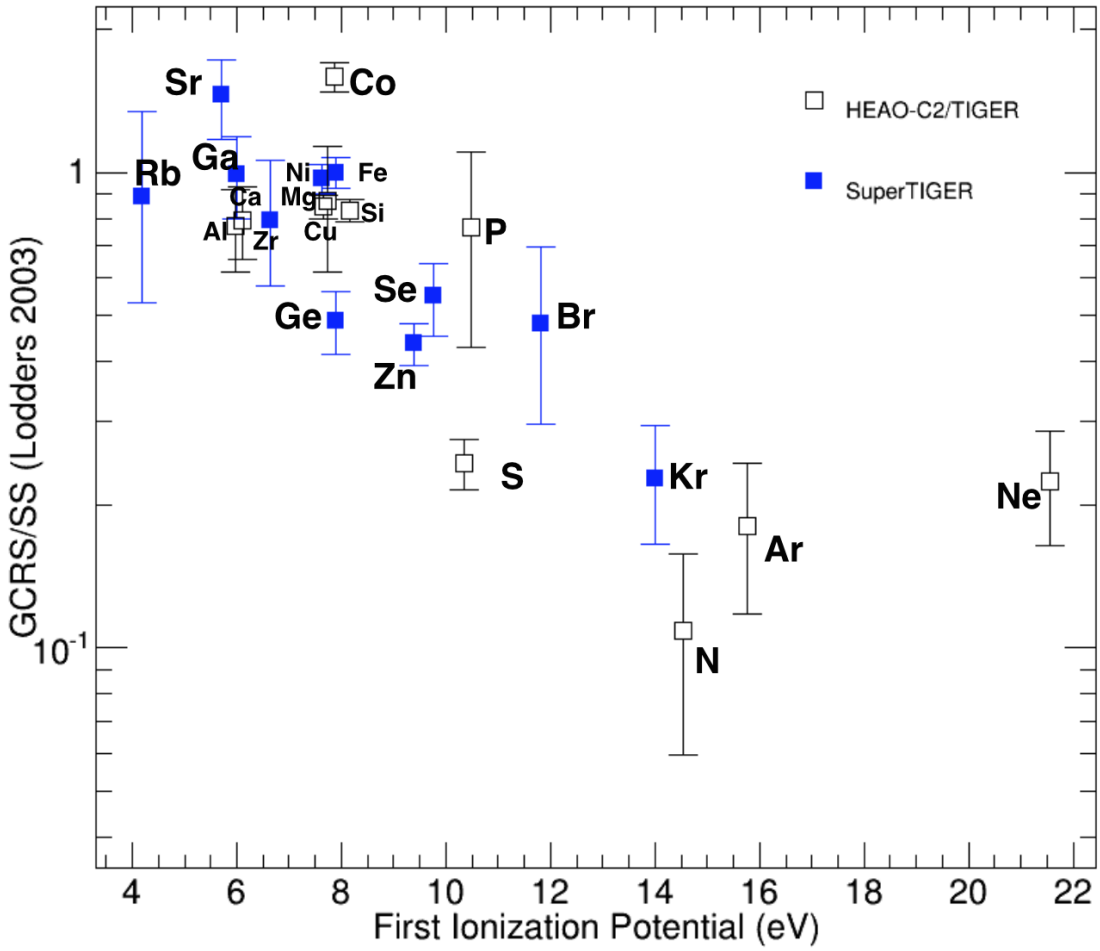

Figure 6.2: Ratio of SuperTIGER, TIGER (for $_{27}$Co and $_{29}$Cu only), and HEAO-3-C2 GCRS relative abundances with SS relative abundances from Lodders (2003), plotted as a function of First Ionization Potential (FIP).

6.3 Comparison of SuperTIGER GCRS Results with OB Association Model

Figure 6.3 shows the ratio of SuperTIGER, TIGER, and HEAO-3-C2 GCRS relative abundances divided by Solar System abundances from Lodders et al. (2009) plotted as a function of atomic mass A. Elements were classified as refractory or volatile based on their equilibrium 50% condensation temperatures from Lodders (2003). Elements with $T_C >\sim$ 1200 K were classified as refractory, and elements with lower condensation temperatures

were classified as volatile. A separation between the two was predicted by Meyer et al. (1997), as discussed in Chapter 1. As with the TIGER data shown in Figure 1.3, at high A there is less separation between refractory and volatile elements. This remains true if we use other models of Solar System abundances (described below), as seen in Figures 6.4 and 6.5. On TIGER, adding in ∼20% massive star outflow (MSO) from Woosley and Heger (2007) resolved this, providing a clear separation between the refractory and volatile elements. For SuperTIGER, we tested our GCRS source abundances against various source models to find the model that fit best.

6.3.1 Calculating the GCRS Composition Source Mixture

We can compare the calculated SuperTIGER GCRS relative abundances to various source mixtures. These mixtures use Solar System relative elemental abundances and mix in material from the outflow of massive stars from Woosley and Heger (2007). Woosley and Heger give results for total elemental yields of massive stars, integrated over a Salpeter Initial Mass Function (with $\Gamma = -1.35$) for solar metallicity stars from 12 $M_\odot$ to 120 $M_\odot$. Figure 6.6 shows these production factors relative to SS abundances. These production factors are the same that were used for the TIGER analysis by Rauch (2008) and Rauch et al. (2009). We used 3 different sets of SS relative abundances—those from Lodders (2003), Lodders, Palme, and Gail (2009), and a third table, which was calculated based on the work of Grevesse et al. (2010) and Asplund et al. (2009) according to a method given by Nicolas Grevesse to W. Robert Binns of Washington University (priv. comm.).

The GCRS source models were calculated using the production factors from Woosley and Heger (2007), SS abundances, and a mix fraction η_{WH}, representing the proportion of the mix that came from massive star outflow. For element X, the mix is given by:

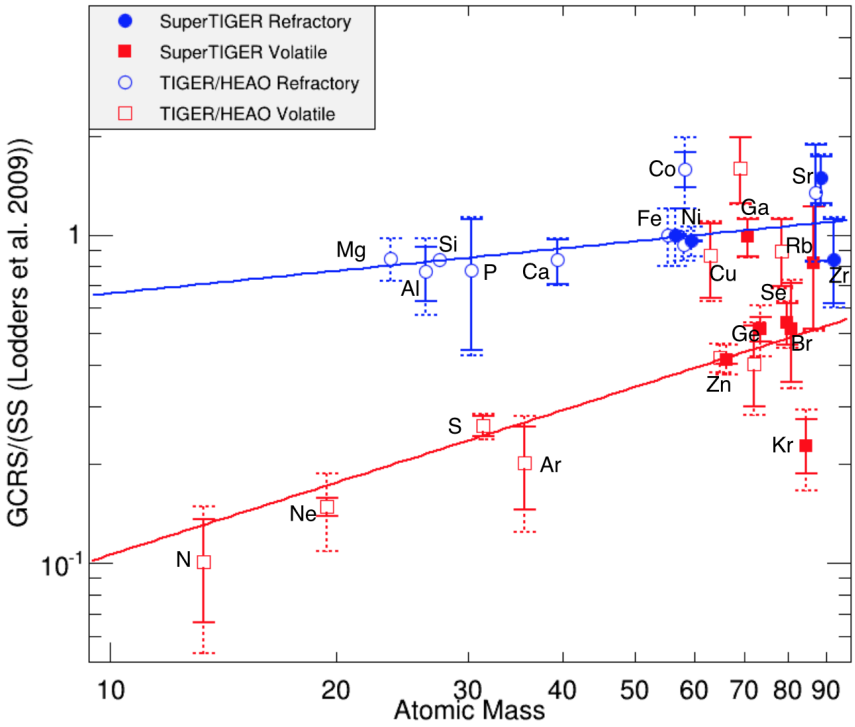

Figure 6.3: Ratio of GCRS relative abundances with Solar System relative abundances from Lodders et al. (2009). Solid error bar lines are uncertainties in GCRS abundances, dashed error bar lines represent total uncertainty in the GCRS/SS ratio. Fit lines for the Refractory (in blue) and Volatile (in red) elements are shown.

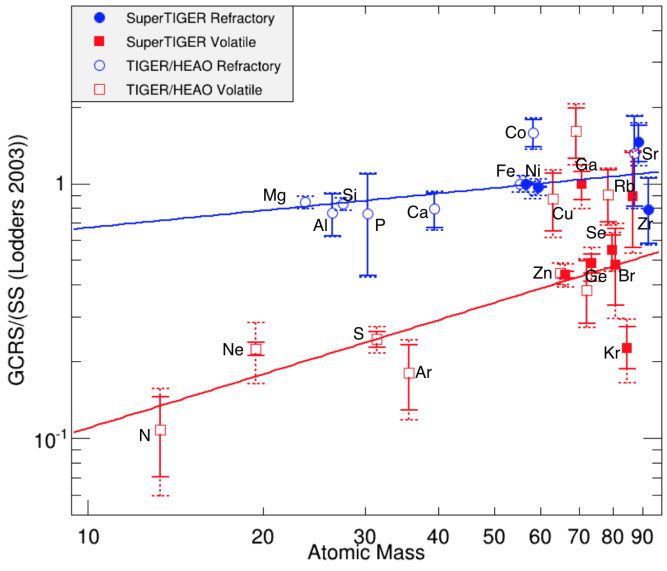

Figure 6.4: Ratio of GCRS relative abundances with Solar System relative abundances from Lodders (2003). Solid error bar lines are uncertainties in GCRS abundances, dashed error bar lines represent total uncertainty in the GCRS/SS ratio. Fit lines for the Refractory (in blue) and Volatile (in red) elements are shown.

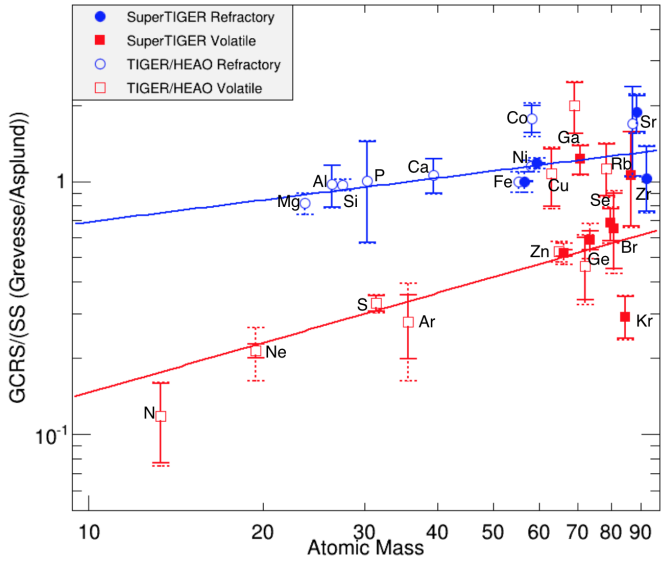

Figure 6.5: Ratio of GCRS relative abundances with Solar System relative abundances from Grevesse et al. (2010)/Asplund et al. (2009). Solid error bar lines are uncertainties in GCRS abundances, dashed error bar lines represent total uncertainty in the GCRS/SS ratio. Fit lines for the Refractory (in blue) and Volatile (in red) elements are shown.

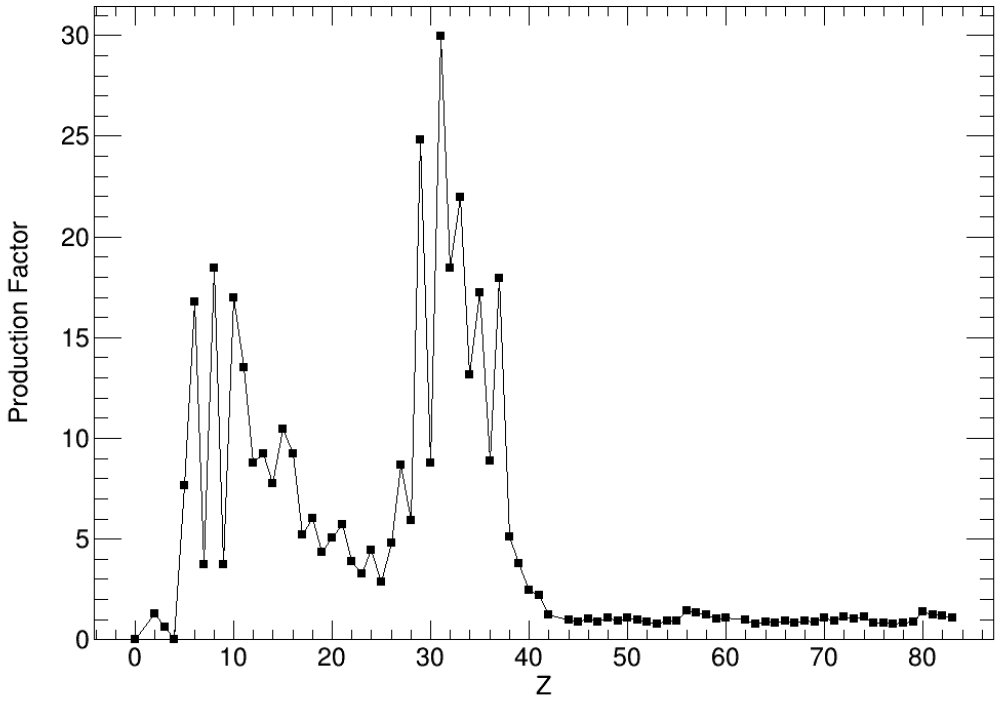

Figure 6.6: Production factors relative to SS Abundances for massive star nucleosynthesis, derived from Figure 7 in Woosley and Heger (2007), compiled in Table 6.1 of Rauch (2008).

$$GCRS(X) = \frac{(PF_M(X)\eta_{WH} + (1 - \eta_{WH}))\, N_{SS}(X)}{(PF_M(Fe)\eta_{WH} + (1 - \eta_{WH}))\, N_{SS}(Fe)}. \tag{6.1}$$

Here, $PF_M(X)$ is the mass production factor from Woosley and Heger (2007), and N_{SS} is the relative number SS abundance. We calculated GCRS mixtures in 1% increments from 100% SS abundances to 100% massive star outflow. For each mixture, we plotted the ratio of the GCRS Abundances (from SuperTIGER, TIGER, and HEAO-3-C2) to the GCRS model against atomic mass. We include uncertainties in the ratio that are the sum in quadrature of the uncertainties in GCRS abundances (summed statistical and systematic error bars for SuperTIGER, reported error bars for TIGER and HEAO-3-C2) and the uncertainty in the Solar System abundance. We assumed that the production factor for each Z had the same fractional uncertainties as the solar system abundance. The atomic masses we used were

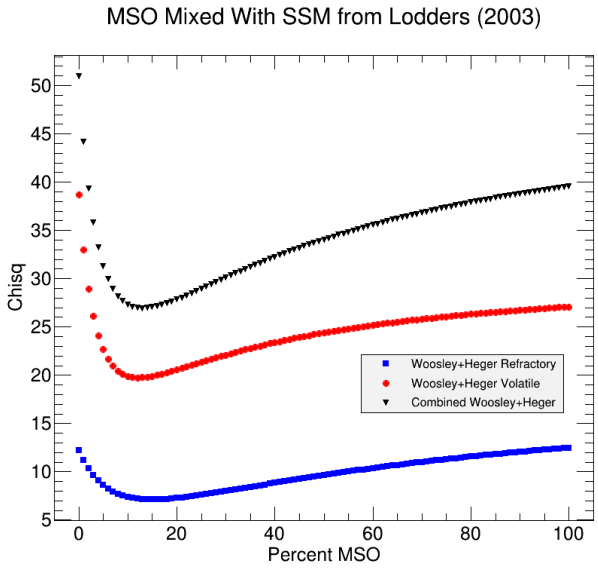

Figure 6.7: Summed Chi Squared as function of MSO contribution to the source mixture.

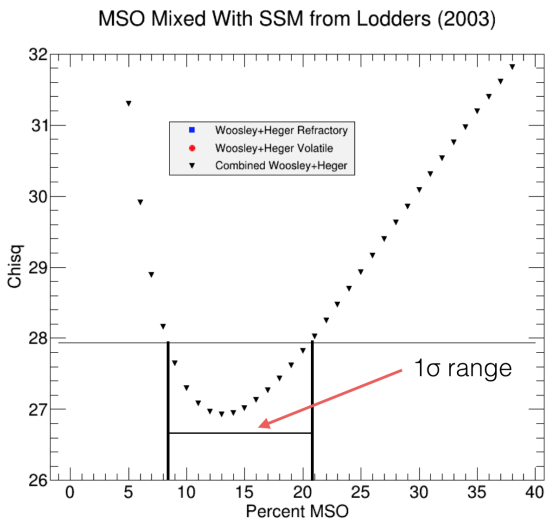

Figure 6.8: Summed Chi squared with expanded vertical and horizontal scale, showing the 1-σ range used to report uncertainties in the optimal source mixture.

based on SS isotopic mass fractions from Lodders et al. (2009). We made separate plots for refractory and volatile elements, and then fit each these with a curve of the form $y = C_0 A^{C_1}$.

. For each fit, we then calculated the summed χ^2 value, and then plotted the summed χ^2 as a function of MSO percentage. Figure 6.7 shows the plot of summed χ^2 for each GCRS mixture. The minimum of the combined Volatile and Refractory χ^2 values (χ^2_{min}) represents the best fit. We then found the 1-σ uncertainty levels by finding the mixtures with a χ^2 value of χ^2_{min}+1, shown in Figure 6.8. A plot showing the values of the fit slopes as a function of MSO percentage can be found in Figure 6.9. Example plots are shown in Figures 6.10-6.12.

We tested GCRS mixtures of MSO from Woosley and Heger (2007) and SS material from each of the three SS models with a combined SuperTIGER, TIGER, and HEAO dataset. For Z <26, we used HEAO-3-C2 GCRS abundances from Engelmann et al. (1990). For $_{27}$Co and $_{29}$Cu, we used just the TIGER measured GCRS abundances from Rauch et al. (2009). For all other elements with $26 \leq Z \leq 40$ (except for $_{33}$As and $_{39}$Y), we used a combination

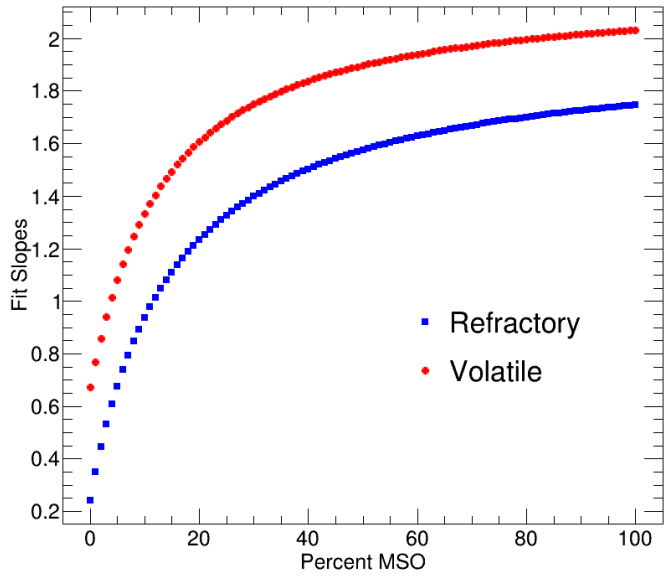

Figure 6.9: Slopes of the fits ($y = C_0 A^{C_1}$) for the refractory and volatile elements for each GCRS mixture.

of the TIGER and SuperTIGER abundances, weighted by the statistics recorded with each experiment.

SuperTIGER added new points to these plots, most of them for volatile elements. $_{35}$Br, $_{36}$Kr, and $_{37}$Rb were added to the volatile elements used, while $_{40}$Zr was added to the refractory elements. The uncertainties in the abundances of $_{34}$Se and $_{38}$Sr were also reduced, shrinking the error bars on the plot. These served to further constrain the mass-dependent trends for both types of elements.

Other Models of Massive Star Outflow

While the model described in Woosley and Heger (2007) was used for the TIGER data analysis and has been used by Lingenfelter and Higdon (2003), among others, as the default model for the elemental and isotopic yields of massive stars, a number of other groups have also modeled the elemental yields of supernovae. Chieffi and Limongi (2013), for example,

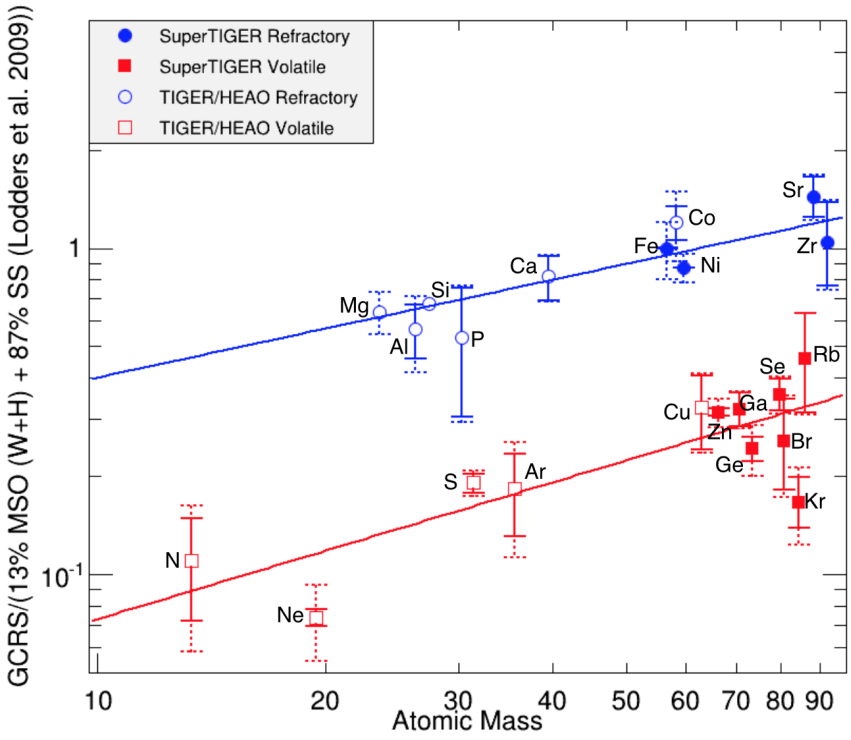

Figure 6.10: Ratio of GCRS relative abundances with SS relative abundances from Lodders et al. (2009) for the best-fit case for the combined SuperTIGER, TIGER, and HEAO method. Solid lines are uncertainties in GCRS abundances, dashed lines represent total uncertainty in the GCRS/SS ratio.

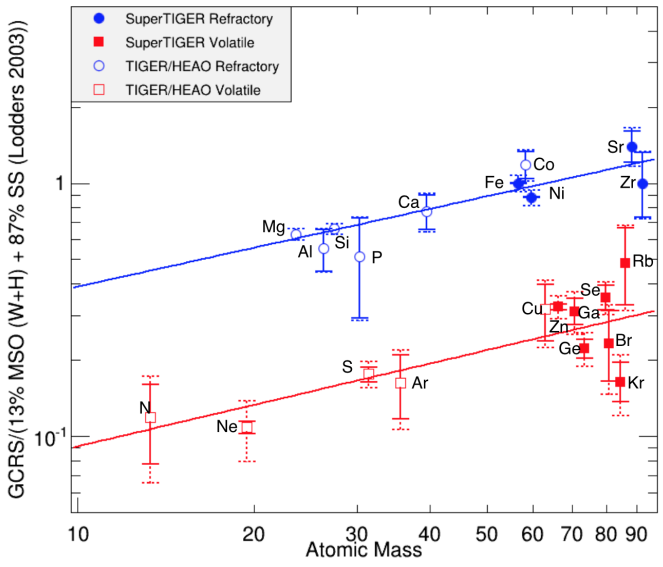

Figure 6.11: Ratio of GCRS relative abundances with SS relative abundances from Lodders (2003) for the best-fit case for the combined SuperTIGER, TIGER, and HEAO method. Solid lines are uncertainties in GCRS abundances, dashed lines represent total uncertainty in the GCRS/SS ratio.

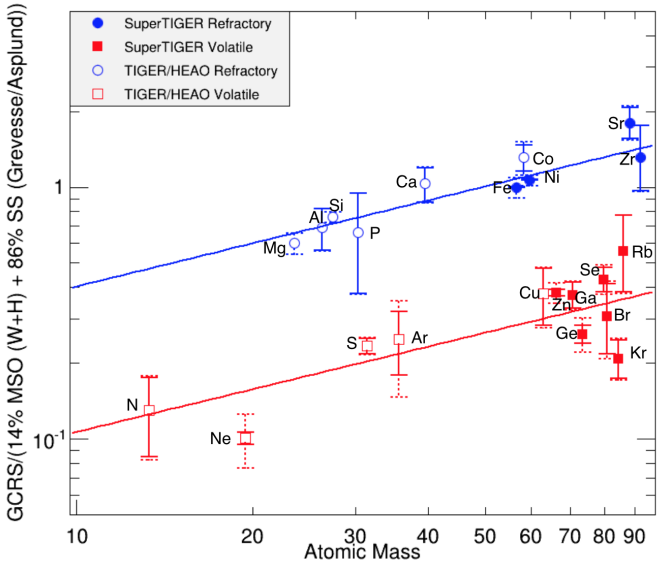

Figure 6.12: Ratio of GCRS relative abundances with SS relative abundances from Grevesse et al. (2010)/Asplund et al. (2009) for the best-fit case for the combined SuperTIGER, TIGER, and HEAO method. Solid lines are uncertainties in GCRS abundances, dashed lines represent total uncertainty in the GCRS/SS ratio.

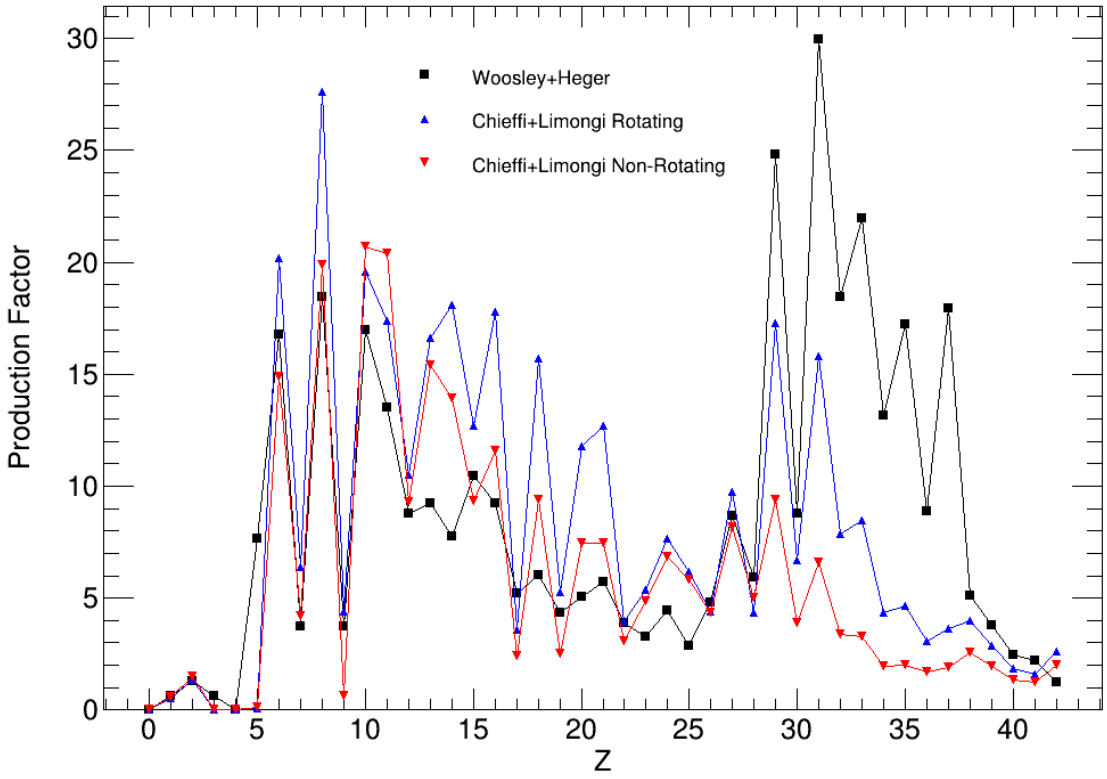

Figure 6.13: Production factors from Woosley and Heger (2007) compared to two sets of production factors from Chieffi and Limongi (2013).

published elemental production factors that are dramatically different than those published by Woosley and Heger (2007). Figure 6.13 shows a comparison between the production factors from Woosley and Heger (2007) and two different models from Chieffi and Limongi (2013), for rotating (v=300m/s) and non-rotating (v=0m/s) stars. In particular, elements in the range $30 \leq Z \leq 40$ are produced in significantly lower quantities under both Chieffi and Limongi models. For the source mixes discussed here, however, the Chieffi and Limongi models were not considered.

6.3.2 GCRS Mix Results and Comparison with Previous Data

While Rauch et al. (2009) reported results consistent with a ∼20% MSO mix fraction, a similar analysis of the TIGER data to find an optimal source mixture was presented by W. Robert Binns of Washington University at the 2010 COSPAR Scientific Assembly, using SS abundance from Lodders (2003). This analysis reported a MSO mix fraction of 14^{+8}_{-5}%. Using data from the ACE-CRIS experiment, Kelly Lave of Washington University derived a MSO mix fraction of 8^{+11}_{-4}%. This analysis, in a 2013 internal ACE memo, used SS abundances from Lodders et al. (2009). Both of these analyses used the MSO production factors from Woosley and Heger (2007).

The best-fit mixtures found using HEAO data points with combined SuperTIGER and TIGER data points are shown in Figures 6.10-6.12 for abundances from Lodders et al. (2009), Lodders (2003), and Grevesse et al. (2010)/Asplund et al. (2009), respectively. For mixes with Lodders et al. (2009), the best fit mixture has a MSO mix fraction of 12^{+6}_{-5}%, with a reduced χ^2 value of 1.67. For Lodders (2003) it is 13^{+8}_{-5}%, with a reduced χ^2 value of 1.50. Using Grevesse et al. (2010)/Asplund et al. (2009) gives an optimal mixture of 14^{+7}_{-5}%, with a reduced χ^2 value of 2.22.

While these three calculations agree to within the calculated uncertainties, the mixture with 13% MSO and 87% material with SS abundances from Lodders (2003) provides the best fit, with a reduced χ^2 value of 1.50. This 13% MSO value is the midpoint between the MSO fractions given by the best fits to the other two SS models, so our best-fit GCRS mixture consists of ∼13% MSO and ∼87% material with SS abundances.

All of these mixtures found mass-dependent trends for both the volatile and refractory elements. The volatile mass dependent-trend was predicted by Ellison et al. (1997), but no such trend was predicted for refractory elements. TIGER analysis from Rauch et al.

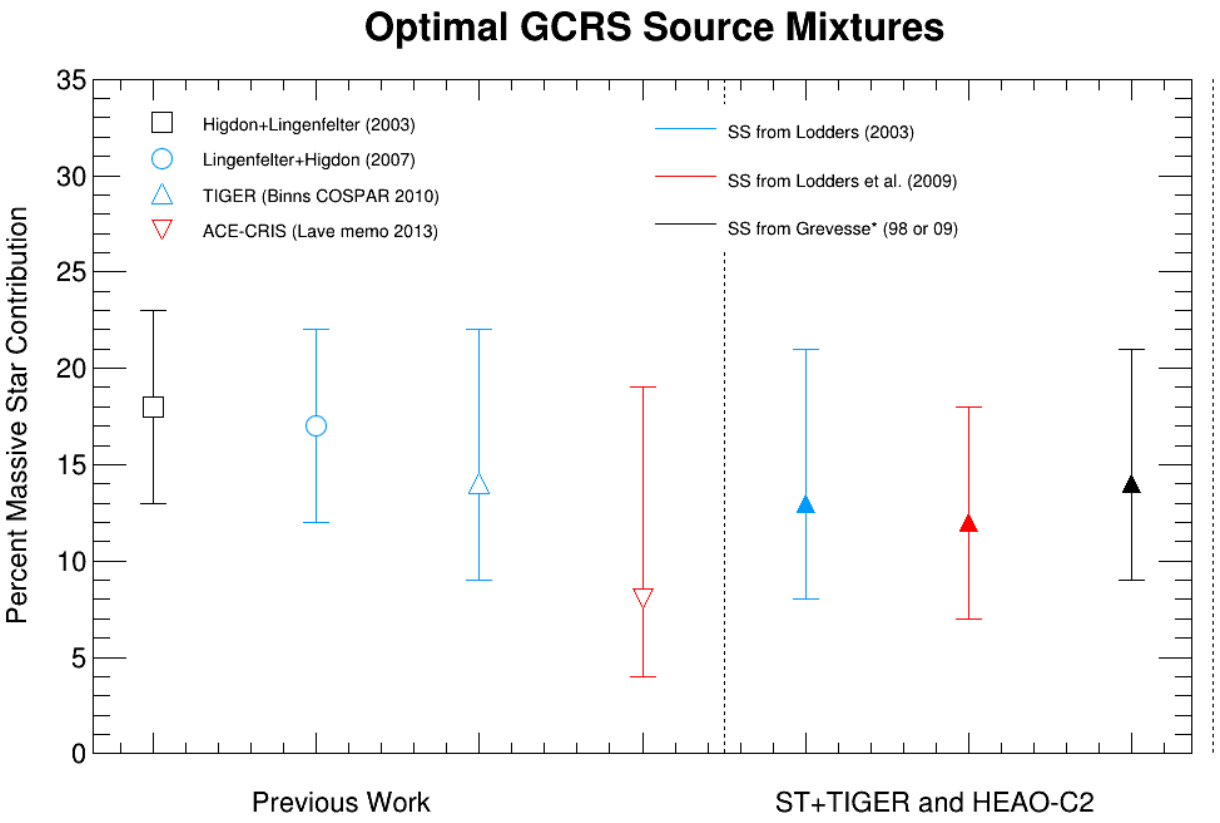

Figure 6.14: Comparison of GCRS MSO % from various measurements. Higdon and Lingenfelter (2003) used SS abundances from Anders and Grevesse (1989) mixed with MSO numbers based on Woosley and Weaver (1995). All of the other measurements used MSO production factors from Woosley and Heger (2007) and SS abundances as indicated.

(2009) was inconclusive, as the $_{38}$Sr point had large statistical uncertainties associated with it. The SuperTIGER $_{38}$Sr relative abundance is higher than that found on TIGER and has a smaller statistical uncertainty, but the two measurements still agree to within statistical uncertainties. This is further evidence for a mass-dependent trend. $_{40}$Zr, another refractory element, lies below the refractory trend line in Figures 6.10-6.12. This new SuperTIGER data point still has large associated uncertainty, and further data will be needed to improve this.

Figure 6.14 shows how these calculated optimal mixtures for SuperTIGER compare with other measurements. The measurement from Higdon and Lingenfelter (2003) was based

on the observed ACE-CRIS $^{22}Ne/^{20}Ne$ ratio, and used SS abundances from Anders and Grevesse (1989) mixed with MSO numbers based on Woosley and Weaver (1995). All of the other measurements used MSO production factors from Woosley and Heger (2007). The Lingenfelter and Higdon (2003) point used SS abundances from Lodders (2003). The SS sources for the Binns 2010 point and the Lave 2013 point were described above.

The SuperTIGER best-fit GCRS mixture, with a MSO mass fraction of $13^{+8}_{-5}\%$ and SS abundances from Lodders (2003), is consistent with previous results. This mixture is towards the low end of the range calculated by Higdon and Lingenfelter (2003) and Lingenfelter and Higdon (2003), but is similar to the number calculated for the TIGER dataset for the 2010 Binns COSPAR talk. This lends further support to the OB Association model for the origin and acceleration of GCR.

6.4 Conclusion

The SuperTIGER instrument was developed to make precise measurements of the relative abundances of the ultra-heavy Galactic Cosmic Rays with single-element resolution and high statistics. In its record-breaking 55-day balloon flight, the instrument successfully detected and telemetered over 4 million $_{26}Fe$ events and over 600 events in the charge range $30 < Z \leq 40$. These measurements are the best measurements ever performed for the GCR in the charge range $30 \leq Z \leq 40$, and the first to individually resolve every element in that range with good statistics.

The measured abundances, corrected for propagation affects to the top of the atmosphere, are consistent with previous measurements. The abundances corrected for propagation effects to the GCR source are consistent with previous measurements and support the OB Association theory of GCR origins, where the GCR source is composed of mostly material

with solar system abundances enriched by a small contribution from material from massive stars. This mixture is then accelerated by supernova explosions, most of which occur in O and B type stars in OB associations. The SuperTIGER data support a best-fit GCR source mixture of $\sim$87% normal ISM with a 13^{+8}_{-5}% enrichment by mass from massive star outflow. These data allowed for the inclusion of four new elements into the GCR source analysis. The SuperTIGER data show a preferential acceleration of refractory elements, primarily found in interstellar dust grains, over volatile elements, which are mostly found in a gaseous state. This preferential acceleration shows a mass-dependent trend for both the volatile elements, which is predicted by Ellison, Drury, and Meyer (1997), and the refractory elements, which is not. Better resolving the abundances for ultra-heavy elements would help provide a further test of the OB association theory of GCR origins. This improvement can be achieved through increased exposure time, either on the planned SuperTIGER-II Antarctic balloon flight in 2017 or by a potential space-based mission dedicated to measuring the flux of ultra-heavy galactic cosmic rays.

Appendix A

Calibration and Performance of the Scintillating Fiber Hodoscope

The SuperTIGER scintillating fiber hodoscope was used to measure the trajectory of cosmic-ray particles as they passed through the instrument. This appendix describes the work that went into corrections for position variation of the fibers as well as the performance of the hodoscopes in flight. A description of the hodoscopes can be found in Chapter 2.

A.1 Hodoscope Mapping

The fibers used in the hodoscope were custom-made and drawn using a slowly rotating aluminum wheel, and then glued together into ribbons and cut to size. Each plane of fibers consisted of multiple ribbons glued together. However, the fibers were not always perfectly straight and their lateral position could vary up to ∼3-4mm from a straight line. The number of fibers in a single fiber tab as described in Section 2.2 also varied from tab to tab within a single fiber layer. To account for these effects, I created a map of the (x, y) position of the intersection of each x-tab and each y-tab on all four hodoscope planes.

An uncertainty in the (x, y) position of a particle in the top and bottom hodoscope results in an uncertainty in the incidence angle. Love et al. (1977) showed that an uncertainty in the incidence angle has an effect on the charge resolution of other detectors in an instrument:

$$\sigma_Z = \left(\frac{1}{\alpha\sqrt{6}}\right) \sin\theta \cos\theta \left(\frac{s}{h}\right) Z. \tag{A.1}$$

Here, σ_Z is the contribution to the charge resolution from the hodoscope, θ is the incidence angle, s is the width of the hodoscope tabs, and h is the height between the bottom and top hodoscope laters. This equation is for detectors whose signal is proportional to Z^α, so for the SuperTIGER Cherenkov counters α=2 and for the scintillator detectors $\alpha \approx 1.7$.

A.1.1 Mapping Apparatus and Procedure

The SuperTIGER mapping apparatus was adapted from the apparatus used to map the fiber hodoscopes on TIGER. Two steel plates were attached to a pair of metal beams, which sat on a large lab table. The steel plates had holes drilled into them for the attachment of a movable set of (x, y) stages. The long axis of this stage was attached to the metal plates, and sat over the hodoscope fibers. This long-axis stage was attached to a step motor. Attached to the moveable platform of the stage was another stage, this one a short ($\sim$1m) stage, also attached to a step motor. Attached to the moveable portion of this second stage was a microscope and a camera, as well as a flashlight for illumination. Both stages were attached to rulers so that I could measure the (x, y) location easily. The camera was linked to a television monitor which had an overhead transparency of a bullseye taped to it. To measure the location of the edge of a coarse segment (each segment had 12 tabs), I illuminated the edge fiber in the segment using a standard laser pointer. Figure A.1 shows the laser pointer and a fiber being illuminated in the mapping apparatus. I then marked the illuminated fiber by placing a razor blade on its side on top of the fiber, with a corner

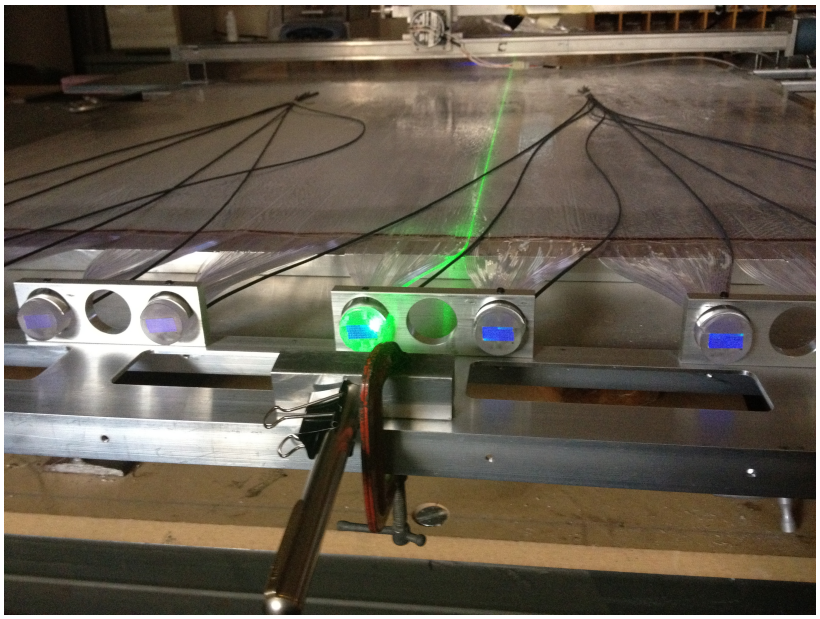

Figure A.1: The hodoscope mapping setup with a laser illuminating a single fiber for mapping.

of the razor blade in the middle of the fiber. I then moved the larger moveable stage so that the edge of the marked fiber was in the center of the bullseye on the TV monitor. I then recorded the (x, y) location of the edge of the fiber. I then moved the camera along the fiber $\sim$10 cm with the smaller stage, keeping the fiber edge centered in the bullseye with the larger stage as needed. I recorded the (x, y) position of the fiber edge at this new location, and repeated this every 10 cm until the camera reached the edge of the smaller stage. I then moved the camera back to the start position and moved the larger stage over to map the edge of the next segment. Because the smaller stage did not have enough length to cover an entire hodoscope plane, once I had exhausted its range in one location of the larger stage, I moved both stages, and then repeated the process. I had to move the stages twice (for a total of 3 times through this process) for the long hodoscope fibers, and once (for a total of 2 times through) for the short fibers. I also measured the (x, y) position of easy to find reference points on each short hodoscope layer. The long hodoscope layers were mapped after being glued to the substrate and instrument frame, so I simply used the edge of the frame as the reference points there.

For comparing the relative straightness of fibers as a quick check on the mapping process, I used an aluminum straightedged meter stick to determine which of the 13 fibers I would map was the most straight, and used that as a "reference fiber". These reference fibers were not used for anything besides quick checks of the quality and accuracy of the mapping.

Finding the center of each tab

In flight, however, we need to be able to come up with a real-space location in the instrument coordinate system for each tab intersection. This document describes how I took the raw mapping data for a given hodoscope layer and converted it into a spreadsheet with the (x, y) positions of the center of each tab. The first order of business is to take the mapping data, which recorded the positions of the edges of each segment, and turn it into data on the center of each tab. Each hodoscope segment contains 12 tabs. Each tab contains between 5 and 9 fibers. On any given plane, though, the tabs contain roughly the same number of fibers. The number of fibers in any specific tab was recorded by Dana as he made each fiber layer and a copy was provided for this data analysis.

At a variety of X values, the Y value of the position of the edge of each segment was measured. The problem is thus to interpolate between the Y values at a given X to find the Y position of the center of each tab. This will depend on the average size of the fibers, S_f, computed by dividing the distance between the two edges of the segment by the number of fibers, the $Y-$position of one edge of the segment a, the number of fibers between that edge and the edge of this tab, and the number of fibers in the tab. For the ith fiber, the position of the center of the fiber is given by:

$$Y_i = a + \frac{x}{\sum_i^{12} f_i} \left(\sum_j^{i-1} f_j + \frac{f_i}{2} \right) \tag{A.2}$$

A.1.2 Converting to the Instrument Coordinate Frame

Once I had the (x, y) positions of the center of each fiber tab in the mapping apparatus frame, I converted these positions into the coordinate frame of the instrument. To do this, I measured the positions of standard reference points (the substrate aluminum frame for the long fibers and the inner corner of the active area of the short fibers, defined by the edge of pieces of red ribbon tape) in both the mapping apparatus frame and, after the short layers were glued to the long layers and the substrate, in the instrument frame. Then, I rotated and translated all of the measured centers of fiber tabs by the rotation (and translation) that transformed the (X, Y) reference points in the mapping frame to their (X', Y') coordinates in the instrument frame. These rotations and translations were done using a spreadsheet.

A.1.3 Finding Intersections Between Tabs

Once I had the position of the center of each fiber tab in the instrument frame, I fit a 4th-order polynomial function to the (x, y) positions of the center of each tab. For each hodoscope layer, this gave me 144 $y-$polynomials and 288 $x-$polynomials. I used Mathematica to find the intersections between each $y-$polynomial and all 288 $x-$polynomials, and exported the (x, y) positions to a file. This file was then converted into a .ROOT lookup table that was given to Makoto Sasaki of NASA Goddard Space Flight Center, who used it to make the .dst files as described in Chapter 4.

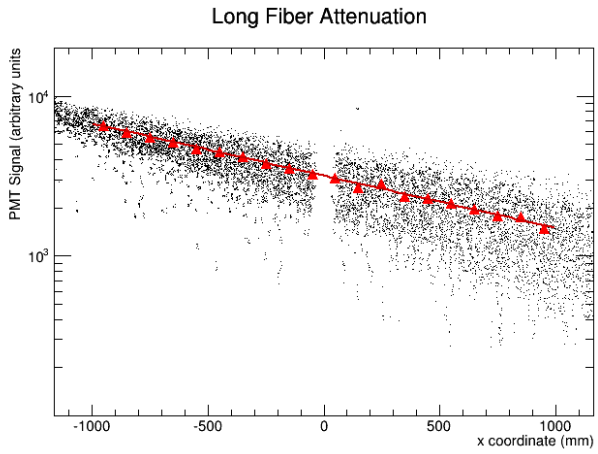

Figure A.2: Long fiber attenuation length plot.

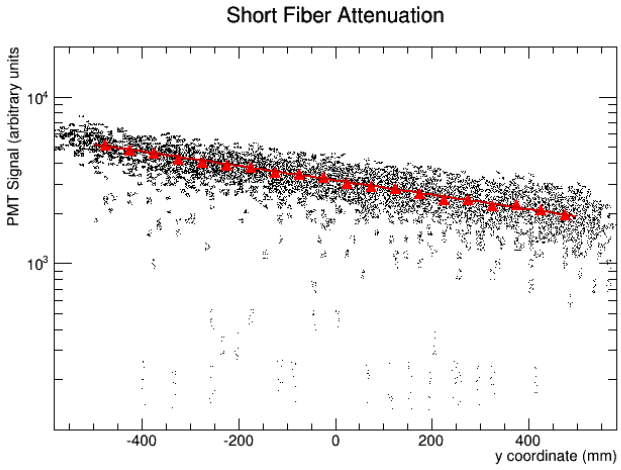

Figure A.3: Short fiber attenuation length plot.

A.2 Fiber Attenuation Length

To determine the attenuation length of the hodoscope fibers, I used data from 18 days in the middle of the flight (January 2-19, 2013), where there were no changes to the high voltage on any of the hodoscope power supplies. I used only $_{26}$Fe events with incidence angles within one radian of vertical. I treated the signal from each PMT separately, and plotted the signal from the PMT against the location along the fiber. I obtained this location using the perpendicular hodoscope plane on the same layer. I also filled histograms with 5cm binding along the length of each fiber, and fit a gaussian to each of these histograms. Figures A.2 and A.3 show the attenuation length plots for a typical long-axis and short-axis fiber, respectively. The peak of each 5-cm bin histogram is shown as a red point on the plot. We then fit a line of the form $y = Ae^{-x/\lambda}$, also shown in red, to these points. The λ in this equation is the attenuation length of that particular fiber.

The mean attenuation length of a short-axis fiber was 1.0 $\pm$ 0.2 m, while the mean attenuation length of the long-axis fibers was 1.3 $\pm$ 0.2m.

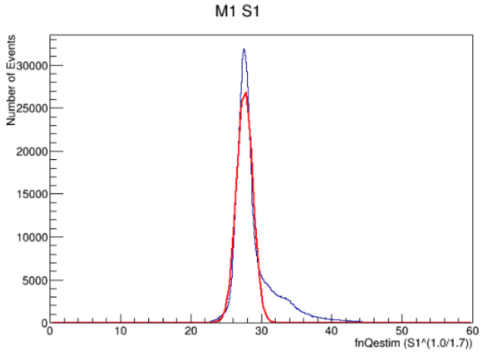

(a) Module 1 S1 "Iron" peak.

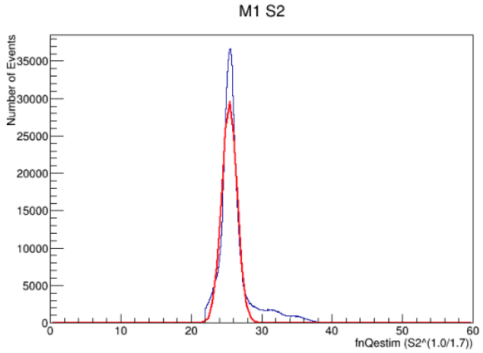

(b) Module 1 S2 "Iron" peak.

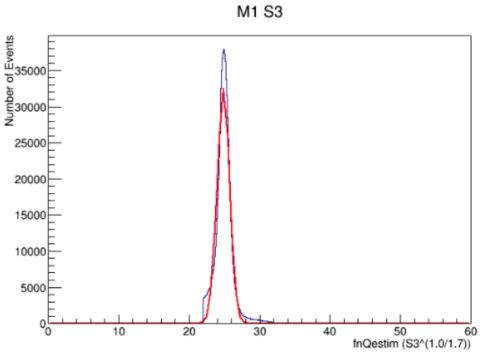

(c) Module 1 S3 "Iron" peak.

Figure A.4: Estimated "Iron" peaks for each scintillator layer in Module 1.

A.3 Hodoscope Efficiency

To determine the efficiency of the SuperTIGER scintillating fiber hodoscope in detecting events and assigning trajectories to particles that passed through the entire detector, we first defined a new set of interaction cuts. Because we wanted to determine the hodoscope efficiency, we only used raw information from the scintillator detectors without any angle or other corrections. Looking at an "estimated charge" ($S1^{1/1.7}$), we found a clearly defined "Iron" peak in each layer of the scintillator detectors, as shown in Figure A.4. In this analysis, I treated each half-module separately. I then fit this peak with a gaussian for each scintillator detector on each module (Figure A.4 shows only Module 1). I defined "good" events as those events that were within 2.5 σ of the peak in all three layers. Figure A.5 shows a cross plot of

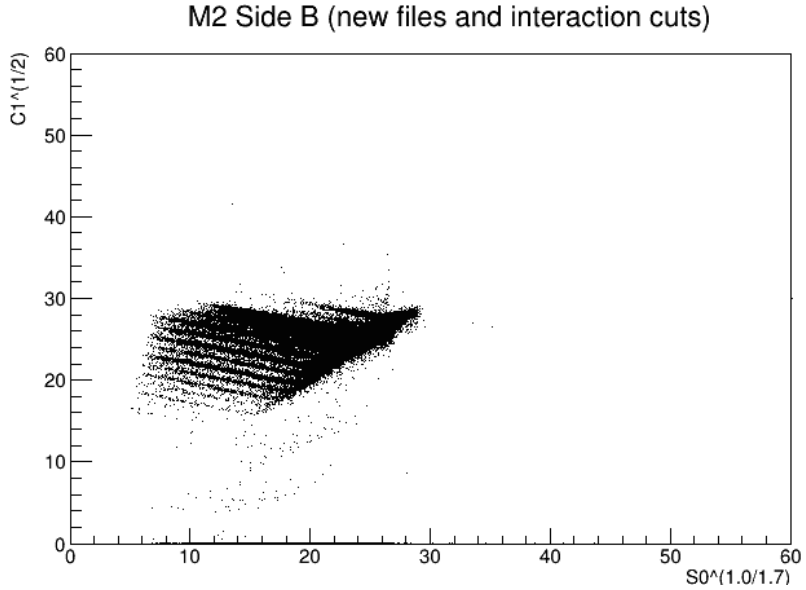

Figure A.5: Cross-plot showing the average scintillator signal vs the Acrylic Cherenkov signal for all "good" events.

the average scintillator signal ($S0 = \frac{S1+S2+S3}{3}$) vs the Acrylic Cherenkov signal of all "good" events that survived this crude interaction cut for one half module. This shows that we did successfully eliminate most of the interacted particles. It also shows that many of our "Iron" particles based on this crude measurement were in fact other elements, most likely with large incidence angles, hence the quotation marks. Selecting "good" events , I calculated the fraction that we saw 4 "good" hodoscope fits and were able to assign a trajectory to. I calculated this efficiency on a day-by-day basis over 48 days of data. Figures A.6 and A.7 show histograms of the efficiency of Module 1 and Module 2, respectively, 1 day of data per count. For Module 1, the mean efficiency was 97.17% and the peak of the gaussian fit to the histogram was 97.21%. For Module 2, the mean efficiency was 95.99% and the peak of the gaussian fit to the histogram was 96.18%. The Module 2 efficiency is lower because two of the Module 2 hodoscope HV power supplies (one on the top hodoscope, M2 9100 HVPS1, and one on the bottom, M2 9C00 HVPS1) had their voltages lowered during flight due to arcing, as was discussed in Section 3.2.1. For the instrument paper (Binns et al., 2014) we quoted an average efficiency of 96.5%.

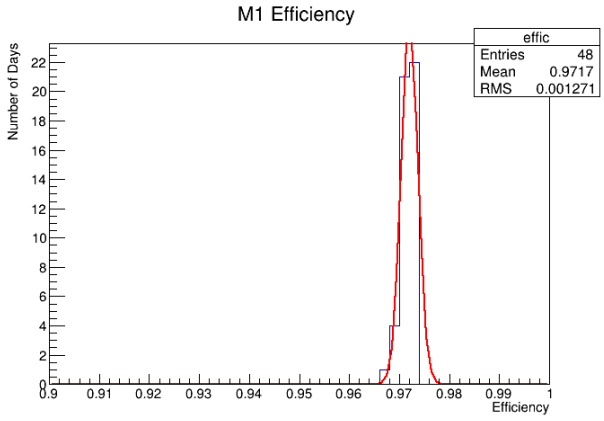

Figure A.6: Efficiency histogram on a day-by-day basis for Module 1.

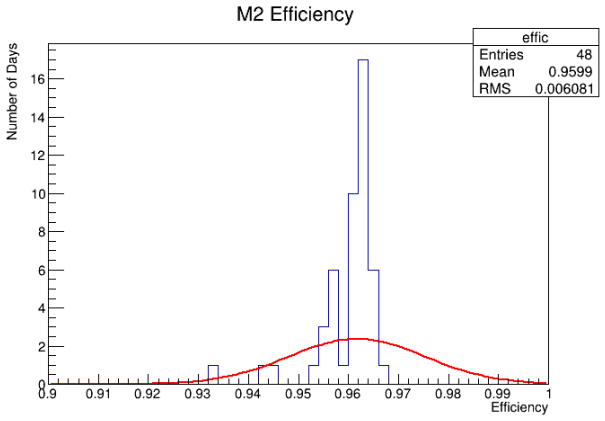

Figure A.7: Efficiency histogram on a day-by-day basis for Module 2.

Module	Mean Efficiency	Efficiency from Gaussian Fit
M1	97.17%	97.21%
M2	95.99%	96.18%

Table A.1: Hodoscope efficiency for each module based on the mean daily efficiency and the gaussian fits from Figures A.6 and A.7

I also took a look at how the efficiency of the hodoscopes changed over time. Figures A.8 and A.9 show the hodoscope efficiencies as a function of time. There was no significant change in hodoscope efficiency over the SuperTIGER flight.

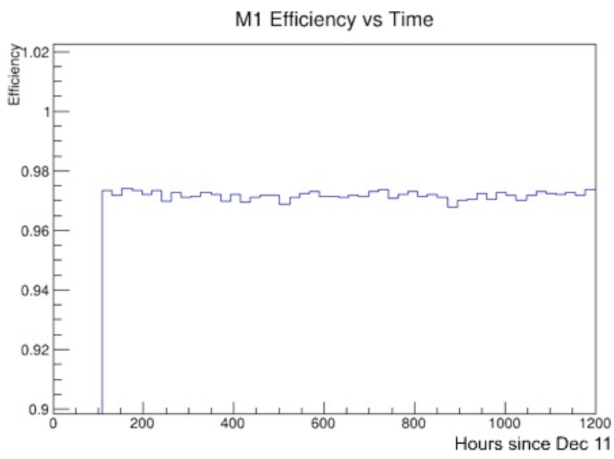

Figure A.8: Module 1 hodoscope efficiency over time.

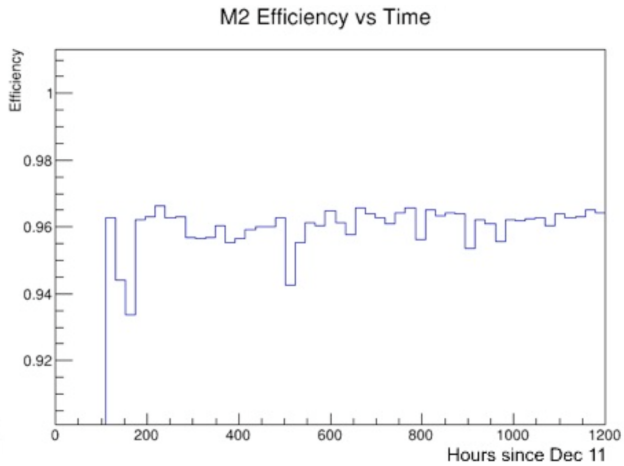

Figure A.9: Module 2 hodoscope refficiency over time.

Appendix B

Solid State Data Drive Failure

SuperTIGER used four Intel 320 series solid state disks (SSDs), two on each module. Each module had a data disk, that recorded all events in an uncompressed data format, and a root disk, which contained the operating system and stored information about the current settings used by the instrument. All four disks failed at some point during the flight.

Approximately 10.5 days after launch, it was noted on the handover conference call between the monitoring teams at Caltech and McMurdo that the payload appeared to be in an unscheduled TDRSS outage. An unscheduled outage was rare but not unheard of—when one occurred, the TDRSS center at White Sands would notify CSBF, who would pass that information along to the monitoring team, and it often took some time for the message to get through. A look at the monitor webpage confirmed that none of the housekeeping HV or other values had been updated recently, but checking the computers at CSBF confirmed that data were indeed coming in and being recorded. However, after the monitoring webpage refreshed and did not include any new data, I took a look at the incoming data and confirmed that there were in fact no housekeeping events in it. After running through the various quick-look routines, I discovered that all of the events that were being telemetered were error events, for example:

```
M1 Event Number 16716247 at time Wed Dec 19 18:01:36 2012  Message:
```

```
error saving data:  stor_next_file:  can't open '/data/supertiger/00059/
M2 Event Number 19373808 at time Wed Dec 19 18:03:37 2012  Message:
error saving data:  stor_next_file:  can't open '/data/supertiger/00059/
```

Since reply events, which include error messages like these and confirmations of commands sent to the instrument, were the highest priority events to be telemetered, the incoming data files were filled with these error messages and no other data. We first sent a command to begin a new data run on the two data disks. A new run would have simply created a new folder on the data disk for the data to be saved in. After a regularly scheduled TDRSS outage, we found that this command had been unsuccessful, and that both data disks were unable to create a new folder.

We then sent a command to end the flight program. This command saves the current instrument setting, safely ramps down the HV supplies to 0 V, stops/starts the FEE power relay, and then restarts the flight program on the computer. This command was successful, and both modules returned to their previous state. The data that was telemetered down included the normal mix of housekeeping events and actual data events from cosmic-ray nuclei. We monitored the instrument closely for $\sim$1 hour to confirm that everything was operating normally before becoming concerned that there was no data being recorded on the data disks.

Checking the data disks confirmed that there had been no increase in the amount of disk space used on either data disk for several hours. A check of the miscellaneous housekeeping confirmed a rate of 0 events written to disk. At that point, we commanded a hard reboot of both modules. Both modules booted back up and returned to their previous states, but no data were still being written to disk. After some consultation, we decided to troubleshoot the problem on Module 2. During the December 21 (local time) shift at WUSTL, we twice cycled power on and off for Module 2, hoping to reset the disk and being writing again. These attempts were unsuccessful, so the decision was made to continue on with the flight

and depend on the TDRSS data, where we were already getting the vast majority of the high-priority events down.

On December 30, we noticed signs of arcing on one of the hodoscope power supplies. I sent the command to lower the voltage on this supply (M2 9100 HVPS 2) by 50 V to 660 V. Ordinarily, this change is made on the instrument and then a reply event is sent confirming that the command was carried out. Instead, we received an error message:

```
M2 Event Number 21160952 at time Sun Dec 30 01:58:18 2012 Message:
save_fee_hvps:  Bad conf_write:  bad fopen on '/usr/local/supertiger/
M2 Event Number 21160953 at time Sun Dec 30 01:58:18 2012 Message:
SET_HVPS couldn't save new hvps value in conf file
```

Housekeeping events confirmed that the voltage had been changed as requested, but the error messages indicated that the setting was unable to be saved. The current HV settings are saved on the root disk of each CPU, so this error message meant that the Module 2 root disk was not able to save files. To confirm this, I sent the command to change an inconsequential parameter (the length of LED pulses in calibration events, which we were not taking at this point in the flight) on both modules. A similar error message came back from both flight CPUs, indicating that the Module 1 root disk was unable to save files as well. This meant that if the flight CPUs were to restart for any reason, they would boot up in the last saved configuration, which we were now unable to modify.

On the final day of flight, the flight computers were turned off entirely in preparation for the termination of the flight. However, the winds shifted, and the flight was extended temporarily. We turned the power back on to the flight computers. As expected, Module 2 booted up into the last saved configuration, and we changed the HV values back to what they had been before the shutdown. Module 1, however, did not boot up. However, enough of the Module 1 system was running that data from Module 2 were transmitted through the multiplexer board located on Module 1. We got an additional $\sim$3 hours of data from

Module 2 before we powered the system off again and shut everything down in preparation for termination.

Testing after the instrument was recovered confirmed that the Module 1 CPU could boot up, but the boot would hang when searching for the root disk, which it was not able to read. The Module 2 CPU could boot up and read the root disk, but the flight program could not write to it. The Module 1 data disk was unreadable. The Module 2 data disk was readable, and contained all of the flight data recorded by that module up until the initial error occurred. This data has not yet been incorporated into the SuperTIGER dataset.

Appendix C

Data Pre-Processing and Calibration

The SuperTIGER data were telemetered in an ASCII text-based format. The data telemetered down via the LOS antennae were in an uncompressed format, while the data telemetered via TDRSS were compressed as described in Section 2.5. Telemetered TDRSS data were stored on two computers at CSBF in Palestine, TX. There were short periods where one of these computers was unavailable, but at least one computer was functioning and recording events throughout the flight. The LOS events were initially stored on the ground support computer at the LDB facility near McMurdo Station, but were later copied to a server at Washington University. Each event was given a unique event number, which allowed for the easy combination of the files stored on these three separate computers.

After the flight, Makoto Sasaki of GSFC converted these data files to useable Data Storage and Transfer (DST) files. He first parsed the individual data files, and discarded all files that had a bad checksum, i.e. those that were not transmitted and stored properly. The number of files discarded at this step was small, and generally only occurred during periods of bad or intermittent TDRSS connection, such as when changing satellites or the beginning and end of a satellite window. Data from the two TDRSS computers in Palestine were then combined, with each unique event number being included in the combined data file once. If LOS data existed for events that existed in the TDRSS files, the LOS event information was

used for the combined data file. These data files were then combined into larger files, each containing information from one hour of the flight. This completed the data pre-processing.

C.1 Calibration

These pre-processed data files were then used to create a calibrated data set, again by Makoto Sasaki of GSFC. This calibration was done in 56 runs, each containing 24 hours (from 00:00:00 NZDT to 23:59:59 NZDT on a given day) of data. This calibration was done to correct for areal (due to detector design) and temporal (due to thermal effects) differences in response. Each of these runs was then divided into subgroups that were used for calibration. The amount of time in each subgroup varied, but each included at least 32 pedestal events and at least 30,000 high-priority events. Pedestal events measured the signal voltage read out by individual FEE channels for individual PMTs when no light was incident on the photocathode. This signal voltage included the raw voltage coming from the PMT (for the hodoscope) or preamplifier board (for scintillator and Cherenkov detectors) and a voltage offset added by the FEE board. The value of the pedestal signal was slightly different for each PMT, and could fluctuate slightly during flight. Taking at least 32 pedestal events per channel allowed for a determination of the average pedestal value in that particular timeframe/event subgroup. A broad distribution of pedestal values was also an indication of an arcing or other HV problems during flight. The high-priority events were those events selected by the priority scheme described in Section 2.5. The value of the pedestal for each PMT (found using these at least 32 pedestal events) was then subtracted from the signal for that particular tube in all of the events of the subgroup.

C.1.1 Gain Correction

These sub-groups were then used to determine the gain correction for each detector. The gain properties of each PMT were slightly different, and, while we gain-matched PMTs within individual detectors as best we could, there were still differences within and between detectors. For the scintillator detectors, the gain correction was calculated in two ways. First, a relative gain calculation compared the signals from one PMT to the total signal from all 8 PMTs in that particular detector. Then, an "Absolute" gain calculation was performed using only selected Iron events (the selection process is described below). This "Absolute" gain calculation was also used for the hodoscopes. For the Cherenkov detectors, the "Absolute" gain calibration was used alongside two relative gain corrections. The first relative gain correction compared the signal from one PMT to the total signal from the 7 PMTs attached to the same FEE board. The second relative gain correction compared the signal from one PMT to the summed signal from the 21 total PMTs in the same Cherenkov half-detector. After these gain corrections, each PMT on a FEE board should respond to the same stimulus with the same signal.

C.1.2 Mapping Correction

The next step was the primary mapping correction, again applied to each of these time sub-groups. The mapping correction used the (x, y) information from the top and bottom hodoscope planes to determine a path through the detector, and, therefore, the location where each event travelled through each of the scintillator and Cherenkov radiators. The primary mapping correction was applied first on an individual PMT basis to the scintillator and Cherenkov PMTs. Each scintillator detector or Cherenkov half-module was divided into a 4 cm $\times$ 4 cm grid (this was later repeated with a finer 2 cm $\times$ 2 cm grid). A correction factor for each 4 cm $\times$ 4 cm area of the detector was found that would ensure that the

response of the PMT was the same regardless of the particle's location within the detector. An additional correction was found for the Cherenkov detectors using the responses of all 7 PMTs on a FEE board in place of a single PMT. An "Absolute" correction was then applied to the entire detector using selected Iron events to eliminate differences between detectors.

C.1.3 Iron Selection

Iron events were selected using a series of cross plots. First, a cross plot comparing the C1 vs C0 signals was created, and a box was drawn along the Iron events on that plot. Then, a similar plot was made for S1 vs C0, S2 vs C0, etc., for all possible combinations of S and C detectors. In each, a box was drawn around the Iron events, and these boxes were used to determine which Iron events were used for the whole-detector calibration. While the Iron events selected during this process were only a fraction of the total number of Iron events observed during flight, Iron is abundant enough that there were sufficient statistics to make all of the required corrections.

C.1.4 Re-Calibration

After initially calibrating the data, this entire calibration train was repeated a second time. The second time through, a finer mapping correction (2 cm $\times$ 2 cm) was used, and the gain calibration and mapping corrections were repeated. This included both the individual PMT corrections and the whole-detector corrections, as well as the additional corrections per Cherenkov FEE board.

C.1.5 Secondary Mapping Correction

A secondary mapping correction was also used in data analysis, but was not included by default in the DST files. This secondary mapping correction actually incorporates 4 separate corrections, designed to correct the effects of incidence angle and path length on detector signal. While the primary conventional mapping found correction factors for a standard (x, y) map of the detector, the secondary corrections combined the (x, y) coordinates from the top and bottom hodoscopes in different ways. The "X-map" found correction factors in (X_{BOTTOM}, X_{TOP})[10] space using the same method as the primary correction described above, substituting the x-coordinate in the bottom hodoscope for the x coordinate used before, and the x coordinate in the top hodoscope layer for the y coordinate. Similarly, the "Y-map" found correction factors in (Y_{BOTTOM}, Y_{TOP}) space, while the "P-map" and "M-map" found correction factors in $([Y_{BOTTOM} + X_{BOTTOM}], [Y_{TOP} + X_{TOP}])$ and $[Y_{BOTTOM} - X_{BOTTOM}], [Y_{TOP} - X_{TOP}])$ space, respectively. These correction factors were saved in a companion file to the DST files with flight data in them, but had to be called specifically by the selector files in order to be used.

C.2 Creating DST Files

These corrected event values were then packaged together into a Data Storage and Transfer (DST) .root file for use with the ROOT data analysis package. One DST file included 24 hours of flight data (from 00:00:00 NZDT to 23:59:59 NZDT on a given day). This file contained a wealth of information on each event. For each event, it listed an event number, an event time, and then two sets of information about the event, a "header" including information about the general state of the instrument, and a "dst" set including

[10]Here, I use (x, y) to indicate the location of the particle within the instrument, while X_{BOTTOM}, X_{TOP}, etc. are used to indicate the x-value in the bottom hodoscope and top hodoscope, and so on.

information about the event itself. The "header" for each event in the DST file contains information about the state of the instrument when that event was recorded, including the latitude, longitude and altitude from the SIP, the pressure from 3 different SIP barometers, whether the event was classified as high-priority or low-priority, and whether the event came over the LOS or TDRSS downlink. The "dst" set of parameters for each event in the DST file includes 32 different pieces of information about each event, including which module it occurred in, how many hodoscope fibers it gave a good signal in, the (x, y) positions at the top and bottom hodoscopes, the incidence angle, the total signal observed in each detector, and a rough estimate of the charge from each detector. For the data analysis, this total signal observed in each detector is what we refer to as the signal, e.g. "S1 signal" is the total signal from the S1 scintillator detector.

These DST files were what I used to analyze the data for the rest of the chapter and the primary analysis. An expanded "raw" set of DST files was also generated, which included information on each PMT for every event. These raw files were used when doing analysis on a single-PMT level, such as finding the Hodoscope Attenuation Length in Appendix A, but proved unwieldy and unnecessary for the primary data analysis.

Appendix D

Scintillator Response Functions and Saturation Models

The SuperTIGER Scintillator Detectors provide a measurement of the amount of light emitted by the radiator as a function of the path length traversed by the ionizing particle, $\frac{dL}{dX}$. The radiator of each scintillator is comprised of a base material, with a small amount of primary and secondary dyes. In an ideal scintillator, the amount of scintillation light produced will be proportional to the energy loss given by the Bethe-Bloch equation (adapted from the treatment in Leo (1994)):

$$-\frac{dE}{dx} = 2\pi N_A r_e^2 m_e c^2 \rho_{ab} \frac{Z_{ab}}{A_{ab}} \frac{Z^2}{\beta^2} \left[ln\left(\frac{2m_e\gamma^2 v^2 W_{max}}{I}\right) - 2\beta^2 - \delta - 2\frac{C}{Z_a b}\right]. \tag{D.1}$$

The first several factors of this equation–N_a, Avogadro's number, r_e, the classical electron radius, m_e, the mass of the electron, c, the speed of light, and 2π–form a constant, $2\pi N_A r_e^2 m_e c^2 = 0.1535 MeV cm^2/g$. The remaining terms outside the bracket show that the amount of energy lost depends on atomic number to atomic mass ratio (Z_{ab}/A_{ab}) of the absorbing material, the density of the absorbing material ρ_{ab}, the charge of the incident particle squared (Z^2), and the inverse square of the relativistic velocity ($\frac{1}{\beta^2}$). The natural log term depends on the maximum energy that can be transferred in a single collision (W_{max}), the mean

excitation potential of the absorbing medium (I), and the velocity of the incident particle ($v, \gamma = 1/\sqrt{1-\beta^2}$). For nuclei, the incident mass is much greater than the mass of an electron, so that $W_{max} \simeq 2m_e v^2\gamma^2$. The remaining terms include a quantum mechanical correction ($-2C/Z_{ab}$,with shell correction term C), a term for the relativistic increase in energy loss ($-2\beta^2$), and a density correction ($-\delta$).

When a particle deposits a large amount of energy in a small volume of the scintillator, however, saturation occurs. This means that the actual energy converted to light as a function of path length (dL/dx) is a fraction of the stopping power (dE/dx) that decreases with increasing density of ionization. To fit the SuperTIGER Below C0 dataset, a number of different models of scintillator response were tested. For initial calibration and response cross-plots with scales roughly equivalent to integer charge units we used the simple assumption that the scintillator signal went as $S = Z^{1.7}$. This naive assumption is sufficient to find an Iron peak but does not give well-defined peaks for $Z > 26$. Figure D.1 shows the charge histogram generated using this naive assumption compared with the simplest of the saturation models I tried.

The general method for comparing the various models of scintillator saturation started with assigning charge using the method discussed in Section 4.4, but with the particular response model I was testing taking the place of the Voltz Model in that model. Once the charges were assigned to events in the Below C0 dataset (with a restrictive set of interaction cuts in place), I compared the charge resolution at Iron, the location of the Iron peak, and definition and separation of higher-Z peaks. Initially, these models were only tested on the top scintillator detector (S1), but eventually charge was assigned using both the S1 and S2 detectors. These models are all energy-independent, since the method from Section 4.4 relies on on fitting the scintillator response function in a very narrow energy range.

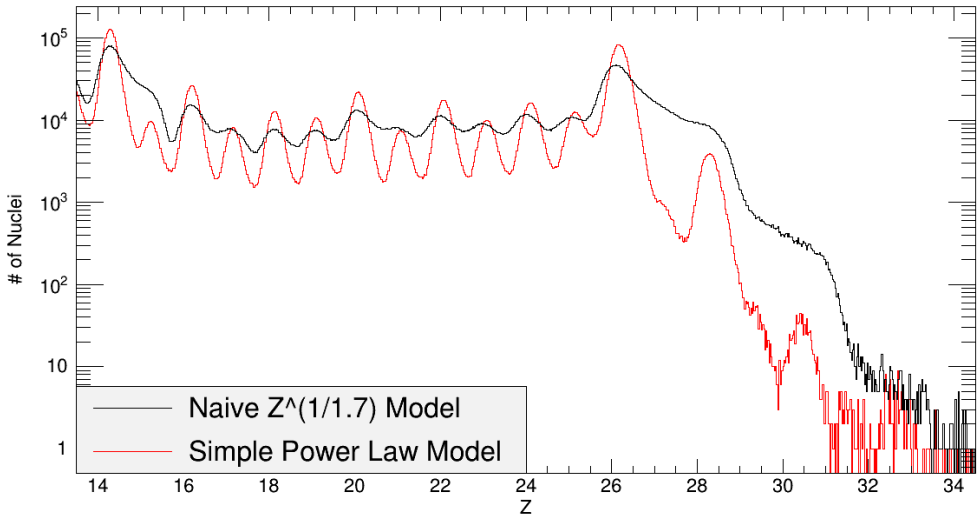

Figure D.1: Our naive model finds the Iron peak but not much else. The Simple Power Law model provides a noticeable improvement, and was used to find C1/Z^2 in Equation 4.9.

The first model I tried was a simple power law model. Rather than assuming that $S = Z^{1.7}$, this model allowed for a different power α for each angle and energy bin:

$$S_{SimP} = Z^{\alpha}. \tag{D.2}$$

The results of this model for assigning charge using only S1 are shown along with the naive $Z^{1.7}$ model in Figure D.1. This model represents an improvement over the naive model and was used as a simple proof-of-concept of the code and method described in 4.4 with a single parameter. After this, I tested a modified power law using a form tested during the TIGER analysis by Link (2003):

$$S_{ModP} = AZ^{BZ+C}. \tag{D.3}$$

This form was tested at the same time as the Voltz and BTV models described below, and was abandoned because it did not fit the data as well as the other two models. It was not used on TIGER for similar reasons.

I also tested two polynomial models. The reasoning behind the first, a 4th-order polynomial, was that the energy lost to non-radiative effects came from two excited states interacting with each other, so the non-radiative term is proportional to the density of the energy deposited squared, or Z^4.

$$S_{New4} = AZ^2 - BZ^4 \tag{D.4}$$

This model did not fit the peaks at high Z very well (see Figure D.2) so we decided to test another model with the possibility that a third excited state could interact with two others, giving a Z^6 term:

$$S_{New6} = AZ^2 - BZ^4 - CZ^6 \tag{D.5}$$

This proved to be a bit of an overcorrection compared to the 4th-order model (again, see Figure D.2) and provided unphysical results at high Z, so both of the polynomial models were abandoned.

The two most promising and, ultimately, most accurate models were those developed by Tarle et al. (1979) and Voltz et al. (1966). The "BTV" Model from Tarle et al. (1979). Both models use the formalism first proposed by Voltz et al. (1966), in which the region closest to the path of a sufficiently energetic particle (the "core") will be fully quenched, and therefore not sensitive to changes in dE/dx, while an outer region (the "halo"), will luminesce due to the energy deposited by knock-on electrons, and the light emitted in this region will depend on dE/dx. The energy-independent form of the BTV model is:

$$S_{BTV} = \frac{AZ^2}{1 + BZ^2} + CZ^2. \tag{D.6}$$

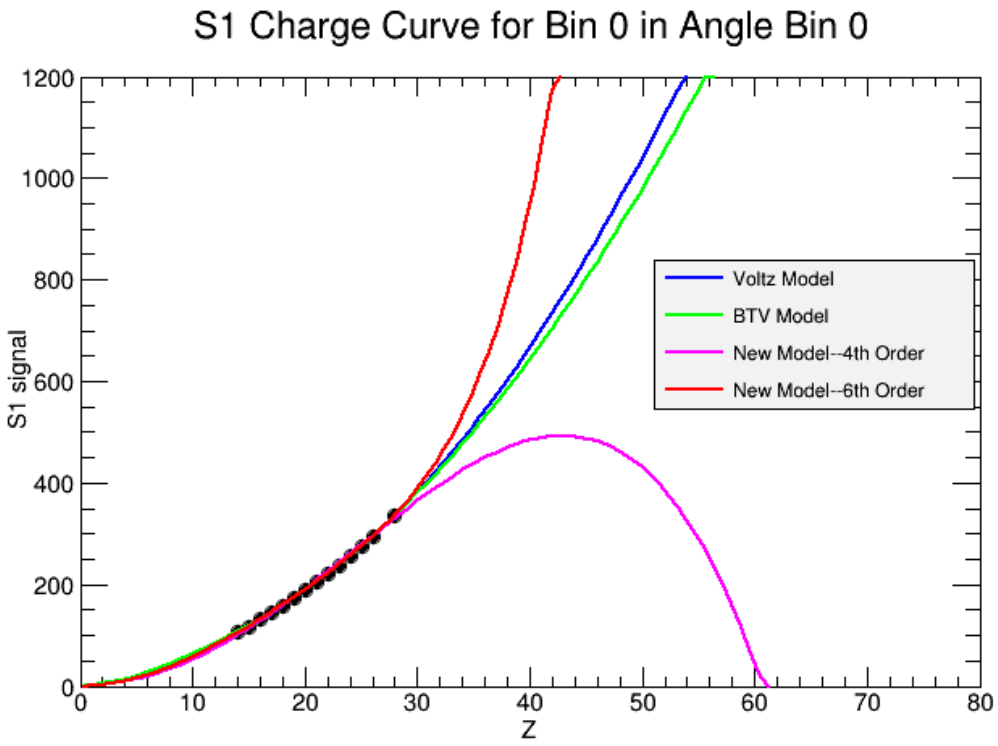

Figure D.2: Comparing the BTV model, Voltz Model, and the two "new" polynomial models as a function of Z. Black dots are the values of S1 signal and Z used to fit each model. Outside the fit range, the polynomial models do not give a good model of scintillator response with Z.

The BTV model provided similar results to the Voltz Model, but gave worse charge resolution at Iron and did not give particularly well-defined peaks at higher Z. It was tested but not used on the TIGER data for similar reasons (Link, 2003).

Improving our understanding of the SuperTIGER scintillator detectors and their response to higher Z particles will require further testing. A six-day test using a $_{82}$Pb beam at CERN is planned for late 2015.

Appendix E

SuperTIGER Material Stackup

Tables E.2, E.3, and E.4 show the thicknesses of each layer of material within the SuperTIGER instrument, starting from the top of the thermal insulation. The table contains information on the type of material, its thickness, density, and column density, as well as what type of material ("Alias") we treated it as for the interaction and energy corrections within the instrument. The cumulative column density of all material from the top of the instrument is also shown. Table E.1 contains more information about the materials used in the SuperTIGER instrument.

Abbreviation	Material	Chemical Formula	Brand Name
PVT	Polyvinyltoulene	C_9H_{10}	
PS	Polystyrene	C_8H_8	
PMMA	Poly Methyl Methacrylate (Acrylic)	$C_5H_8O_2$	
PE	Polyethylene	C_2H_4	Tyvek
PVF	Polyvinyl fluoride	C_2H_3F	
PMI	polymethacrylimide	$C_8H_{11}O_2N$	Rohacell
PET	Polyethylene terephthalate (Mylar)	$C_{10}H_8O_4$	
	Melanine foam	$C_4H_6N_6$	Techlite
PU	Polyurethane	$C_2H_{42}N_2O_6$	
PTFE	Polytetrafluoroethylene	C_2F_4	Gore-TEX

Table E.1: Materials used in the SuperTIGER Instrument.

Detector	Description	Thickness cm	Material	Density g/cm^3	Column Density g/cm^2	Alias	Cum. Column Density g/cm^2
Thermal Insulation	Mylar layer	0.013	Mylar (PET)	1.390	0.018	Mylar	0.018
	Techlite 079	2.540	Melanine foam	0.009	0.023	PMMA	0.040
Scintillator S1	Light shield	0.012	Al foil	2.700	0.033	Al	0.073
	Defuse reflector	0.005	Reflector, Mylar (PET)	1.390	0.007	Mylar	0.080
	Plastic scintillator	1.016	PVT	1.030	1.046	PVT	1.127
	Defuse reflector	0.005	Reflector, Mylar (PET)	1.390	0.007	Mylar	1.134
	Depron foam	0.300	EPS	0.040	0.012	PS	1.146
	Floor	0.011	Al foil	2.700	0.031	Al	1.177
		0.005	Hysol EA 9396 (Epoxy)	1.135	0.006	Mylar	1.183
		1.270	Rohacell 0.5” (PMI)	0.032	0.041	Rohacell	1.223
		0.005	Hysol EA 9396 (Epoxy)	1.135	0.006	Mylar	1.229
		0.011	Al foil	2.700	0.031	Al	1.260
Top Hodoscope	Light shield	0.012	Al foil	2.700	0.033	Al	1.293
	X fibers	0.100	PS -81%, PMMA 19%	1.060	0.106	PS	1.399
	separator	0.005	PE (Low Density)	0.919	0.005	PE	1.403
	separator	0.005	PE (Low Density)	0.919	0.005	PE	1.408
	Y fibers	0.140	PS -81%, PMMA 19%	1.060	0.148	PS	1.556
	Floor	0.011	Al foil	2.700	0.031	Al	1.587
		0.005	Hysol EA 9396 (Epoxy)	1.135	0.006	Mylar	1.593
		1.588	Rohacell 5/8” (PMI)	0.032	0.051	Rohacell	1.644
		0.005	Hysol EA 9396 (Epoxy)	1.135	0.006	Mylar	1.650
		0.011	Al foil	2.700	0.031	Al	1.680

Table E.2: Materials and Thicknesses in the SuperTIGER Instrument, Part 1.

Detector	Description	Thickness cm	Material	Density g/cm^3	Column Density g/cm^2	Alias	Cum. Column Density g/cm^2
Aerogel	Light shield	0.012	Al foil	2.700	0.033	Al	1.713
Cherenkov	Defuse reflector	0.025	Gore-Tex	0.600	0.015	PS	1.728
C0	Air	17.320	Air	0.000	0.000	PS	1.728
	Aerogel	0.003	LDPE film	0.920	0.002	PS	1.731
		3.000	Aerogel	0.205	0.614	SiO2	2.345
	Defuse reflector	0.025	Gore-Tex	0.600	0.015	PS	2.360
		0.003	LDPE film	0.920	0.002	PS	2.362
	Allan's cushion foam	0.635	PU	0.080	0.051	PS	2.413
	Pallet	0.008	Al	2.700	0.021	Al	2.434
		0.005	Hysol EA 9396 (Epoxy)	1.135	0.006	Mylar	2.440
		0.476	Rohacell 3/16" (PMI)	0.032	0.015	Rohacell	2.455
		0.005	Hysol EA 9396 (Epoxy)	1.135	0.006	Mylar	2.461
		0.008	AL	2.700	0.021	Al	2.481
	Floor	0.011	Al	2.700	0.031	Al	2.512
		0.005	Hysol EA 9396 (Epoxy)	1.135	0.006	Mylar	2.518
		1.270	Rohacell 1/2" (PMI)	0.032	0.041	Rohacell	2.558
		0.005	Hysol EA 9396 (Epoxy)	1.135	0.006	Mylar	2.564
		0.011	Al	2.700	0.031	Al	2.595
Acrylic	Light shield	0.012	Al foil	2.700	0.033	Al	2.628
Cherenkov	Defuse reflector	0.025	Gore-Tex	0.600	0.015	PS	2.643
C1	Air	0.000	Air	0.000	0.000	PS	2.643
	Acrylic	1.270	Acrylic 0.5" (PMMA)	1.180	1.499	PMMA	4.141
	Defuse reflector	0.025	Gore-Tex	0.600	0.015	PS	4.156
	Floor	0.011	Al	2.700	0.031	Al	4.187
		0.005	Hysol EA 9396 (Epoxy)	1.135	0.006	Mylar	4.193
		1.270	Rohacell 1/2" (PMI)	0.032	0.041	Rohacell	4.234
		0.005	Hysol EA 9396 (Epoxy)	1.135	0.006	Mylar	4.240
		0.011	Al	2.700	0.031	Al	4.270

Table E.3: Materials and Thicknesses in the SuperTIGER Instrument, Part 2.

Detector	Description	Thickness cm	Material	Density g/cm^3	Column Density g/cm^2	Alias	Cum. Column Density g/cm^2
Scintillator S2	Light shield	0.012	Al foil	2.700	0.033	Al	4.303
	Defuse reflector	0.005	Reflector, Mylar (PET)	1.390	0.007	Mylar	4.310
	Plastic scintillator	1.016	PVT	1.030	1.046	PVT	5.357
	Defuse reflector	0.005	Reflector, Mylar (PET)	1.390	0.007	Mylar	5.364
	Depron foam	0.300	EPS	0.040	0.012	PS	5.376
	Floor	0.011	Al foil	2.700	0.031	Al	5.407
		0.005	Hysol EA 9396 (Epoxy)	1.135	0.006	Mylar	5.413
		1.270	Rohacell 0.5" (PMI)	0.032	0.041	Rohacell	5.453
		0.005	Hysol EA 9396 (Epoxy)	1.135	0.006	Mylar	5.459
		0.011	Al foil	2.700	0.031	Al	5.490
Bottom Hodoscope	Light shield	0.012	Al foil	2.700	0.033	Al	5.523
	X fibers	0.100	PS -81%, PMMA 19%	1.060	0.106	PS	5.629
	separator	0.005	PE (Low Density)	0.919	0.005	PE	5.633
	separator	0.005	PE (Low Density)	0.919	0.005	PE	5.638
	Y fibers	0.140	PS -81%, PMMA 19%	1.060	0.148	PS	5.786
	Floor	0.011	Al foil	2.700	0.031	Al	5.817
		0.005	Hysol EA 9396 (Epoxy)	1.135	0.006	Mylar	5.823
		1.588	Rohacell 5/8" (PMI)	0.032	0.051	Rohacell	5.874
		0.005	Hysol EA 9396 (Epoxy)	1.135	0.006	Mylar	5.880
		0.011	Al foil	2.700	0.031	Al	5.910
Scintillator S3	Light shield	0.012	Al foil	2.700	0.033	Al	5.943
	Defuse reflector	0.005	Reflector, Mylar (PET)	1.390	0.007	Mylar	5.950
	Plastic scintillator	1.016	PVT	1.030	1.046	PVT	6.997
	Defuse reflector	0.005	Reflector, Mylar (PET)	1.390	0.007	Mylar	7.004
	Depron foam	0.300	EPS	0.040	0.012	PS	7.016
	Floor	0.011	Al foil	2.700	0.031	Al	7.047
		0.005	Hysol EA 9396 (Epoxy)	1.135	0.006	Mylar	7.053
		1.270	Rohacell 0.5" (PMI)	0.032	0.041	Rohacell	7.093
		0.005	Hysol EA 9396 (Epoxy)	1.135	0.006	Mylar	7.099
		0.011	Al foil	2.700	0.031	Al	7.130

Table E.4: Materials and Thicknesses in the SuperTIGER Instrument, Part 3.

References

A. Abramowski et al. *Science*, **347**:406–412, 2015.

M. Ackermann et al. *Science*, **334**:1103, 2011.

M. Ackermann et al. *Science*, **339**:807, 2013.

S. P. Ahlen. *Reviews of Modern Physics*, **52**:121–173, 1980.

E. Aliu et al. *The Astrophysical Journal*, **770**:93, 2013.

E. Anders and N. Grevesse. *Geochim. Cosmochim. Acta*, **53**:197, 1989.

Y. Asaoka et al. *Nuclear Instruments and Methods A*, **416**:236, 1998.

M. Asplund, N. Grevesse, A. J. Sauval, and P. Scott. *Annu, Rev. Asron. Astrophys.*, **47**: 481–522, 2009.

W. R. Binns, M. H. Israel, J. Klarmann, T. L. Garrard, E. C. Stone, and C. J. Waddington. In R. Ramaty, T. L. Cline, and J. F. Ormes, editors, *Essays in Space Science*, pages 173–189. NASA Conference Publication 2464, 1987.

W. R. Binns, T. L. Garrard, P. S. Gibner, M. H. Israel, M. P. Kertzman, J. Klarmann, B. J. Newport, E. C. Stone, and C. J. Waddington. *The Astrophysical Journal*, **346**:997, 1989a.

W. R. Binns, M. E. Wiedenbeck, M. Arnould, A. C. Cummings, J. S. George, S. Gorily, M. H. Israel, R. A. Leske, R. A. Mewaldt, G. Meynet, L. M. Scott, E. C. Stone, and T. T. von Rosenvinge. *The Astrophysical Journal*, **634**:351–364, 2005.

W. R. Binns, R. G. Bose, D. L. Braun, T. J. Brandt, W. M. Daniels, G. A. de Nolfo, P. F. Dowkontt, S. P. Fitzsimmons, D. J. Hahne, T. Hams, M. H. Israel, J. Klemic, A. W. Labrador, J. T. Link, R. A. Mewaldt, J. W. Mitchell, P. Moore, Murphy R. P., M. A. Olevitch, B. F. Rauch, K. Sakai, F. San Sebastian, M. Sasaki, G. E. Simburger, Stone. E. C., C. J. Waddington, J. E. Ward, and M. E. Wiedenbeck. *The Astrophysical Journal*, **788**:18, 2014.

W.R. Binns, T. L. Garrard, P. S. Gibner, M. H. Israel, M. P. Kertzman, J. Klarmann, B. J. Newport, E. C. Stone, and C. J. Waddington. *The Astrophysical Journal*, **346**:997, 1989b.

W. R. Binns et al. In R. A. Mewaldt, editor, *Acceleration and Transport of Energetic Particles Observed in the Heliosphere*, page 413. AIP, New York, 2000.

W. R. Binns et al. *Proc. of the 33rd International Cosmic Ray Conference (Rio de Janeiro)*, page 0646, 2013.

B. Byrnak et al. *Proceedings of the 18th International Cosmic Ray Conference*, **2**:29, 1983.

M. Cassé and P. Goret. Ionization modes of cosmic ray sources. *The Astrophysical Journal*, **221**:703–712, 1978.

C. J. Cesarsky and T. M. Montmerle. *Proceedings of the 17th International Cosmic Ray Conference*, **9**:207, 1979.

A. Chieffi and M. Limongi. *The Astrophysical Journal*, **764**:21, 2013.

A. J. Davis et al. Acceleration and transport of energetic particles observed in the heliosphere. In R. A. Mewaldt, J. R. Jokipii, M. A. Lee, E. Mobius, and T. H. Zurbuchen, editors, *American Institute of Physics Conference Series Vol 528*. 2000.

D. C. Ellison, L. O. Drury, and J. P. Meyer. Galactic cosmic rays from supernova remnants ii. shock acceleration of gas and dust. *The Astrophysical Journal*, **487**:197, 1997.

J. J. Engelmann, P. Ferrando, A. Soutoul, P. Goret, and E. Juliusson. *Astronomy and Astrophysics*, **316**:555, 1990.

R. I. Epstein. The acceleration of interstellar grains and the composition of the cosmic rays. *Monthly Notices of the Royal Astronomical Society*, **193**:723–729, 1980.

P. H. Fowler, R. N. F. Walker, M. R. W. Masheder, R. T. Moses, A. Worley, and A. M. Gay. *The Astrophysical Journal*, **314**:739–746, 1986.

N. Gehrels. *The Astrophysical Journal*, **303**:336, 1986.

N. Grevesse, M. Asplund, A. J. Sauval, and P. Scott. *Astrophys Space Sci.*, **328**:179–183, 2010.

J. E. Grove and R. A. Mewaldt. *Nuclear Instruments and Methods in Physics A*, **314**: 495–503, 1992.

T. Hams et al. *Proceedings of the 29th International Cosmic Ray Conference*, **3**:69–72, 2005.

T. Hams et al. *Proceedings of the 32nd International Cosmic Ray Conference*, **6**:382, 2011.

V. Hess. *Physikalische Zeitschrift*, **13**:1084, 1912.

J. C. Higdon and R. E. Lingenfelter. *The Astrophysical Journal*, **590**:822–832, 2003.

J. C. Higdon and R. E. Lingenfelter. *The Astrophysical Journal*, **628**:738–749, 2005.

J. C. Higdon, R. E. Lingenfelter, and R. Ramaty. *The Astrophysical Journal*, **509**:L33–L36, 1998.

Brian Humensky and the VERITAS Collaboration. *Proceedings of the 34th International Cosmic Ray Conference*, page 1167, 2015.

M. H. Israel, W. R. Binns, E. R. Christian, A. C. Cummings, G. A. de Nolfo, K. A. Lave, R. A. Leske, R. A. Mewaldt, E. C. Stone, T. T. von Rosenvinge, and M. E. Wiedenbeck. *Proceedings of the 34th International Cosmic Ray Conference*, page 68, 2015.

A. W. Labrador et al. *Proceedings of the 23rd International Cosmic Ray Conference*, **2**:524L, 1993.

K. A. Lave, M. E. Wiedenbeck, W. R. Binns, E.R. Christian, A. C. Cummings, A. J. Davis, G. A. de Nolfo, M. H. Israel, R. A. Leske, R. A. Mewaldt, E. C. Stone, and T. T. von Rosenvinge. *The Astrophysical Journal*, **770**:117, 2013.

R. L. Leo. *Techniques for Nuclear and Particle Physics Experiments*. Springer-Verlag, 1994.

R. E. Lingenfelter. In S. Maran, editor, *Astronomy and Astrophysics Encyclopedia*. Van Nostrand, New York, 1992.

R. E. Lingenfelter and J. C. Higdon. *The Astrophysical Journal*, **660**:330–335, 2003.

Jason T. Link. *Measurement Of Ultra-Heavy Galactic Cosmic Rays With The TIGER Instrument*. PhD thesis, Washington University in St. Louis, 2003.

K Lodders. *The Astrophysical Journal*, **591**:1220, 2003.

K. Lodders, H. Palme, and H. P. Gail. Abundances of the elements in the solar system. In J.E." "Trümeter, editor, *"Landölt-Bornstein, New Series Vol. VI/4B "*. Springer-Verlag, Berlin, Heidelberg, New York, 2009.

P.L. Love et al. *NIM*, **140**:469–576, 1977.

J. P. Meyer. Solar-stellar outer atmospheres and energetic particles, and galactic cosmic rays. *The Astrophysical Journal Supplement Series*, **57**:173, 1985.

J. P. Meyer, L. O. Drury, and D. C. Ellison. Galactic cosmic rays from supernova remnants i. a cosmic-ray composition controlled by volatility and mass-to-charge ratio. *The Astrophysical Journal*, **487**:182, 1997.

T. Montmerle. *The Astrophysical Journal*, **231**:95, 1979.

NASA. *NASA's Super-Tiger Balloon Breaks Records While Collecting Data*. 2013.

B. S. Nilsen, C. J. Waddington, J. R. Cummings, T. L. Garrard, and J. Klarmann. *Phys Rev C*, **52**:3277, 1995.

National Institute of Standards and Technology. Pstar stopping-power and range tables for protons, 2015. URL `http://physics.nist.gov/PhysRefData/Star/Text/PSTAR.html`.

B. F. Rauch, J. T. Link, K. Lodders, M. H. Israel, L. M. Barbier, W. R. Binns, E. R. Christian, J. R. Cummings, G. A. de Nolfo, S. Geier, R. A. Mewaldt, J. W. Mitchell, S. M. Schindler, L. M. Scott, E. C. Stone, R. E. Streitmatter, C. J. Waddington, and M. E. Wiedenbeck. *The Astrophysical Journal*, **697**:2083, 2009.

Brian F. Rauch. *Measurement Of The Relative Abundances Of The Ultra-Heavy Galactic Cosmic Rays ($30 \leq Z \leq 40$) With The Trans-Iron Galactic Element Recorder (TIGER) Instrument*. PhD thesis, Washington University in St. Louis, 2008.

Lauren M. Scott. *Cosmic-Ray Energy Loss In The Heliosphere And Interstellar Reacceleration*. PhD thesis, Washington University in St. Louis, 2005.

R. Silverberg, C. H. Tsao, and A. F. Barhoouty. *The Astrophysical Journal*, **501**:911, 1998.

G. Tarle, S. P. Ahlen, and B. G. Cartwright. *The Astrophysical Journal*, **230**:607–620, 1979.

S. van den Bergh and R. D. Mclure. *The Astrophysical Journal*, **425**:205, 1994.

R. Voltz, J. Lopes da Silva, G. Laustriat, and A. Coche. Influence of the nature of ionizing particles on the specific luminescence of organic scintillators. *Journal of Chemical Physics*, **45**:3306, 1966.

B. A. Weaver and A. J. Westphal. *The Astrophysical Journal*, **628**:738–749, 2005.

W. R. Webber, J. C. Kish, and D. A. Schrier. *Phys. Rev C*, **41**:520, 1990.

G. D. Westfall et al. *Phys Rev C*, **19**:1309–1323, 1979.

M. E. Wiedenbeck, W. R. Binns, E. R. Christian, A. C. Cummings, B. L. Dougherty, P. L Hink, J. Klarmann, R. A. Leske, M. Lijowski, R. A. Mewaldt, E. C. Stone, M. R. Thayer, T. T. von Rosenvinge, and N. E. Yanasak. *The Astrophysical Journal Letters*, **523**:L61, 1999.

M. E. Wiedenbeck, A. J. Davis, R. A. Leske, W. R. Binns, C. M. S. Cohen, A. C. Cummings, G. A. de Nolfo, M. H. Israel, A. W. Labrador, R. A. Mewaldt, L. M. Scott, E. C. Stone, and T. T. von Rosenvinge. *Proceedings of the 29th International Cosmic Ray Conference*, **00**:101–104, 2005.

M. E. Wiedenbeck, W. R. Binns, A. C. Cummings, A. J. Davis, G. A. de Nolfo, M. H. Israel, R. A. Leske, R. A. Mewaldt, E. C. Stone, and T. T. von Rosenvinge. *Space Science Reviews*, **130**:415, 2007.

S. E Woosley and A. Heger. *Physics Reports*, **442**:269, 2007.

S. E. Woosley and T. A. Weaver. *ApJS*, **101**:181, 1995.